Design of a Wireless Power Transfer System using Electrically Coupled Loop Antennas

Shyam Chandrasekhar Nambiar

Thesis submitted to the Faculty of the
Virginia Polytechnic Institute and State University
in partial fulfillment of the requirements for the degree of

Master of Science
in
Electrical Engineering

Approved:
William A. Davis
Dennis G. Sweeney
Disapproved:
Majid Manteghi, Chair

February 19, 2015
Blacksburg, Virginia

Keywords: Wireless power transfer, Implanted antennas, Electrically Coupled Loop Antenna, Negative resistance oscillators

Design of a Wireless Power Transfer System using Electrically Coupled Loop Antennas

by Shyam Chandrasekhar Nambiar

Abstract

Wireless Power Transfer (WPT) has become quite popular over the recent years. This thesis presents some design challenges while developing a WPT system and describes a system-level methodology for designing an end-to-end system. A critical analysis of contemporary research is performed in the form of a literature survey of both academic and commercial research to understand their benefits and demerits. Some theoretical notes are presented on coupled-mode theory and coupled filter theory and the problems concerning WPT analyzed using these models. The need for higher power transfer efficiency (PTE) and power delivered to load (PDL) is studied using these models. The case for using magnetic antennas over electric antennas when surrounded by lossy media (specifically for the case of human body tissues at various frequencies) is made using some theoretical models and simulation results. An Electrically Coupled Loop Antenna (ECLA) is introduced, studied and designed for two main WPT applications, viz. free space transmission and that of powering implanted devices. An equivalent circuit is proposed to better understand the coupling effects of the antennas on a circuit level and to study the effect of various environmental and structural factors on the coupling coefficient. Some prototypes were created and measured for the two use cases of free space and implanted applications. In order to complete the system design, a negative resistance-based oscillator is designed and fabricated, that incorporates the antennas as a load and oscillates at the required frequency. Some changes in load conditions and power handling are studied by the use of two circuits for free-space (high-power) and implanted (low-power) applications. Finally, the salient points of the thesis are re-iterated and some future work outlined in the concluding chapter.

"Education is a progressive discovery of our own ignorance."

Will Durant

To my family

Acknowledgements

Contents

List of Figures

List of Tables

Abbreviations

AUT	Antenna Under Test
CMT	Coupled-Mode Theory
ECLA	Electrically Coupled Loop Antenna
BW	BandWidth
FT	Filter Theory
LTI	Linear Time Invariant
MICS	Medical Implant Communication Service
MoM	Method of Moments
PDL	Power Delivered to Load
PEC	Perfect Electric Conductor
PIFA	Planar Inverted F-Antenna
PTE	Power Transfer Efficiency
RF	Radio Frequency
SAR	Specific Absorption Rate
WPT	Wreless Power Transfer

Nomenclature

Δ S-parameter discriminant

ϵ permittivity

η intrinsic impedance

η_{opt} CMT: optimum transfer efficiency

Γ CMT: damping factor; S-parameter analysis: reflection coefficient

κ CMT: coupling coefficient

μ permeability

σ conductivity

a CMT: complex amplitude

K Rollett stability factor

k FT: coupling coefficient

Q Quality factor

Chapter 1

Introduction

1.1 History

Over the past decade, commercial products have become smaller and smaller while becoming computationally more powerful. They have changed the way humans interact with the world and the objects around them. This is the age of pervasive computing, and the effect of technology on our lives can be seen and felt by looking around us and noticing that we are almost entirely dependent on our gadgets and machines. As human beings, we love technology and creating tools and implements that make our life easier. Every year there are thousands of new inventions that shape and make our lives more comfortable than it was the previous year. As the number and complexity of these devices grows, we are faced with the problem of having to power these devices and sustain their operation ever more efficiently. Even though battery and power supply technologies (switched power electronics, High Voltage DC, etc.) have become more efficient over the years, it is definitely more desirable to have a powering/recharging solution as ubiquitous and convenient as wireless internet.

It is in this context then that the field of Wireless Power Transfer (WPT) has gained momentum lately. However, efforts to transfer power wirelessly began with Heinrich Hertz's experiments

with radio waves. Hertz used synchronously tuned resonant circuits to be able transmit using spark gaps possible (which are inherently wideband and were, therefore, outlawed in later years by regulatory bodies). However, Tesla's demonstrations at his residence and at exhibitions were what truly captured the imagination of the public. Tesla's method was to use his resonant transformers (or Tesla coils) [Tesla, 1900, 1914] for creating a zone of wireless power near the transmitter. Tesla's end objective was to provide free power to everyone over the world by making use of the disturbed charges of ground and air[1] which, albeit noble, did get him into trouble with more influential entrepreneurs (read Edison). Over the course of the past century, many different approaches have been tried in order to transfer power wirelessly. Brown [1996] brings out these 20th century efforts in his paper, especially for the cases where wireless power was synonymous with beamed power and power harvested through solar cells or satellites where power was "beamed" down to earth in the microwave regime and converted to DC power using rectennas (antennas coupled to rectifying diodes). These techniques, however, faced problems with the amount of power, cost, size needed to generate meaningful power delivery at a faraway point, as could be seen from the Raytheon helicopter experiment of 1964 or the Solar Powered Satellites (SPS). Relatively high efficiencies were obtained (ĩ91%); however, these systems were bulky and sensitive to small changes in alignment (due to their directive nature) [Brown, 1996]. These also suffered from the so-called "thinned-array curse"[2].

Even as the aforementioned disadvantages made long-distance WPT problematic, short distance WPT through induction, especially for medical devices began gaining prominence. This was followed by a widespread interest in WPT and especially resonant mode coupling thanks to an experiment by a group of researchers at the Massachusetts Institute of Technology (MIT) Kurs et al. [2007] that resulted in the founding of their startup called "WiTricity". The theoretical aspects of their paper (among others) and contemporary research trends will be presented in the next chapter.

---

[1]The incomplete Wardenclyffe Tower was a testament to his resolve to this extent.
[2]http://en.wikipedia.org/wiki/Thinned-array_curse

1.2 Motivation

So far we have seen that there exists a very real need for an efficient and scalable WPT system. As will be shown in the next chapter, most of the research focus has been on achieving a high Power Transfer Efficiency (PTE) and/or high Power Delivered to Load (PDL), resulting in somewhat complex systems of multiple coils and/or resonating structures. However, there's a need for a system design perspective while discussing WPT that is absent in the literature. While we will try to maximize PTE and PDL as well, the overarching goal in this thesis will be to see if some of these concepts can be viewed from a system optimization perspective, thus giving a holistic view of end-to-end system performance for a closed standalone system. This would mean the design of a power source that takes into account the effect of the load on its operating point. As will be shown later on in this thesis, this can be achieved by using proper design equations for a negative resistance oscillator used in a coupled resonator system.

1.3 Objectives

The objective of this project is to design a simplified wireless power transfer system that fulfills the following requirements:

- A high level of integration is desired so that the number of components, matching circuits, etc. can be absorbed or avoided.

- System complexity is minimal such that losses incurred in the signal chain are the lowest possible.

- A high transfer efficiency is a must; however, the overall power delivered to the load should be of most concern.

- System must be scalable in size and power.

- The source power generator should be able to track changes (small variations in frequency) due to any loading or coupling effects.

1.4   Thesis Organization

This thesis is divided into five chapters (including this one) and two appendices. Each chapter can be described as follows:

- Chapter 1 acts as an introduction to the thesis in terms of a general overview, its motivation, objectives and structure.

- Chapter 2 presents current research trends and introduces relevant theoretical concepts in WPT from various perspectives. Industrial standards and commercial efforts are highlighted as well. The theory of most WPT systems is handled briefly for systems in free space as well as in lossy (partially conductive) surroundings. The effect of magnetic or electric antennas surrounded in lossy media (such as for implanted devices) is derived and described.

- Chapter 3 deals with antenna design and proposes various types of antennas to handle different applications. The Electrically Coupled Loop Antenna (ECLA) is introduced here and some design iterations described through the means of full-wave simulations and fabricated prototypes. An equivalent circuit is also presented that aids in arriving at system objectives faster.

- Chapter 4 deals with embedding the antenna parameters developed in Chapter 3 into a complete WPT system and discusses oscillator design, integration issues and other considerations. The system is simulated as realistically as possible and measurements carried out to validate the results.

- Chapter 5 summarizes the most important thesis concepts and findings and establishes future lines of exploration.

- All academic references are provided in the Bibliography while some online resources are mentioned as footnotes throughout the thesis where relevant.

- Appendix A elaborates on the circuit simulation techniques used in Keysight (formerly Agilent) ADS (Advanced Design System) throughout the thesis. Some online references for non-linear design using ADS are also provided here.

- Appendix B is a compilation of the MATLAB codes used within the thesis.

Chapter 2

Literature Review and Theoretical Background

2.1 Research Trends and Theoretical Perspectives on Design

In this chapter, we will present some theoretical results that are used in contemporary research papers to study Wireless Power Transfer (WPT). A background of the literature is presented followed by some formulations for coupled resonators in general, followed by a theoretical framework for a comparison between magnetic and electric antennas for implanted applications.

2.1.1 Review of Trends and Types of WPT

In the previous chapter, we discussed the far-field WPT efforts in the later part of the 20th century. Here, we discuss some of the near-field techniques. There are mainly three types of coupling that can occur in the near-field, namely **inductive**, **capacitive** or **magneto-dynamic**[1]. The last two types of coupling are typically unfavorable for high-efficiency WPT as well as implanted applications due to the (a) high voltage (and consequently, **E**-field) required between

---

[1] http://en.wikipedia.org/wiki/Wireless_power

the resonators which violates safety norms [IEEE, 2010] and (b) moving parts can lead to a loss of energy while also being cumbersome to maintain.

Thus, inductive WPT is probably the most common form of WPT in current use. High levels of RF magnetic fields have not been found to have any major effects on human tissue as the tissues are lossy dielectrics and tend to react more adversely to comparable electric fields than they do for magnetic fields. Even for inductive WPT, we can think of **resonant inductive coupling** vs. regular inductive coupling (transformer action). In resonant coupling, the transmit and receive coils form resonators, either through added capacitors or their distributed self-capacitance. These are preferably synchronously tuned resonators and the theory of such coupled resonators can be analyzed in a number of ways. We will discuss a few of these techniques. Transformer coupling relies on the strong coupling between the primary and secondary due to the strong flux linkage between these coils, either due to winding techniques or by sharing the same core.

The way Kurs et al. [2007] conducted their experiment involved the use of four coils, two of which were coupled while the actual source and load circuits are inductively coupled to these *linked* coils. The load in this case was a 60 W bulb that was operated through the use of these linked coils (resonating at 10 MHz). As will be seen through sections below, the Quality factor (Q) of the coupled coils plays a big part in maximizing the Power Transfer Efficiency (PTE) of the system and therefore, there has been quite a lot of effort in increasing the Q of the coils by introducing more loops in the system [RamRakhyani and Lazzi, 2013]. Some have also studied the effect of having more than two loops [RamRakhyani et al., 2011] while yet others have derived figures of merit for systems with 2, 3 or more loops [Kiani and Ghovanloo, 2013, Kiani et al., 2011]. The thrust of most of these papers with multiple loops has been to use an inductive link extremely close to the body/skin to power an implanted microelectronic device (IMD) which relies on slightly stronger coupling effects than the loosely coupled resonant systems of [Karalis et al., 2008, Kurs et al., 2007]. The motivation for these efforts comes from the fact that in order to maximize the PTE or Power Delivered to Load (PDL) of the system, the reflection from the source and load loops must be minimized while maximizing the coupling between them. In some cases, having multiple loops increases the design flexibility by introducing

more degrees of freedom in choosing coil dimensions or Q[Wei et al., 2014]. Also, having parasitic loops in between the source and load coils increases the effective coupling distance [Karalis et al., 2010]. Even though Zierhofer and Hochmair [1996] showed the dependence of coil geometry on the efficiency of mainly inductive systems as early as 1996, there has been a significant upsurge of interest in coil geometry recently in the loosely-coupled regime since the MIT demonstration.

Researchers who have approached the system analysis aspect of WPT include Lee and Cho [2015, 2013] who studied the effect of multiple receivers on the transmitter and how the system can be better tuned by optimizing the load variations[2].

An important aspect of WPT that some articles fail to stress on is the d/r ratio which is the ratio of the distance between the loops, d, to the radius of the minimum sphere containing any one loop, r (Clearly valid only for identical loop sizes.). This is crucial to understanding the relative success of one technique over another as one can achieve arbitrarily high values of transfer efficiency by having a large transmit coil. For example, in the MIT work, a $d = 3r$ range is chosen which establishes the regime as near-field and loosely-coupled. Hence, to better understand the overall system efficiency (as given by the PDL which in the case of the MIT research was 20% from wall to bulb). The choice of an appropriate operating frequency is also essential for the design of antennas of adequate form factor [Poon et al., 2007]. For example, for implanted applications, one needs to choose a high enough frequency so that a physically small antenna is electrically large enough at resonance while the effect of the lossy nature of human tissue be kept minimal. Hence, a band like the Medical Implant Communication Service (MICS) band (402 - 405 MHz) is ideal. Some results on the frequency effects for implanted antennas are studied later in this chapter.

---

[2]An interesting point here is that some researchers seem to have RF Identification (RFID) and energy harvesting ideas confused with WPT. Whereas the former relies on scattering mechanisms, the degree of coupling and power is very weak when compared to the latter. Also, while a scattering based analysis is indeed possible with coupled resonators of WPT, it is usually best to think of these as two quite separate phenomena at the risk of confusing the reader.
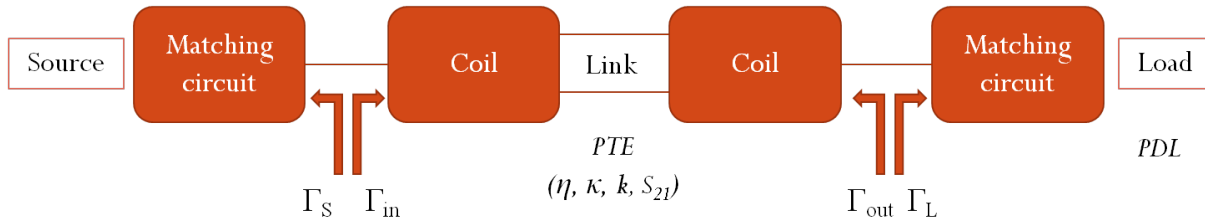
FIGURE 2.1: Overall system performance metrics
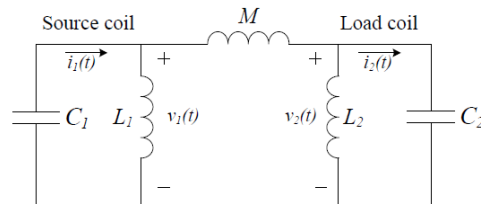
FIGURE 2.2: Coupled LC tank circuit system (Wei, X., Wang, Z., and Dai, H. (2014). A critical review of wireless power transfer via strongly coupled magnetic resonances. Energies, 7(7):4316-4341. Used under fair use, 2015.)

2.1.2 Coupled-Mode Theory

The Coupled-Mode Theory (CMT) formalism is used extensively in opto-electronics, optical guides and by physicists in general [Haus et al., 1984, Pollock, 1995][3]. CMT is a perturbational approach by which a coupled second-order differential equation can be decoupled to simpler first-order equations by means of a complex amplitude term. In general, a mode can mean many different things in physics, for example propagation modes, resonant or normal modes of vibration, polarization states, etc.[4]. In the specific case of WPT analysis, it is easier to visualize the mode quantity as a resonant mode of an LC resonator[Haus et al., 1984]. Thus, considering Fig. 2.2, we can define the following terms

---

[3]This is probably why it was the MIT researchers' choice of analysis as they were physicists too.
[4]http://emlab.utep.edu/ee5390em21/Lecture%205%20--%20Coupled-mode%20theory.pdf

$$v = L\frac{di}{dt} \tag{2.1}$$

$$i = -C\frac{dv}{dt} \tag{2.2}$$

$$\frac{d^2v}{dt^2} + \omega_0^2 v = 0 \tag{2.3}$$

where

$$\omega_0^2 = \frac{1}{LC}$$

Let $a_\pm$ be some complex amplitude such that

$$a_\pm = \sqrt{\frac{C}{2}}\left(v \pm j\sqrt{\frac{L}{C}}i\right) \tag{2.4}$$

$$\frac{da_+}{dt} = j\omega_0 a_+ \tag{2.5}$$

$$\frac{da_-}{dt} = -j\omega_0 a_- \tag{2.6}$$

Here, these amplitudes can be seen to hold the energy of the circuit when their magnitude is squared ($|a_\pm|^2 = W$). The $\pm$ subscript for amplitudes denotes the positive and negative frequency components of the mode. Most discussions do not generally use the negative term as it is just the complex conjugate of the positive term [Haus et al., 1984].

Also, Γ is used to denote the damping factor of the lossy resonators (and not the reflection coefficient as in S-parameter analysis!), for both intrinsic and external loss/decay and is thus tied to the Quality factor of the loops. For a lossy tank circuit, if unloaded Q is

$$Q_{unloaded} = \frac{\omega}{2\Gamma} = \frac{\omega L}{R}$$

then

$$\Gamma = \frac{R}{2L}$$

We can now introduce the coupling between these modes by κ, which is often used in CMT-based analyses to denote the coupling coefficient between modes [Kurs et al., 2007] (k may also be used with subscripts [Kim, 2012].). If a_1 and a_2 represent the mode amplitudes of the uncoupled resonators seen in Fig. 2.2,

$$\frac{da_1}{dt} = j\omega a_1 + \kappa_{12}a_2 \tag{2.7}$$

$$\frac{da_2}{dt} = j\omega a_2 + \kappa_{21}a_2 \tag{2.8}$$

κ_{12} and κ_{12} denote the coupling between the modes 1 and 2. Note that this is for the lossless case and for the more general lossy case, the intrinsic decay rate for the resonators as well as the matching loss must be considered [Wei et al., 2014][5].

Now that we have defined some basic terms and have a general idea of the formalism, from Karalis et al. [2008] and Kim [2012] we see that we can define some system design parameters to maximize the PTE and/or PDL by optimizing certain quantities in a complete, coupled WPT system to obtain

---

[5]There are quite many details that are left out in this discussion for the sake of a simple review and the reader is advised to derive these relations from the references provided.

$$U = \frac{\kappa}{\sqrt{\Gamma_1 \Gamma_2}} = K_U \sqrt{Q_1 Q_2} \tag{2.9}$$

$$\text{where } K_U = \frac{M}{\sqrt{L_1 L_2}} \tag{2.10}$$

$$U_{opt} = \sqrt{1 + U^2} \tag{2.11}$$

$$\eta_{opt} = \left(\frac{U}{1 + \sqrt{1 + U^2}} \right)^2 \tag{2.12}$$

Here, U and K_U are intermediate variables that are used in the optimization of the overall transfer efficiency. Thus, the optimum efficiency (η_{opt}) is achieved when the above criterion is achieved, which can be seen to be dependent on the quality factors of the coils. Due to physical limitations, there is a need to equalize the source and load resistances to guarantee optimal performance, failing which we are stuck with sub-optimal efficiency [Kim, 2012]. This means that some sort of controllable input impedance network should be aimed for (which we will design in the next few chapters). As discussed previously, more degrees of freedom are obtained by increasing the number of loops in the system. It will be shown in Chapter 3 that the value of coupling coefficient is very low for loosely coupled systems, and thus high-quality factor loops are an implicit requirement for achieving high PTE. Also, it is possible to develop an understanding for over, under, or critically-coupled resonators by looking at the value of U.

2.1.3 Filter Theory

From Hong and Lancaster [2004], we can define the Filter/circuit Theory (FT) perspective on coupled resonators. The analysis given here is limited to the magnetic coupling of two coupled resonators. Even though this perspective might seem more intuitive to engineers due to our predisposition to work with circuit elements, in some cases it may be difficult to arrive at a valid equivalent circuit, such as in the case of antennas used as couplers (this problem will be overcome in the next chapter). From Fig. 2.3, at reference planes $T_1 - T_1'$ and $T_2 - T_2'$, we have
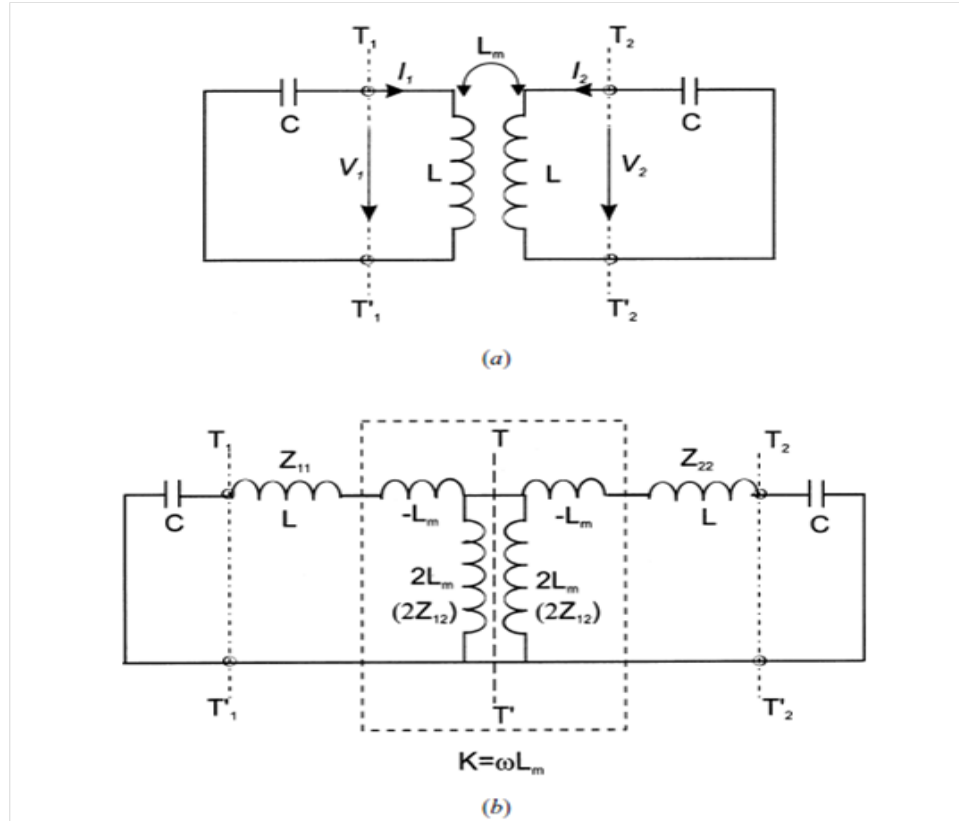
FIGURE 2.3: Equivalent circuit for magnetically coupled resonators (Hong, J.-S. G. and Lancaster, M. J. (2004). Microstrip filters for RF/microwave applications, volume 167. John Wiley & Sons. Used under fair use, 2015.)

$$V_1 = j\omega L I_1 + j\omega L_m I_2 \tag{2.13}$$

$$V_2 = j\omega L I_2 + j\omega L_m I_1 \tag{2.14}$$

$$f_e = \frac{1}{2\pi\sqrt{(L - L_m)\,C}} \tag{2.15}$$

$$f_m = \frac{1}{2\pi\sqrt{(L + L_m)\,C}} \tag{2.16}$$

where L_m is the mutual inductance and L, C are the equivalent inductance and capacitance respectively when the resonator is self-resonant and isolated (decoupled). Also, f_e, f_m are the frequencies due to the shift in the stored flux as given in Hong and Lancaster [2004] (Subscripts

e and m represent the insertion of an electric/magnetic wall for analysis.). Then, the magnetic coupling coefficient is given by

$$k_M = \frac{f_e^2 - f_m^2}{f_e^2 + f_m^2} = \frac{L_m}{L} \tag{2.17}$$

This may also be seen as the even and odd mode coupling as shown in Heebl et al. [2014], Kim et al. [2010] where even and odd modes are considered to be the modes above and below the resonant frequency in the isolated (non-coupled) case. Typically, this splitting is limited to the strongly-coupled regime and both modes coalesce in the loosely-coupled regime.

Note that this is the case for synchronously tuned filters and that for the more general asynchronous cases, this is but a degenerate case. From the formulation above, we can see that it is possible to extract the coupling coefficient [Kim et al., 2010] and/or quality factor information from coupled resonator system to study it further (using both magnitude and phase information of S_{21}). This is especially useful for implanted applications where the effect of the body on the resonators is not quite clear or well understood.

2.1.4 Comparison

Useful side-by-side comparisons of the circuit-theoretic and the CMT approach are given in Hui et al. [2013], Kiani and Ghovanloo [2012], Kim [2012]. Wei et al. [2014] bring out the state of the art in terms of both theories and clearly demarcate which theory is better suited for the application at hand while also discussing various system architectures. An interesting result that follows from this analysis is that both approaches are perfectly valid ways of approaching the problem with no perceived benefit of one over the other as long as the physics for the assumptions (near-field conditions) hold true. It is important to realize that CMT is a perturbational approach and that it is valid only when the first few modes are the most dominant, which is the case for loosely coupled WPT systems. The circuit theory model, albeit simple and straightforward, suffers from the problem of relying on fixed network parameters. For

example, any change in the load network would require a re-work of the calculations which may seem tedious and impractical for real-time applications (changing load conditions).

Azad et al. [2012] have achieved a Friis equation-like formulation for the near-field coupling but the near-field equation here is a misnomer as the approach is still derived from an equivalent circuit method. It is not *truly* from an antenna perspective. Although the objective of this thesis is not to present a complete theoretical formulation for the near field behavior of the coupling antennas, we will strive to analyze the system from an antenna perspective where and when possible with possible segue into an equivalent circuit to understand the system from a more established/conventional circuit perspective as well.

2.2 Overview of Industrial Standards

The main objective of this section is to understand contemporary commercial WPT schemes. At 100 kHz, the Qi standard published by the Wireless Power Consortium (WPC) is a form of non-resonant inductive coupling. Its specifications are maintained by the WPC (currently at v1.1.2) and split into three possible regimes: Low, Medium and High power. Currently only low power (5 W) exists in the market. Efforts are ongoing to realize medium power devices (up to 120 W) commercially. High power operation has not been standardized yet. Qi includes a communication protocol that enables WPT control by a mobile device. It requires low standby power and has a typical operating distance of 5̃ mm for device size of about 40 mm. Other such inductive methods include Duracell's Powermat technology.

Qi is by far the most wide-spread of WPT schemes. It incorporates "foreign object detection" which prevents heating of metal objects in the neighborhood of an active transmitter. Some Qi-specific terms are given below.

Qi - Guided vs Free positioning

Guided Positioning - User must actively align the Secondary Coil to the Primary Coil, by placing the Mobile Device on the appropriate location of the Interface Surface. The mobile device provides an alignment aid that is appropriate to its size, shape and function.

Protocols	Power Frequency band	Communication Frequency band	Tightly coupled Tx & Rx	Spatial Freedom (x/y/z)
Wireless Power Consortium (WPC)	100 – 205 KHz	Same (in band communication)	Yes (no magnet)	Yes Adaptive resonance
Powermat	277 – 357 KHz	Same (in band communication)	Yes (with magnet)	No
Alliance for Wireless Power (A4WP)	6.78 MHz	2.4 GHz ISM (ZigBee or BTLE?)	No	Yes Magnetic resonance
Intel	13.56 MHz	?	No	Yes Magnetic resonance
Eurobalise	27.095 MHz	Same (down link) 4.234 MHz (up-link)	No	Yes, at high speed

(a) Technical Considerations

	100 - 500 kHz	6.78 / 13.56 27 MHz ISM	notes
Human RF exposure	Best	Good	<500KHz has more headroom for compliance to SAR and Efield safety limits
EMC radiation	Good	Unproven	<500KHz pass FCC part15/18 and CISPR11 requirements. 6.78MHz not yet proven; ISM bandwidth tolerance is very narrow 15KHz
Interference with NFC and other electronic devices	Best	Good	Induced voltage in nearby metallic objects or PCB is proportional to frequency. NFC, key fob intereference can be managed
Efficiency / Transmission range	Good	Good	<500kHz has better circuit efficiency 6.78MHz has better coil efficiency Both achieve similar transmission range
System cost	Good	Good	6.78MHz requires higher voltage and more complex FETs. <500KHz has more complex coils for similar freedom of placement

(b) System Considerations

FIGURE 2.4: Comparison of useful parameters used in contemporary industrial designs

Free Positioning - makes use of an array of Primary Coils to generate a magnetic field at the location of the Secondary Coil only. Another implementation uses mechanical means to move a single Primary Coil underneath the Secondary Coil.

Communication between transmit and receive coils takes place through a digital ping in Qi which makes use of backscatter modulation (Differential bi-phase bit encoding like that used in RFID systems)

Other WPT schemes include **WiTricity**[6] which is based on the work by Karalis et al. [2008], Kurs et al. [2007]. Competing technologies are **Intel's Wireless Resonant Energy Link (WREL)**[7] (operating at 13.56 MHz) and **Alliance 4 Wireless Power's (A4WP) Rezence** technology (operating at 6.78 MHz). On February 11 2014, A4WP and **Power Matters Alliance** (PMA) announced plans for co-operative growth and inter-operable standards. Fig. 2.4[8] gives an idea of the relative pros and cons of each of this technologies and a qualitative idea of the suitability of their operational frequencies for various purposes. **Qualcomm** has also been involved with electric vehicle charging with its project called **Halo** (possible collaboration with Tesla Motors) as well as other applications of WPT [Mohammadian, 2009, Toncich et al., 2009].

2.3 Implanted Antennas: Electric vs. Magnetic Antennas in Lossy Media

Due to the steady rise in demand for implantable devices in recent years, the issue of power transfer to these devices warrants a study into the suitability of certain antennas over others. This problem is studied in this section where theoretical results are developed to promote the candidacy of magnetic antennas over electric antennas specifically in the case of implanted applications.

---

[6]http://www.witricity.com/assets/highly-resonant-power-transfer-kesler-witricity-2013.pdf

[7]http://newsroom.intel.com/docs/DOC-1119

[8]https://community.freescale.com/community/the-embedded-beat/blog/2012/11/30/wireless-power-technology-comparison

In this section, the near-field radiation characteristics of electric and magnetic antennas when surrounded by a lossy dielectric medium are described. This study is relevant for cases such as implanted antennas, submarine or underground communications where the antenna's near-field consists of lossy dielectric media such as human tissues, minerals or saline water. Theoretical results for both types of small antennas are presented and expressions to show the difference in stored energy and radiated power in the radian sphere [Wheeler, 1959] around the antenna are formulated. These "ideal" results are then validated using simulation results from a center-fed small dipole and a small loop antenna as a dual of magnetic dipole. It will be shown that magnetic antennas give much better performance when surrounded by a lossy dielectric[9].

2.3.1 Overview and Motivation

The study of the near-field of antennas is of great significance in applications where the antenna is located next to or inside a lossy medium because the medium properties can greatly alter the performance of the antenna while themselves being subject to effects such as dielectric heating and magnetization. This is typically the case for antennas near the human body [Kim and Rahmat-Samii, 2004], soil [Large et al., 1973], submarine [Wheeler, 1958], or other lossy media. In order to reduce the time-to-market, an antenna designer may choose a simple design; however, this choice needs to take into consideration the nature of the surrounding medium. It will be shown that antenna performance in a lossy medium is directly linked to whether it has a dominant electric or magnetic field intensity in the near-zone. This study focuses on the specific case of how antennas in implanted medical devices are affected by the presence of the human body.

The demand for smart implanted medical devices has been growing exponentially during the last few decades [Hall and Hao, 2006, Zimmerman, 1996]. Most modern implanted devices are able to receive commands from the outside world or relay information from various sensors within the host body. Thus, it can be seen that implanted antennas will play a significant role

---

[9]The material given in this section is incorporated from the paper by Manteghi and Ibraheem [2014] to which the author contributed.

in the future of healthcare technology. However, there are many challenges involved in the design of implanted antennas, including but not limited to: antenna miniaturization, antenna loss due to miniaturization (structural loss), radiation loss that manifests itself in the immediate near-field (environmental or near-field loss), compatibility with the human tissues, detuning, etc. The goal of this study is to investigate losses that arise inside a conductive medium (such as the human body) due to the strong reactive and radiating near-field for two main classes of small antennas: electric antennas and magnetic antennas. Antennas in lossy media and near material half-spaces have been studied in detail in King et al. [1981], Smith [1984] but the focus here is on the use of electrically small antennas with highly reactive near fields specifically with a focus on biomedical or implanted device applications.

Electrically Small Antennas

Previous research by Wheeler [Wheeler, 1947, 1975], Chu [Chu, 1948], Harrington [Harrington, 1960] and others [Collin and Rothschild, 1964, Davis et al., 2011, McLean, 1996] has focused on the physical limitations of antennas with regard to size, gain, directivity, quality factor, and the interdependence of these quantities. Karlsson [2004] and Wait [1952] have investigated antennas surrounded by a lossy or conducting medium, but with a focus on finding optimal values for antenna gain and radiation efficiency. To the best of the authors' knowledge, a study of the effect of the surrounding lossy media in the near-field based on the type of antenna has not been conducted before. This issue, with a focus on electrically small antennas [Wheeler, 1975], is addressed at length in this study by computing the power loss and radiated power for electric and magnetic antennas. Especially in the case of implanted devices, the power lost in the near-field goes into heating human tissues which needs to comply with standards set by government agencies. Through analytical expressions and simulations, the case for magnetic antennas will be made by comparing the power dissipated in the lossy medium and the radiated power for electric and magnetic antennas.

(a) Antenna loss regimes   (b) Ideal dipole surrounded by a lossy medium
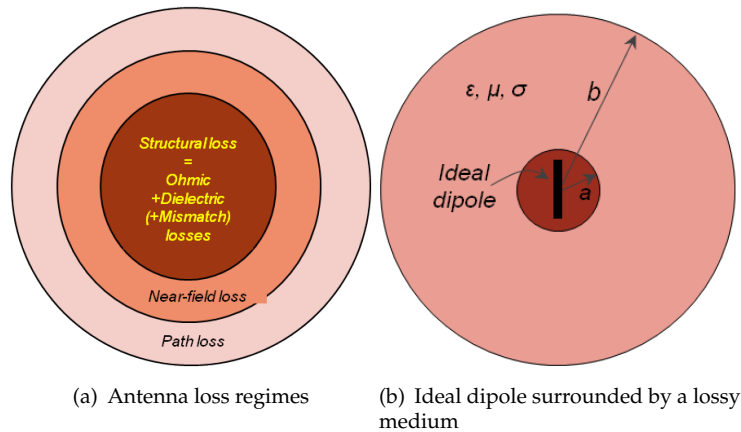
FIGURE 2.5: Antenna Losses

Loss Mechanisms

- **Strucural Loss**: The structural loss of an antenna, which is converted to thermal energy, can be seen as the ohmic and dielectric losses of the antenna structure itself regardless of whether the antenna is surrounded by free space [Jungsuek and Sarabandi, 2012], lossy media, or any other type of medium (see Fig. 2.5). Arbabi and Safavi-Naeini [2012] approached this problem for optimizing maximum gain. Unlike electrically large antennas such as reflectors, structural loss is an important factor in the overall loss of electrically small antennas [Wheeler, 1947, 1975]. These losses can be minimized during the antenna design stage. If the antenna is made of a perfect electric conductor, PEC, and perfect dielectric material, the structural loss of an antenna can theoretically go to zero. The antenna still might have return loss which is not converted to further thermal energy. Structural and mismatch losses are not considered in this study.

- **Near-field Loss**: The reactive near-field of an antenna is strongly coupled to the current distribution on the antenna structure. Therefore, any disturbance in the reactive near-field will affect the current distribution and input impedance of the antenna. If the antenna is surrounded by a lossy material, the reactive near-field will contribute to the antenna overall loss. The loss associated with the reactive near-field of the antenna,

which is converted to thermal energy in the surrounding material, is termed environmental or near-field loss in this study. There are some limits on the amount of thermal energy generated by an implanted transmitter which are set by regulatory bodies such as the United States Federal Communications Commission (FCC) and the European Radio-communications Committee (ERC) which is usually characterized by the term Specific Absorption Rate or SAR. According to the FCC and ERC, the maximum limits for SAR averaged over 1g and 10g of tissue mass are 1.6 W/kg [Federal Communications Commission, 1996] and 2 W/kg, respectively [Commission, 1995]. The question is how does the antenna type affect the total radiated power for a given antenna size while still satisfying the FCC limits? Results of an investigation into this problem are studied in this section of the thesis.

- **Path Loss**: It is well known that the radiated fields of any antenna in the far zone is a locally plane wave. For a plane wave, the ratio of electric field to the magnetic field is dictated by the material properties in the far-field and not the antenna type. However, the ratio of total electric field to the total magnetic field in the reactive near zone of a small antenna can vary from a very small number (0 for a magnetic point source at the origin) to a very large number (infinity for an electric point source at the origin). Thus, it is clear that the reactive near-field of a small antenna can vary dramatically from one antenna type to another based on the radiation mechanism. Since the reactive near-field of a small antenna is strongly coupled to the antenna structure, it is beneficial to define antenna loss in the reactive near zone as an antenna-dependent environmental loss which can be distinguished from the structural loss mentioned above. At the same time, one can distinguish the near-field environmental loss from the path loss which usually deals with plane waves (far-field) and will be independent of the antenna type.

2.3.2 Theoretical Results

For simplicity, two ideal dipoles (an electric dipole and a magnetic dipole) will be analyzed in a homogeneous lossy medium with a finite conductivity (or dielectric loss). The exact total

field of these two antennas can be found analytically, and therefore, one will be able to compare their near-field stored energy, radiated power and dissipated power in the closed form. This analysis allows us to study the behavior of small antennas in a lossy medium without concerning ourselves with the antenna design, mismatch issues, and the antenna structural loss. However, note that the approach used here is a perturbational method as the concept of effect of the antenna size on near-zone fields is studied through a normalization of the power flowing through an imaginary sphere (of varying size) and thus the results presented here are an approximation of the expected performance.

- **Ideal Dipoles**

  Consider a homogeneous medium with permittivity, permeability and conductivity of ϵ, μ and σ respectively. An electric (or magnetic) dipole of length Δz, carrying a uniform current I (or K) in the z direction, is located at the origin. One can find the electric and magnetic fields of these dipoles from Jin [2011] as

$$
\begin{cases}
\mathbf{E}_E = \frac{j\Delta z \mu \omega I e^{-r\gamma}}{4\pi r^3 \gamma^2} \left(2\left(1 + r\gamma\right) \cos\left(\theta\right) \hat{r} + \left(1 + \gamma r + \gamma^2 r^2\right) \sin\left(\theta\right) \hat{\theta} \right) \\
\mathbf{H}_E = \frac{\Delta z I (1 + r\gamma) e^{-r\gamma} \sin(\theta)}{4\pi r^2} \hat{\phi}
\end{cases}
\tag{2.18}
$$

$$
\begin{cases}
\mathbf{E}_M = \frac{\Delta z K (1 + r\gamma) e^{-r\gamma} \sin(\theta)}{4\pi r^2} \hat{\phi} \\
\mathbf{H}_M = \frac{j\Delta z K e^{-r\gamma}}{4\pi \mu \omega r^3} \left(2\left(1 + r\gamma\right) \cos\left(\theta\right) \hat{r} + \left(1 + \gamma r + \gamma^2 r^2\right) \sin\left(\theta\right) \hat{\theta} \right)
\end{cases}
\tag{2.19}
$$

  where

$$
\gamma = \alpha + j\beta = \sqrt{j\omega\mu\left(j\omega\varepsilon + \sigma\right)}
\tag{2.20}
$$

with

$$\alpha = \omega \sqrt{\frac{\varepsilon\mu}{2}} \sqrt{-1 + \sqrt{1 + \frac{\sigma^2}{\varepsilon^2\omega^2}}} \tag{2.21a}$$

$$\beta = \omega \sqrt{\frac{\varepsilon\mu}{2}} \sqrt{1 + \sqrt{1 + \frac{\sigma^2}{\varepsilon^2\omega^2}}} \tag{2.21b}$$

The electric field intensity is proportional to the inverse of r^2 for the magnetic dipole in the near-zone while it is proportional to inverse of r^3 for the electric dipole. It means that $\mathbf{E} \cdot \mathbf{E}^*$ in the near-zone is proportional to $1/r^4$ and $1/r^6$ for magnetic and electric dipoles, respectively. Therefore, the ohmic loss associated with conductance, σ, of the medium will be higher for an electric dipole in comparison to a magnetic dipole.

In order to proceed with these calculations, the input impedances of the antennas need to be found to be able to feed both antennas with the same amount of power. Since the surrounding lossy dielectric loads the antennas in different fashions, the antenna impedances will not be similar to its respective free space input impedance. At the same time, a finite thickness for both dipole antennas would need to be included to avoid field singularities, and consequently, numerical solutions are required to proceed. However, there is an alternative way to compare the performance of these two antennas in a lossy medium. To avoid impedance computation and field singularities, we assume that the antenna is located in an imaginary small sphere of radius a that just encloses the antenna and generates the same field distribution outside of that sphere as the ideal dipole in a homogeneous medium (see Fig. 2.5). As mentioned previously, we omit the stored energy and any loss inside the small sphere of radius a as it represents the antenna's structural loss, similar to the assumptions made by Chu [1948].

- **Power lost inside a lossy sphere**

  The electromagnetic power lost in a homogeneous lossy dielectric spherical shell with an inner radius of a and an outer radius of b is computed as
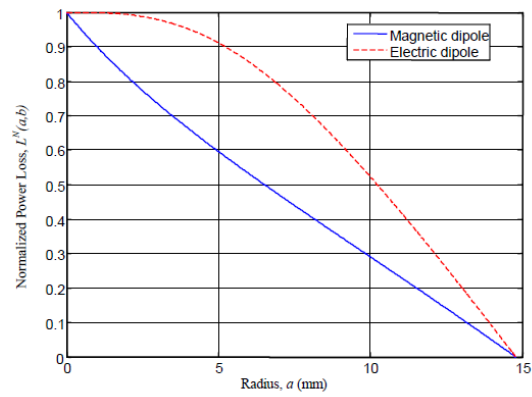
(a)
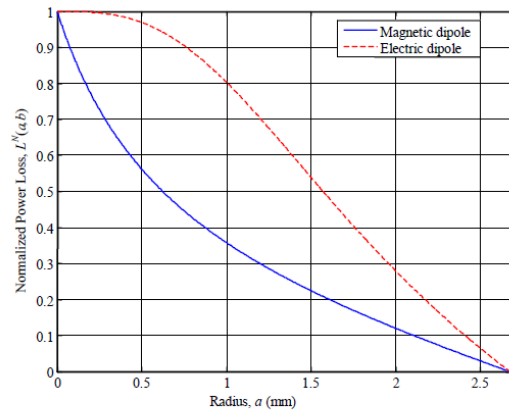
(b)
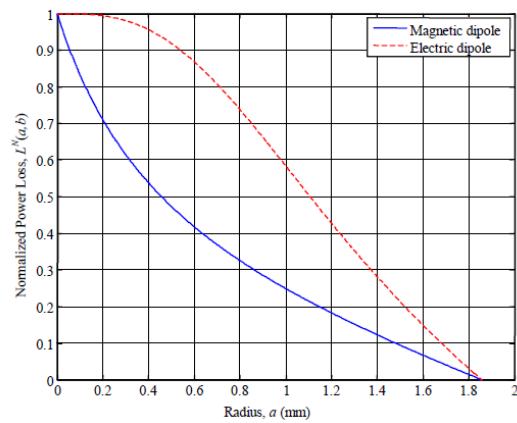
(c)

FIGURE 2.6: Normalized power loss for muscle tissue inside radian sphere of (a) radius, $b = 14.5$ mm at 403 MHz (b) radius, $b = 2.7$ mm at 2.4 GHz and (c) radius, $b = 1.9$ mm at 3.5 GHz

TABLE 2.1: Values of Dielectric Constant and Effective Conductivity For Various Human Tissues at Different Frequencies

Tissue	Frequency (MHz)	Dielectric Constant, ϵ_r	Conductivity, σ
Muscle	403	57.95	0.81
	2400	53.6	1.81
	3500	52.12	2.72
Fat	403	11.62	0.081
	2400	10.82	0.27
	3500	10.5	0.42
Cerebro-Spinal Fluid	403	70.96	2.25
	2400	66.32	3.41
	3500	64.58	4.57

$$L(a,b) = \int_0^{2\pi} \int_0^{\pi} \int_a^b \frac{1}{2}\sigma \mathbf{E}(\mathbf{r}) \cdot \mathbf{E}^*(\mathbf{r}) r^2 \sin(\theta) \, dr d\theta d\varphi \tag{2.22}$$

It is worth noticing that the electric energy can be computed in a fashion similar to this equation by replacing σ by $\epsilon/2$. To show the significance of the near-zone antenna loss, we compute the antenna loss within the radian sphere ($\beta b = 1$) for different a, and normalize it to the total power lost in the lossy material if it were to extend infinitely (It will be shown in the next section that the total loss is equal to the total energy passing through the sphere of radius a). The assumption is that the antenna size, $2a$, is smaller than the radian sphere which is a condition for small antennas. In the rest of this study, a will be used as the radius of a sphere enclosing the antenna structure.

The power lost for a magnetic dipole in a lossy medium from a to an arbitrary b is

$$L_M\left(a,b\right) = \frac{\Delta z^2 |M|^2 \sigma}{24\pi\alpha}\left(\mathrm{e}^{-2\alpha a}\frac{2\alpha + \left(\alpha^2 + \beta^2\right)a}{a} - \mathrm{e}^{-2\alpha b}\frac{2\alpha + \left(\alpha^2 + \beta^2\right)b}{b}\right) \qquad (2.23\mathrm{a})$$

$$\simeq \frac{\Delta z^2 \mathrm{e}^{-2\alpha a}|M|^2 \sigma\left[2\alpha + \left(\alpha^2 + \beta^2\right)a\right]}{24\pi\alpha a}\Bigg|_{b\to\infty} \qquad (2.23\mathrm{b})$$

Normalizing, we get

$$L_M^{(N)}(a,b) = \frac{L_M(a,b)}{L_M(a,\infty)} = 1 - \frac{a\mathrm{e}^{-2(b-a)\alpha}\left(2\alpha + \left(\alpha^2 + \beta^2\right)b\right)}{b\left(2\alpha + \left(\alpha^2 + \beta^2\right)a\right)} \qquad (2.24)$$

The power lost for an electric dipole in a lossy medium from a to arbitrary b is

$$L_E\left(a,b\right) = \frac{\Delta z^2 |I|^2 \mu^2 \sigma\omega^2 \mathrm{e}^{-2(a+b)\alpha}}{24a^3 b^3 \pi\alpha(\alpha^2 + \beta^2)^2} \times \left[b^3\mathrm{e}^{2b\alpha}f\left(\alpha,\beta,a\right) - a^3\mathrm{e}^{2a\alpha}f\left(\alpha,\beta,b\right)\right] \qquad (2.25\mathrm{a})$$

$$\simeq \frac{\Delta z^2 |I|^2 \mu^2 \sigma\omega^2 \mathrm{e}^{-2\alpha a}f\left(\alpha,\beta,a\right)}{24\pi\alpha(\alpha^2 + \beta^2)^2 a^3}\Bigg|_{b\to\infty} \qquad (2.25\mathrm{b})$$

Normalizing, we get

$$L_E^{(N)}(a,b) = \frac{L_E\left(a,b\right)}{L_E\left(a,\infty\right)} = 1 - \frac{a^3\mathrm{e}^{-2(b-a)\alpha}f\left(\alpha,\beta,b\right)}{b^3 f\left(\alpha,\beta,a\right)} \qquad (2.26\mathrm{a})$$

$$\text{where} f\left(\alpha,\beta,r\right) = 2\alpha + 4\alpha^2 r + 2\alpha\left(\alpha^2 + \beta^2\right)r^2 + \left(\alpha^2 + \beta^2\right)^2 r^3 \qquad (2.26\mathrm{b})$$

These normalized ratios are plotted in Fig. 2.6 for a typical muscle tissue at 403 MHz, 2.4 GHz and 3.5 GHz (see Table. 2.1 for material properties [Gabriel et al., 1996] as a function of a for an electric dipole and a magnetic dipole in a radian sphere ($b = 1/\beta$) for each frequency.

As Fig. 2.6(a) shows, almost 91% of the power is dissipated in the radian sphere ($b = 14$ mm) for the electric dipole with $a = 5$ mm (antenna size 10 mm). The same ratio is 60%

for a magnetic antenna. It will be shown that outside of two radian spheres ($b = 2/\beta$), the wave impedance approaches intrinsic impedance of the medium and the antenna type does not affect the loss dramatically in this region.

- **Radiated Power**

  In addition to the electromagnetic loss due to σ, the Poynting vector variations can also be computed. One can find the real part of the radiated power passing through a sphere of radius r as

$$P^{rad}(r) = \int_0^{2\pi} \int_0^{\pi} \frac{1}{2} \mathrm{Re}\left[\mathbf{E} \times \mathbf{H}^*\right] \cdot \hat{r} r^2 \sin(\theta)\, d\theta d\varphi \tag{2.27}$$

The total radiated power of these antennas would be equal for a lossless medium ($\sigma = 0$) if

$$M = \eta I \tag{2.28}$$

where η is the intrinsic impedance of the lossy material in which the antenna is placed.

To compare the radiation performance of ideal electric and magnetic dipoles in a lossy material, one can compute the real part of the radiated power passing through a sphere of radius r as

$$P_M^{rad}(r) = \frac{\Delta z^2 \mathrm{e}^{-2\alpha r}|M|^2 \beta \left[2\alpha + \left(\alpha^2 + \beta^2\right) r\right]}{12\pi r \mu \omega} \tag{2.29}$$

$$\simeq \left. \frac{\Delta z^2 \mathrm{e}^{-2\alpha r}|M|^2 \beta \left(\alpha^2 + \beta^2\right)}{12\pi \mu \omega} \right|_{r \to \infty} \tag{2.30}$$

$$P_E^{rad}(r) = \frac{\Delta z^2 \mathrm{e}^{-2\alpha r}|I|^2 \beta \mu \omega}{12\pi r^3 (\alpha^2 + \beta^2)^2} f(\alpha, \beta, r) \simeq \left. \frac{\Delta z^2 \mathrm{e}^{-2\alpha r}|I|^2 \beta \mu \omega}{12\pi} \right|_{r \to \infty} \tag{2.31}$$

In order to make a fair comparison between these two antennas, the radiated power needs to be normalized to the input power. As we ignore the effects of structural and mismatch losses in this study, we will define input power as the total real power that passes through a sphere of radius a. As the medium in which the antenna resides is lossy, the entire input power will be absorbed when $b \to \infty$ (i.e. the far-field).

$$P_M^{(N)}(r,a) = \frac{P_M^{rad}(r)}{P_M^{rad}(a)} = \frac{e^{-2\alpha(r-a)}a\left[2\alpha + \left(\alpha^2 + \beta^2\right)r\right]}{r\left[2\alpha + \left(\alpha^2 + \beta^2\right)a\right]} \tag{2.32}$$

$$P_E^{(N)}(r,a) = \frac{P_E^{rad}(r)}{P_E^{rad}(a)} = \frac{e^{-2\alpha(r-a)}a^3 f(\alpha,\beta,r)}{r^3 f(\alpha,\beta,a)} \tag{2.33}$$

where

$$P_M^{rad}(a) = L_M(a,\infty) \qquad \text{and} \qquad P_E^{rad}(a) = L_E(a,\infty)$$

Equations 2.32 and 2.33 provide the total radiated power passing through a sphere of radius r normalized to the input power for magnetic and electric ideal dipoles, respectively. The normalized power is plotted versus a and distance r for a lossy dielectric mimicking muscle at 403 MHz (with material properties seen in Table. 2.1) in Fig. 2.7. The radian sphere has a radius of b = 14 mm at this frequency.

Fig. 2.7 demonstrates the superior performance of a magnetic antenna in comparison to an electric antenna with the same size and the same input power. It can be observed from these two figures that the difference between these two antennas is greater for a smaller antenna size.

The ratio of the normalized power of these two antennas for different a will provide a measure to compare the behavior of an ideal magnetic dipole to an ideal electric dipole versus frequency, material loss, and antenna size.

$$\frac{P_M^{(N)}(r,a)}{P_E^{(N)}(r,a)} = \frac{r^2 f(\alpha,\beta,a)\left[2\alpha + \left(\alpha^2 + \beta^2\right)r\right]}{a^2 f(\alpha,\beta,r)\left[2\alpha + \left(\alpha^2 + \beta^2\right)a\right]} \tag{2.34}$$
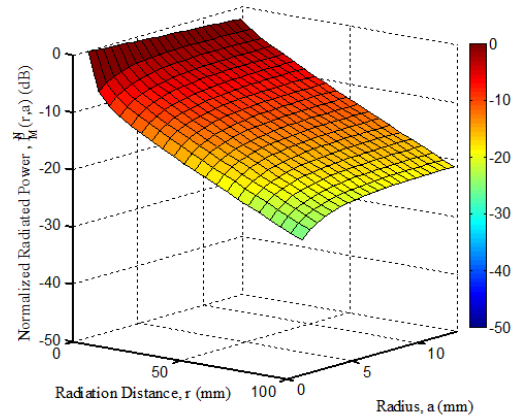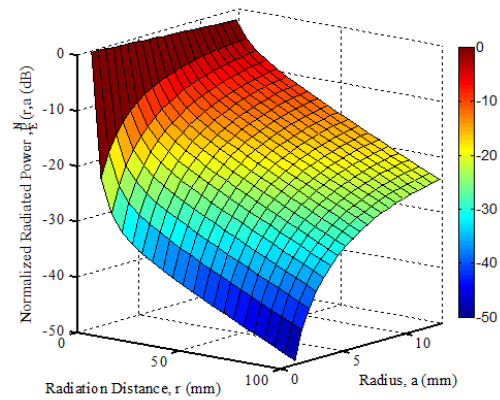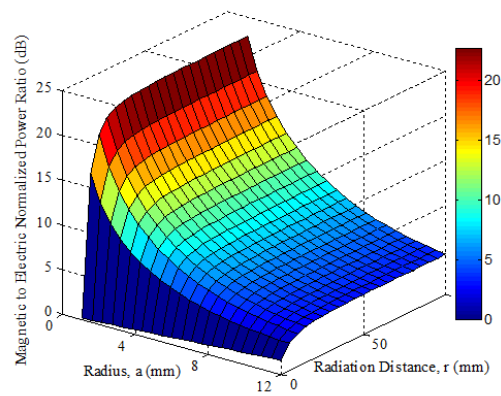
FIGURE 2.7: Normalized radiated power ratio, $P^{(N)}(r, a)$, inside muscle tissue at 403 MHz for (*a*) magnetic dipole and (*b*) electric dipole (*c*) Ratio of values shown in (*a*) to (*b*)
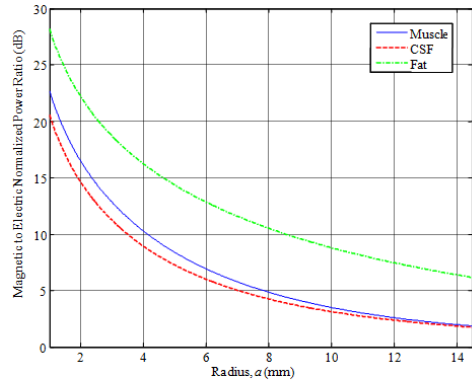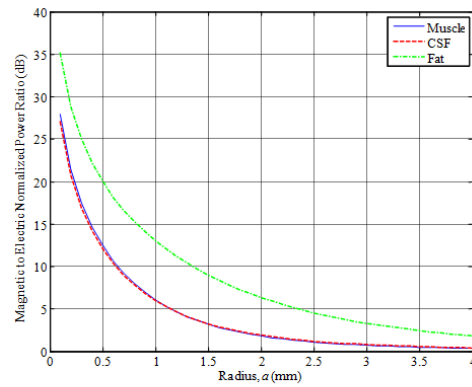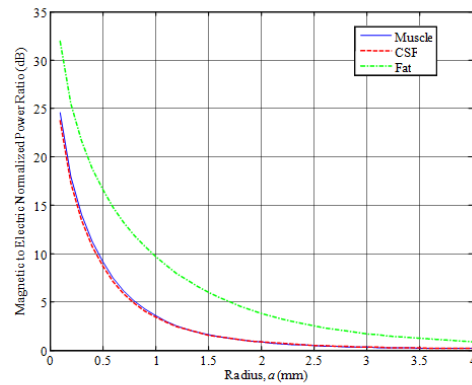
FIGURE 2.8: Normalized radiated power for various tissues vs. sphere radius, a, for fixed radiation distance, r (= 10 cm), at (*a*) 403 MHz (*b*) 2.4 GHz and (*c*) 3.5 GHz

Fig. 2.7-c demonstrates this ratio at 403 MHz for implanted antennas inside a medium mimicking muscle tissue. As it can be seen here, the ratio converges to a steady value for an antenna size larger than two radian spheres. Fig. 2.8 shows this ratio for a fixed r (= 10 cm) and varying a. This ratio has been plotted versus antenna size for three different frequencies (403 MHz, 2.4 GHz and 3.5 GHz) when the antenna is located in typical muscle tissue, fat tissue and Cerebrospinal Fluid (CSF) (see Table. 2.1) in Fig. 2.8.

The ratio of the normalized radiated power from a magnetic antenna to an electric antenna in the far-zone simplifies to

$$\lim_{r \to \infty} \left(\frac{P_M^{(N)}(r, a)}{P_E^{(N)}(r, a)} \right) = 1 + \frac{2\alpha \left(1 + 2\alpha a \right)}{\left(\alpha^2 + \beta^2 \right) a^2 \left(2\alpha + \left(\alpha^2 + \beta^2 \right) a \right)} \tag{2.35}$$

This shows that the radiated power from an ideal magnetic dipole is always more than the radiated power from an ideal electric dipole with the same size for the same accepted power in a medium with ohmic loss. This equation also shows that when the antenna size become smaller, the magnetic antenna radiates much more effectively ($1/a^2$ times higher radiated power) than the electric dipole. Plotting either 2.34 for $r \gg a$, or plotting 2.35 results in the same curves.

2.3.3 Simulation in FEKO
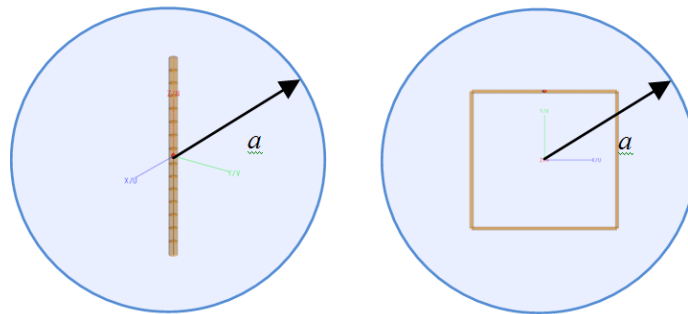
FIGURE 2.9: Simulation setup in FEKO showing dipole and loop antennas inside muscle tissues

In order to validate the theoretical results using full-wave simulations, a dipole antenna (electric field antenna) with a length of 0.5 mm and a rectangular loop antenna (magnetic field antenna) with the length of its diagonal as 0.5 mm were simulated using FEKO as shown in Fig. 2.9. These sizes are chosen in order to ensure an electrically small antenna. These antennas are surrounded by a homogeneous medium that has properties of a lossy dielectric mimicking human muscle tissue at 403 MHz (see Table. 2.1 for tissue properties). Here, a is the radius of the sphere enclosing the antenna as discussed previously and this sphere can be assumed to be the antenna size. To remove the effects of any structural or mismatch loss from these computations, the total radiated power passing through an imaginary sphere of radius a is considered to be the total input power to the antenna (similar to the input power computation for the theoretical formulation) while keeping the size of the physical antennas the same (so as to ensure that the electrically small antenna criterion is met as well as to prevent excitation of higher order modes in a larger antenna). The sphere radius a was varied from 1 mm to 14 mm in order to bring about a comparison with the theoretical results. The total radiated power at various distances from $r = a$ to a maximum distance of $r = 100$ mm is computed for both antennas and it is normalized to the input power (power at $r = a$). Then the ratio of the normalized radiated power for both antennas is computed for different radii of the imaginary sphere (which is considered to represent the antenna size).

Since FEKO contains a Method of Moments (MoM) solver, solving for the fields for a antenna surrounded by a lossy material is as easy as changing the free-space values of ϵ and μ[10]. A similar approach in HFSS was tried by a colleague using the Volume Integration of Power through the Fields Calculator function. However, this method yielded poor results possibly due to the fact that the lossiness of the surrounding medium loaded the antenna under test (AUT) adversely.

The flowchart of activities performed to extract the information from FEKO and post-processing in MATLAB is shown in Fig. 2.10. A spherical near-field pattern was simulated for all the simulations. The resolution and limits of the data are manipulated prior to displaying the plots in

---

[10]The author would like to thank Dr. Davis for his help in setting up the simulation in FEKO

order to facilitate a quick comparison with theoretical results. MATLAB codes are presented in Appendix B for reference.

2.3.3.1 Simulation Results
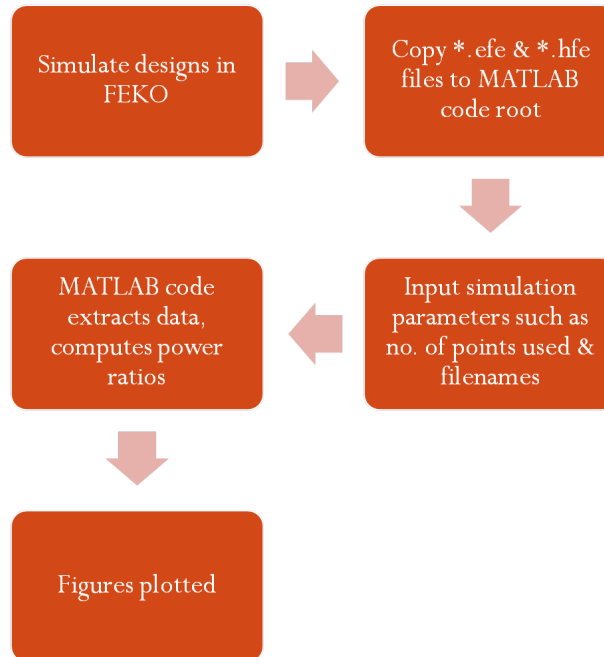
FIGURE 2.10: Flowchart describing steps to obtain MATLAB output from FEKO

Clearly, from Fig. 2.11, simulation results for normalized power agree well with the theoretical predictions in trend if not their absolute values. This can be compared to Fig. 2.8 in the case of muscle tissue for validation. In Fig. 2.12, a comparative plot shows a side-by-side comparison between theory and simulation results. It can be seen that, as the antenna size becomes smaller, the difference between the two types of antennas becomes more significant which is in agreement with our theoretical results. However, a deviation from the theoretical results can also be noticed for smaller values of a. This is due to the fact that within close proximity to the loop antenna, it does not behave as a perfect magnetic dipole (see Fig. 2.13). Instead, we see a large contribution due to the voltage source that excites the structure. Due to the electrically small nature of the antenna, current distribution is nearly uniform; however the effect of the voltage

source can be seen in the Poynting vector magnitude. Thus, since the simulation results are not generated for the exact same antennas as the theoretical effort, the results follow slightly different behavior.

A simulation with ideal dipoles in FEKO showing good agreement to theoretical results for most values of a, is shown in Fig. 2.14 and Fig. 2.15. For the case of these ideal dipoles, power scaling was applied such that the input power is 1 W to both sources. This is to correct for any input impedance mismatch due to the loading effects of the lossy material on either dipole. There is some deviation from agreement for the middle of the range possibly due to the power scaling that was applied. The symmetry in the case of these ideal dipoles is exploited by simulating only one of the 8 octants for the near-field and replicating the fields for the rest of space. In the case of the physical dipoles simulated above, this is not feasible due to the variation in fields as we get close to the source near the feed.

Fig. 2.16 shows the magnitude of the Poynting vector for both dipoles.

2.3.4   Study Conclusions

It can be seen that there is a fundamental difference in the near-field ohmic loss generated within a lossy medium surrounding electric and magnetic antennas. For electrically small antennas, this loss is more pronounced. Theoretical results were presented and later validated through simulation in a full wave simulator using small dipole and loop antennas. It is noted that the approach used here is a perturbational method and the results presented are an approximation of the expected performance. In conclusion, it is clear that magnetic antennas such as the loop antenna and/or its variants offer a significant advantage when compared to electric field antennas such as the dipole, Planar Inverted F-antenna (PIFA), patch and others in terms of power lost in dielectric media surrounding the antenna. Thus, for implanted applications where we have stringent regulations on SAR and where maximum efficiency is required (such as wireless power transfer to medical devices), it makes more sense to use efficient magnetic antennas. Even for magnetic antennas, one must choose a design that minimizes structural losses. The Electrically Coupled Loop Antenna (ECLA) (introduced in the following chapter)
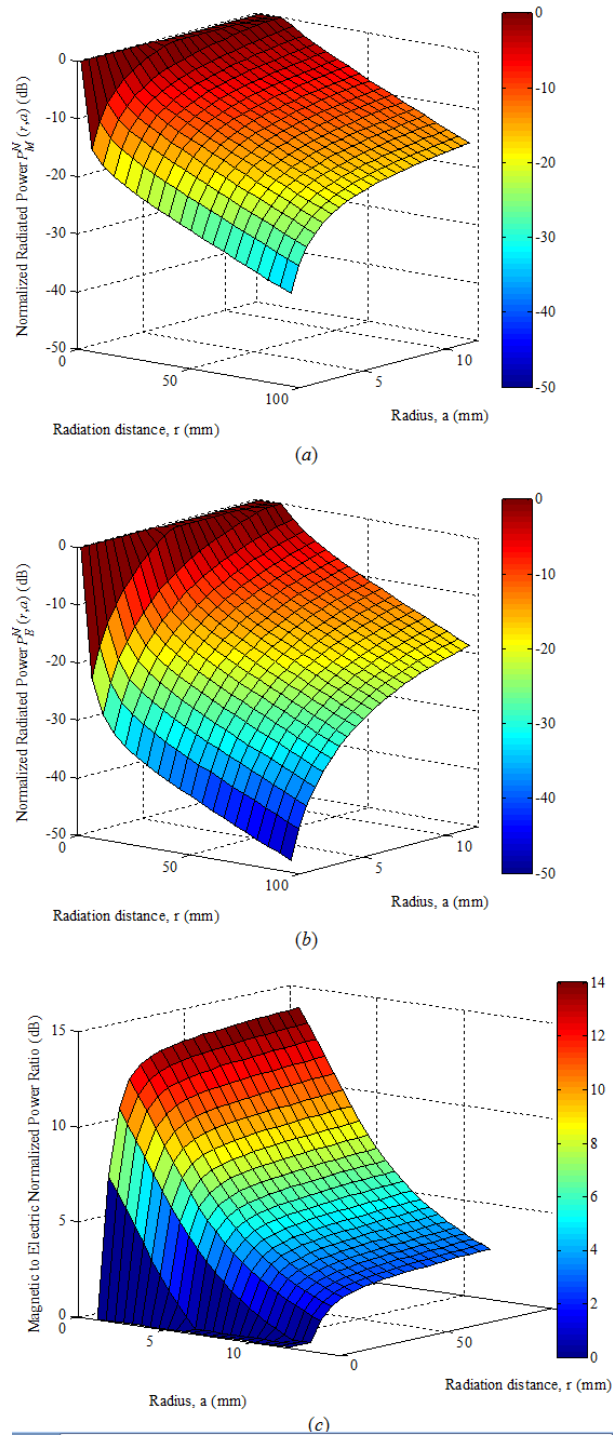
FIGURE 2.11: Simulated results for normalized radiated power ratio, $P^{(N)}(r, a)$, inside muscle tissue at 403 MHz for (*a*) loop antenna and (*b*) electric dipole. (*c*) Ratio of values shown in (*a*) to (*b*)
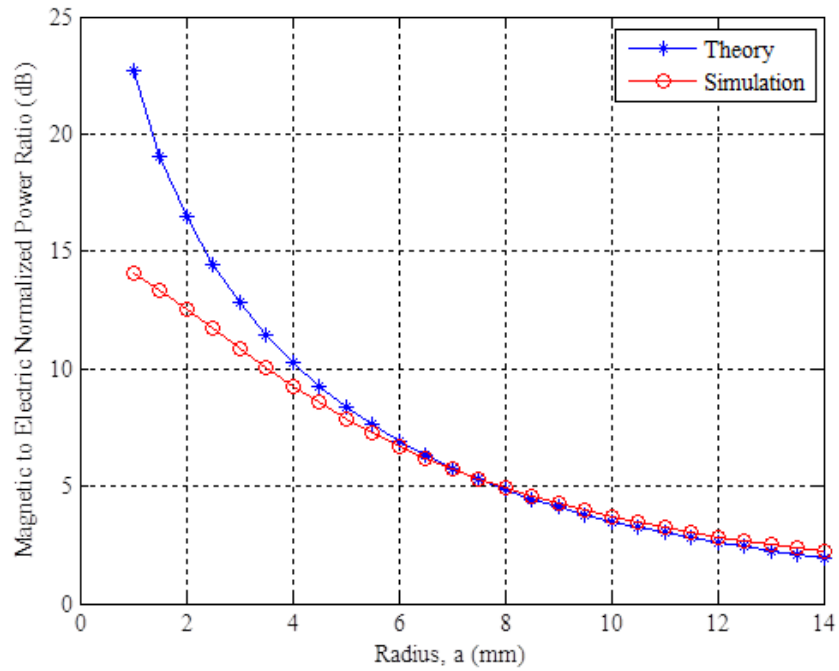
FIGURE 2.12: Comparison between theoretical and simulated results for normalized radiated power ratio, $P^{(N)}(r, a)$, inside muscle tissue at 403 MHz at r = 10 cm
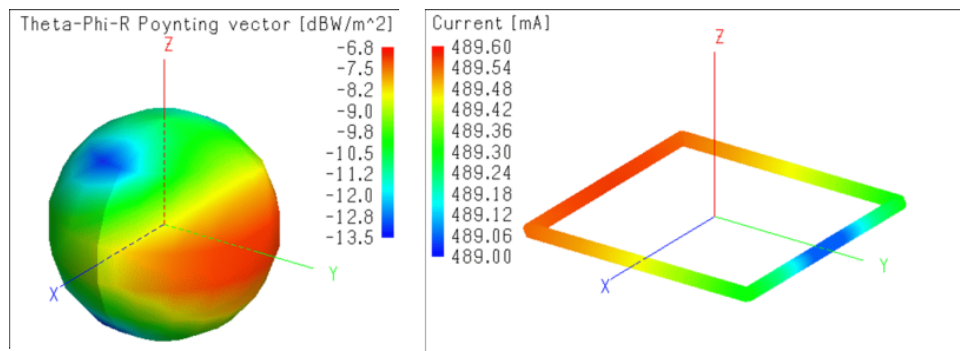
FIGURE 2.13: Total Poynting vector magnitude (in dB W/m^2) and Current Distribution on the electrically small loop antenna

(a)

(b)

(c)
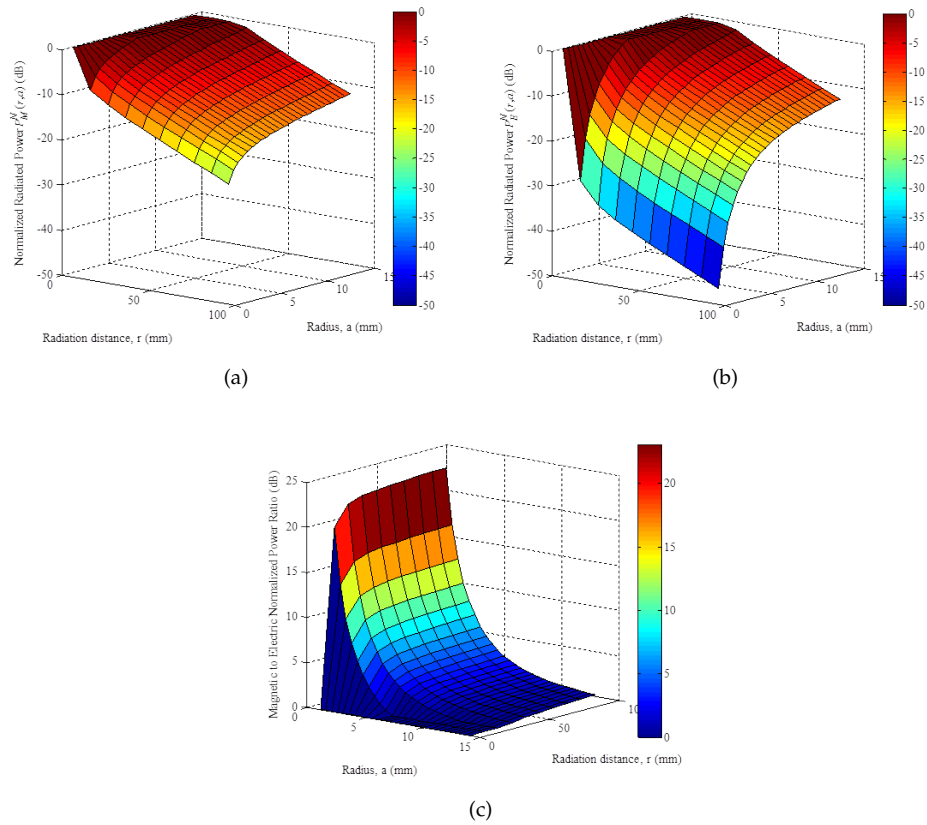
FIGURE 2.14: Simulated results for normalized radiated power ratio, $P^{(N)}(r, a)$, inside muscle tissue at 403 MHz for (*a*) ideal magnetic and (*b*) ideal electric dipoles. (*c*) Ratio of values shown in (*a*) to (*b*)

is a good candidate then by virtue of its high-Q resonator nature that can be conveniently engineered to suit different applications.
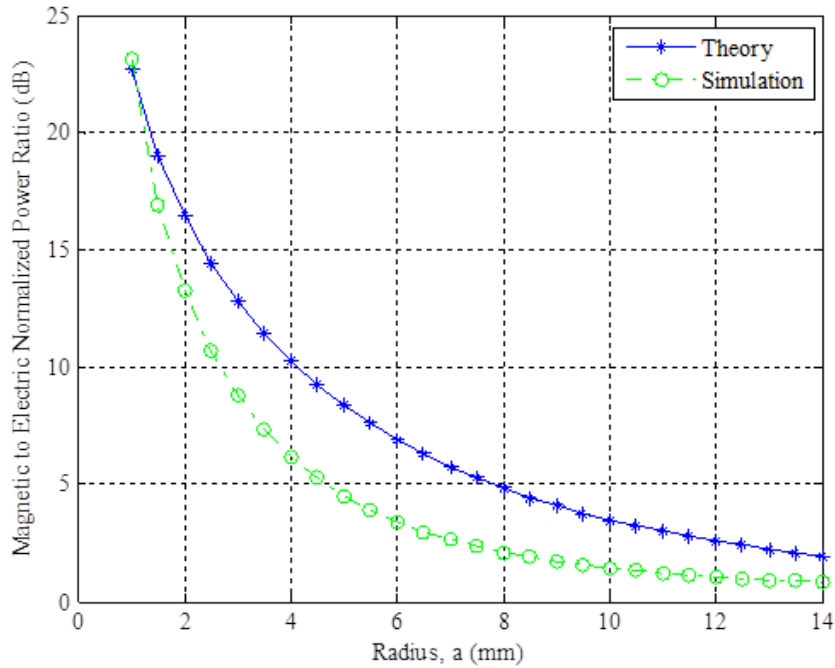
FIGURE 2.15: Comparison between theoretical and simulated results for normalized radiated power ratio, $P^{(N)}(r, a)$, inside muscle tissue at 403 MHz at $r = 10$ cm for ideal electric and magnetic dipoles

(a) Ideal Magnetic Dipole   (b) Ideal Electric Dipole
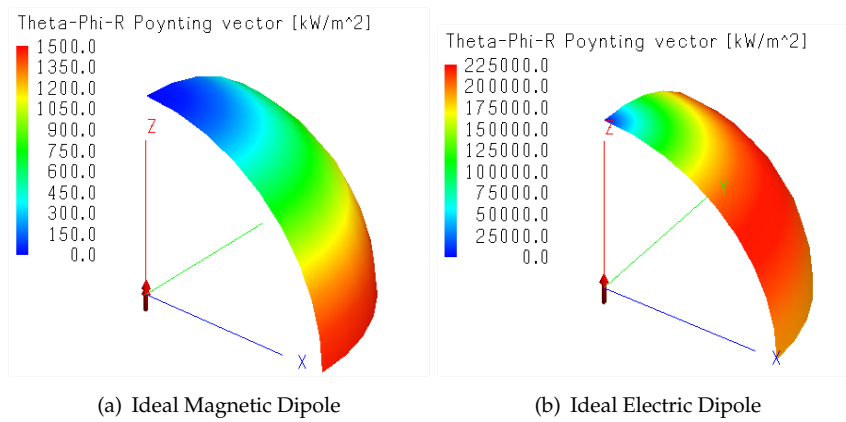
FIGURE 2.16: Magnitude of Poynting Vector for Ideal Dipoles

Chapter 3

Antenna Design

3.1 Introduction

The previous chapter established the different perspectives on design methodology that are prevalent today in academia and the industry. It was seen that a vast majority of designs approach the problem of Wireless Power Transfer (WPT) from the perspective of coupled coils. While this is a perfectly reasonable way of analysis, some more insight into the problem may be gleaned by exploring the design of a WPT system by using antenna theory. In this chapter, we will focus on the use of antennas, namely their near-field, miniaturization for use in implanted applications and the challenges associated with doing so.

It is clear that we require an antenna that can provide a close resemblance to the magnetic dipole in the sense that we require strong magnetic coupling in the near-field. However, we also require a high-Q antenna to be able to store this energy effectively around the antenna and not let it radiate away. From the previous chapter's discussion, we see that a high-Q antenna will also help improve Power Transfer Efficiency (PTE) in a loosely coupled system. Thus, an Electrically Coupled Loop Antenna (ECLA) is proposed [Manteghi, 2013b, Nambiar and Manteghi, 2014a] in this chapter that acts as a high-Q resonator and can be used as a coupling element for WPT systems. After studying the ECLA in some detail, an equivalent circuit is

presented followed by some simulation and measurement results for various use cases. As discussed previously, the focus will be to realize two systems that fulfill two use cases, namely a low frequency version that is suitable for commercial applications (target frequency of 13.56 MHz in the ISM band) in free space and a miniaturized version for implanted applications (target frequency of 403 MHz in the MICS band).

3.2 Electrically Coupled Loop Antenna

The Electrically Coupled Loop Antenna (ECLA) was proposed in Manteghi [2013a] as a dual for the Planar Inverted F-Antenna (PIFA) [Taga and Tsunekawa, 1987]. The PIFA, being an electric antenna and characterized as a patch antenna with a shorting pin to reduce its size and make the patch resonant, is a magnetic current antenna [Villamil and Manteghi, 2013]. There are specific use cases where the qualities of the PIFA are better suited for a certain application (such as cellphones which require small sized antennas and wide bandwidths). However, the case for using the ECLA as a WPT candidate will be made in this thesis. The structure of a simple ECLA is shown in Fig. 3.1. It is basically a loop antenna that is coupled to the transmission line through a capacitive feed. The distributed nature of the inductance and the capacitance are responsible for the very high Q. It is also a self-matched antenna, where the dimensions of the antenna's capacitive "feed head" can be modified to control the input impedance of the antenna and match it to a larger variation in transmission line impedance by choosing a suitable feed head dimension and/or height (t_p, t_s). This capability for absorption of the impedance into a high-Q resonator *without* the use of lumped components helps in lowering the loss incurred in the matching circuits required in other types of loops used for WPT. Also, the fact that the ECLA is an electrically small antenna reduces its radiation efficiency and makes it less susceptible to incur radiation losses; something that we would like to keep at a minimum in non-radiative WPT (see Fig. 3.2). By virtue of its smaller physical size to achieve self-resonance, the ECLA's form factor is much smaller compared to some other loops. Additional coils to increase Q are not required either to increase the Q of the system [Kiani and Ghovanloo, 2013, Kiani et al., 2011] nor to achieve better matching [Karalis et al., 2008] (controlled entirely by

(a) Front View

(b) Isometric View
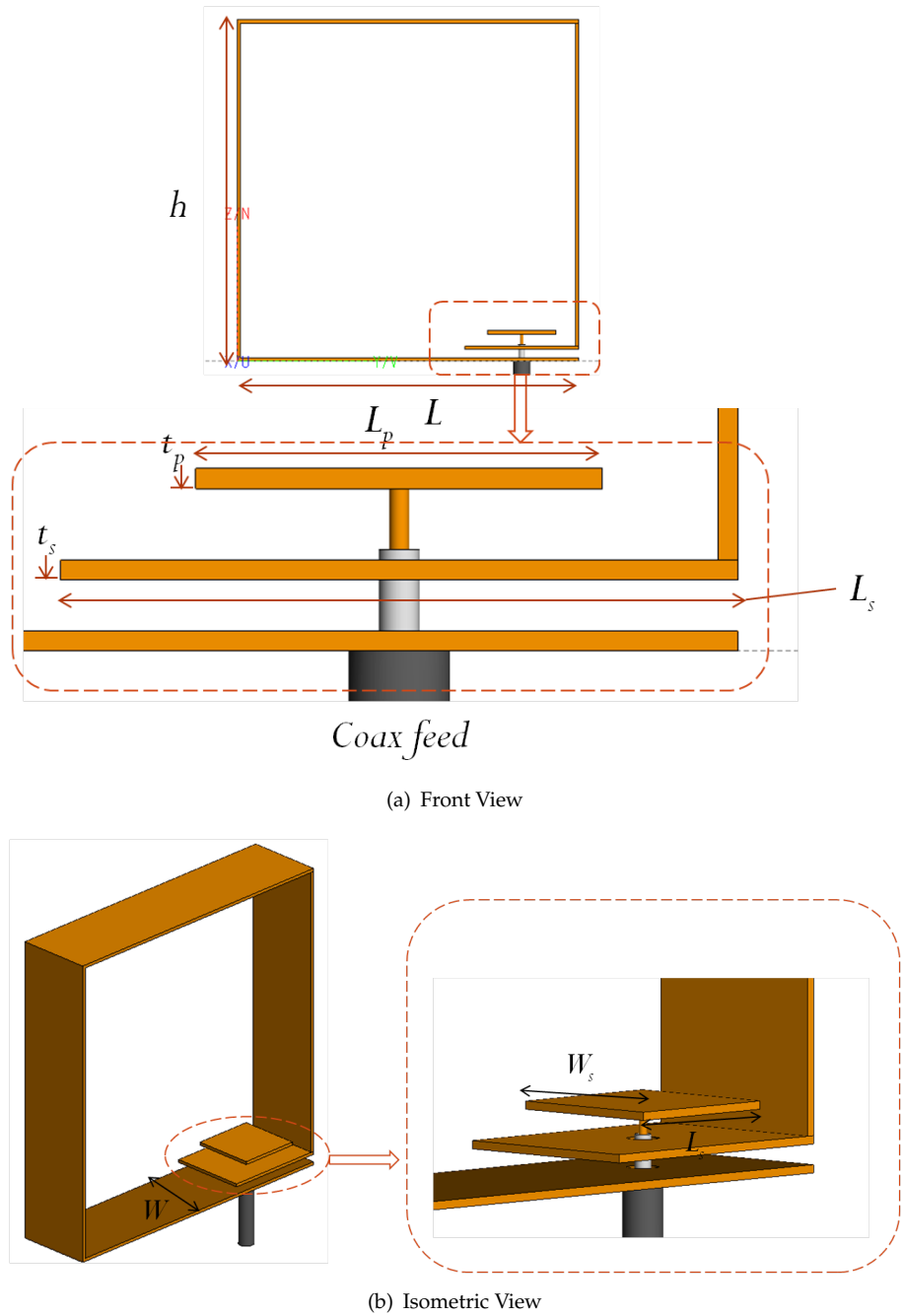
FIGURE 3.1: ECLA structure and design parameters

the ECLA's feed head dimensions as shown in Table. 3.1). Moreover, due to the ECLA being a magnetic field antenna in the near field, it is well suited for implanted applications (as shown in 2.3).

TABLE 3.1: Control of Frequency Response using ECLA's Design Parameters

Design variable	Affected parameter
L, h	Coarse control of resonant frequency
L_s, t_s, W_s, W	Finer control of resonant frequency
L_p, t_p	Controls the Input Impedance

From Fig. 3.1, it can be seen that the resonance of the antenna can be controlled by tuning the parameters shown in Table. 3.1. A design exploiting the frequency dependence of the distributed capacitors for the purpose of miniaturization of the antenna will be discussed in subsequent sections.

3.2.1 Antenna Characteristics

The ECLA has the characteristic "donut"-shaped far-field radiation pattern of a magnetic dipole oriented along the X-axis as seen in Fig. 3.2. Also note that the far-field gain has a maximum of -11.2 dBi at 13.95 MHz (Return Loss of 12 dB). A comparison of the near field distribution of the total electric and magnetic field intensities is shown in Fig. 3.3 as well. Note that the values are shown in dB scale to bring out the variation with r more clearly. At the resonant frequency, the wavelength, $\lambda = 21.5$ m and $ka = \lambda/2\pi = 3.4$ m. Clearly, it can be seen that the ECLA is a magnetic antenna with a relatively strong magnetic field in its near zone. Another method for measuring antenna efficiency is the Wheeler cap method introduced in Wheeler [1959][1].

---

[1]http://www.rfcafe.com/references/articles/Efficiency-Measurement-Antenna-Wheeler-Cap.htm
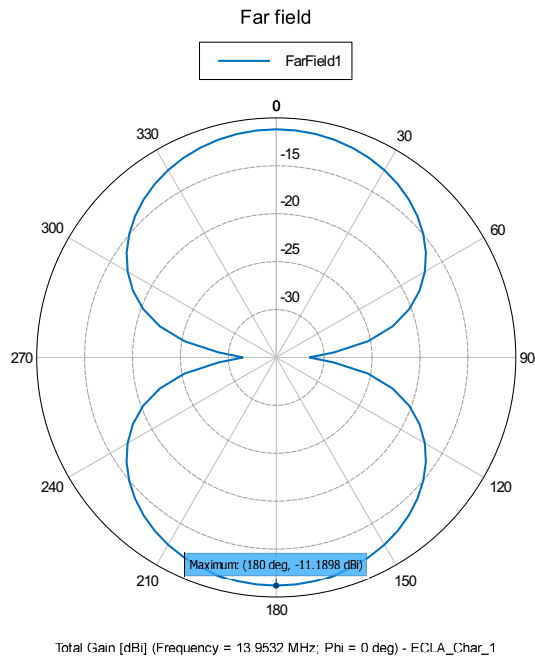
(a) Theta Cut
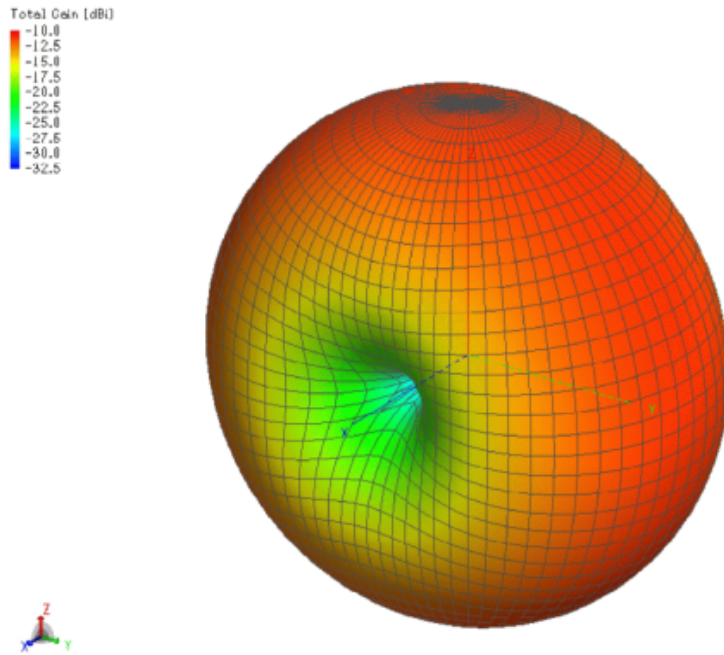
(b) 3D Pattern - Isometric view

FIGURE 3.2: ECLA Gain in dBi
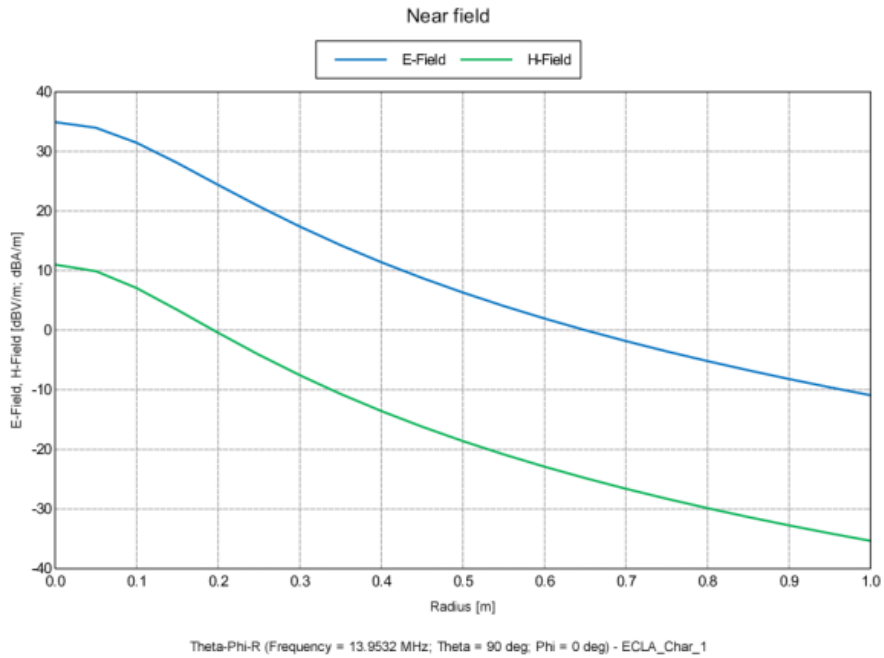
FIGURE 3.3: $|\mathbf{E_{tot}}|, |\mathbf{H_{tot}}|$ variation with r at $\theta = \pi/2, \phi = 0$

3.3 Development of an Equivalent Circuit

In order to understand the working of the coupled systems for WPT as well as to facilitate faster design iterations, an equivalent circuit was developed in Keysight ADS. The first such attempt is shown in Fig. 3.4 (a). This circuit was based on the rather simple breakdown of what to expect given the structure of the ECLA, viz. a lossy parallel inductor capacitor network (distributed transmission line) coupled through a capacitor (feed head). However, this model had some inherent issues in the fact that the true response of the device could not be fully captured. It is important to understand here that the objective of developing this circuit was to provide a quick circuit model for the antenna to observe coupling as well as to understand the large-signal (non-linear) aspects of using the antenna as a load for an oscillator (to be discussed in Chapter 4). Thus, the goal here is to capture the frequency response of the antenna at least in the limited sense of the measured S-parameters in a (relatively) narrow bandwidth.
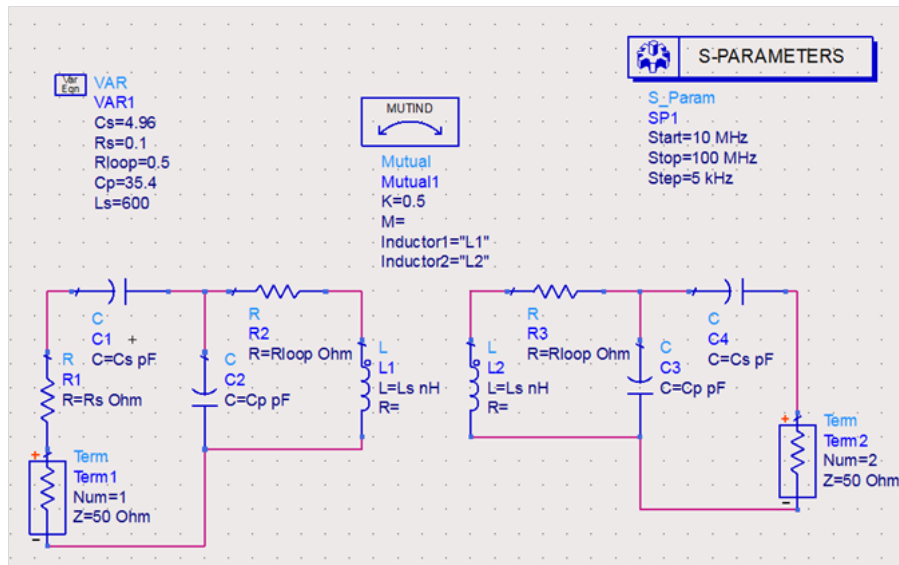
(a) Initial Model
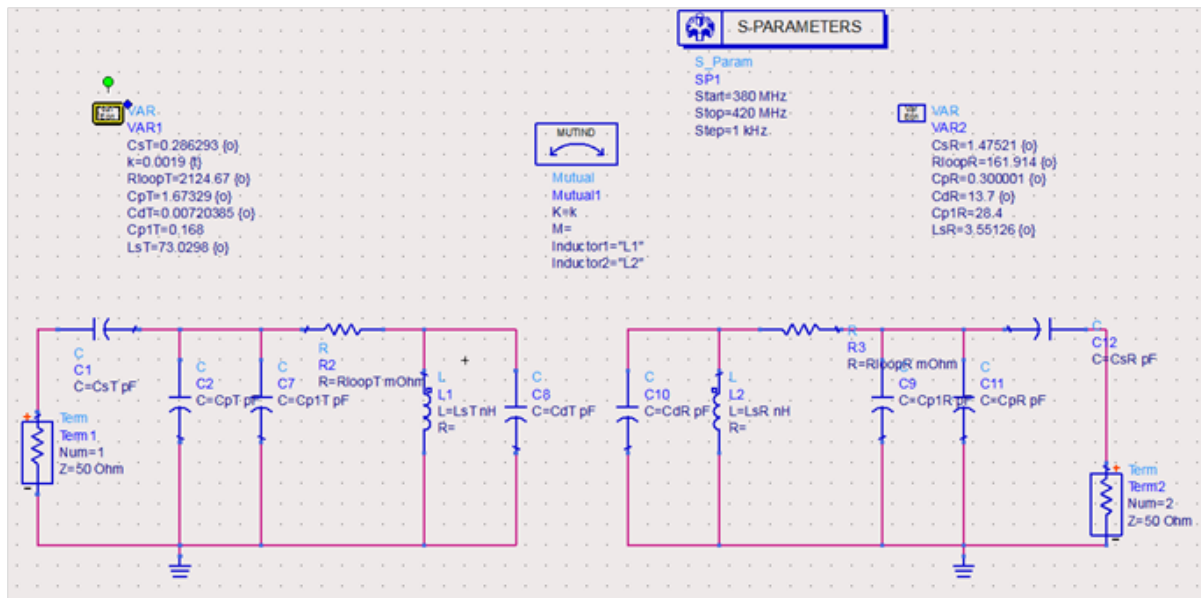
(b) Final Model

FIGURE 3.4: ECLA equivalent circuit model iterations
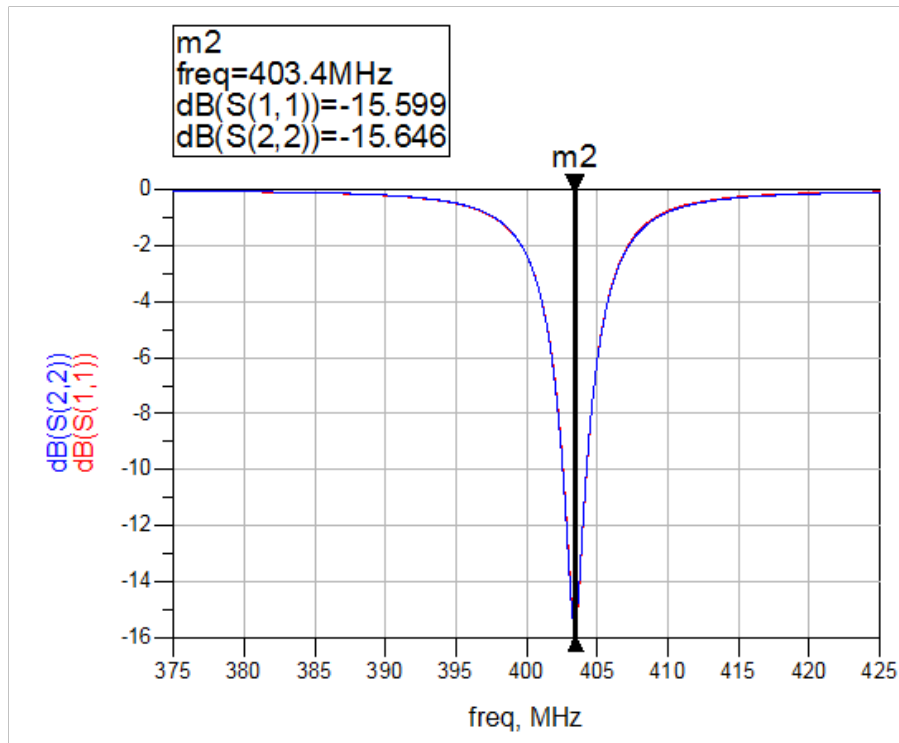
(a) Magnitude Response
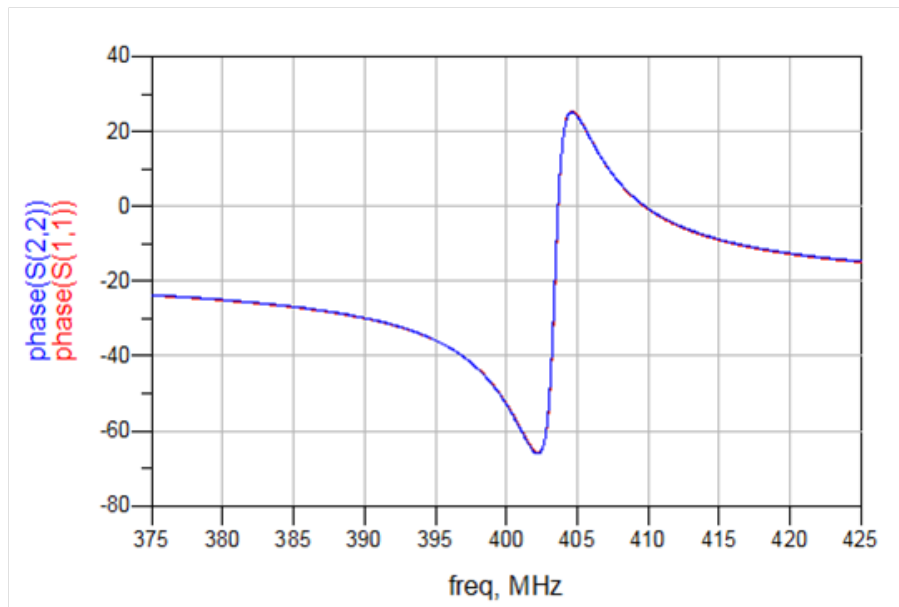
(b) Phase Response

FIGURE 3.5: Gain and phase matched with an ECLA equivalent circuit model

Fig. 3.4 (b) was the result of combining a test bench setup in ADS where either the full-wave or measured S-parameters of the AUT would be subject to an optimization process after initial tuning (or "seeding"). For example, an approximate value for the feeding capacitors and loop resistance can be calculated (on the first order, without accounting for fringing effects) using standard parallel plate capacitor equations and skin depth calculations respectively. Also note that a parallel capacitor was added across the inductor to achieve the required match. The optimization flowchart and setup is explained in Appendix B.

Fig. 3.5 shows the result of the optimization process when applied to an ECLA for the MICS band at 403 MHz. This technique will be used in the rest of the thesis for multiple applications.

3.4 ECLA Variants and Design Iterations

This section will discuss the design and simulation of some ECLA designs. Due to the ease of its construction, a square ECLA formed from thin Copper sheet metal (of approximate thickness 0.5 mm) was used for most initial designs. However, to obtain better current distribution throughout the antenna, a circular ECLA was also prototyped using hollow brass or copper tubing (discussed in the next section).

It should be noted that both the bottom capacitor and feed head dimensions need to be modified while manipulating the frequency as a particular feed head dimension that ensures a good match at one frequency does not guarantee a match another frequency, say 5 MHz away. Some hybrid design techniques using a combination of full-wave data and circuit-level simulation is used to achieve faster design turnaround times.

We will also discuss the practical aspects of prototyping and measuring some ECLA designs[2]. The following sections elaborate efforts to design and demonstrate WPT with ECLAs for different frequency bands and applications.

3.4.1 ECLA in Free Space

(a) Regular ECLA
(b) Modified ECLA
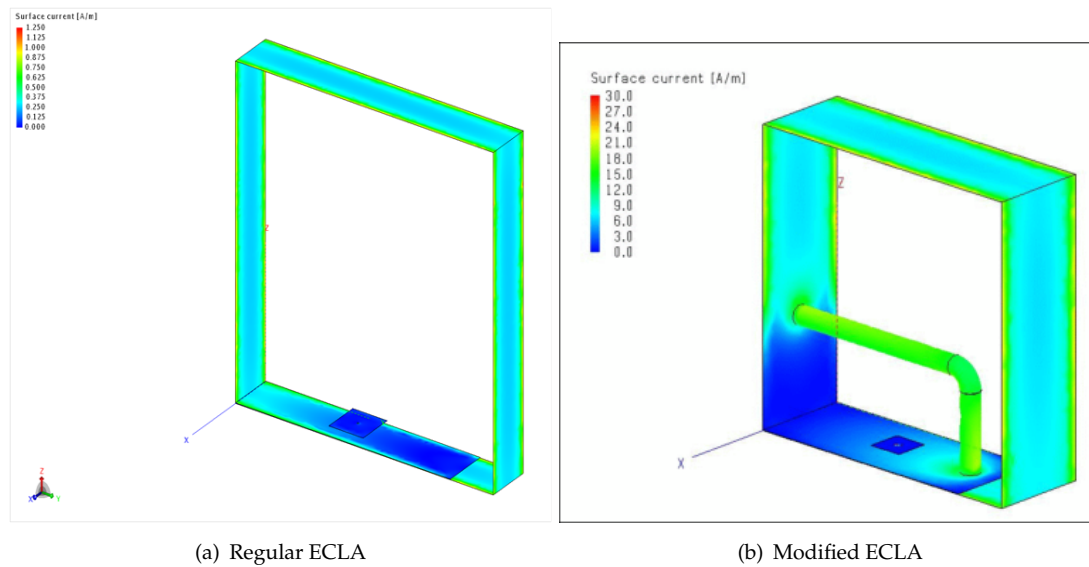
FIGURE 3.6: ECLA structural iterations and Current Density

As seen from Table. 3.1, the design variables of the ECLA can be modified to make it resonant at any frequency. For the free space case, we require the ECLA to be designed close the ISM band at 13.65 MHz and hence designs were simulated in FEKO for $L, W = 30, 5$ cm. Fig. 3.6 shows the current distribution for a regular square ECLA (notice high edge currents) as well as a modified version. The latter was modified for obtaining a smaller E/H (impedance) ratio in the immediate near field[3] but was not pursued further due to difficulties in fabricating and matching such a design. The return loss for such a design was poor, averaging less than 7 dB with given size constraints.

In order to save material costs, scaled versions of the original square ECLA were created with a length reduction factor of 3 ($L, W = 10, 1.5$ cm) and is shown in Fig. 3.7. The resonant frequency was found to be around 42MHz for both loops and the S_{11} achieved was close to 30 dB indicating good matching. An S_{21} of 10 dB for a separation of 10 cm ($d = L$) was obtained as well. Connections are via 3.5 mm SMA connectors and a ground plane made of a brass sheet

---

[3]For some reason, FEKO's and HFSS' results never agreed with each other in terms of absolute values of the fields.

(a) Square ECLA prototype
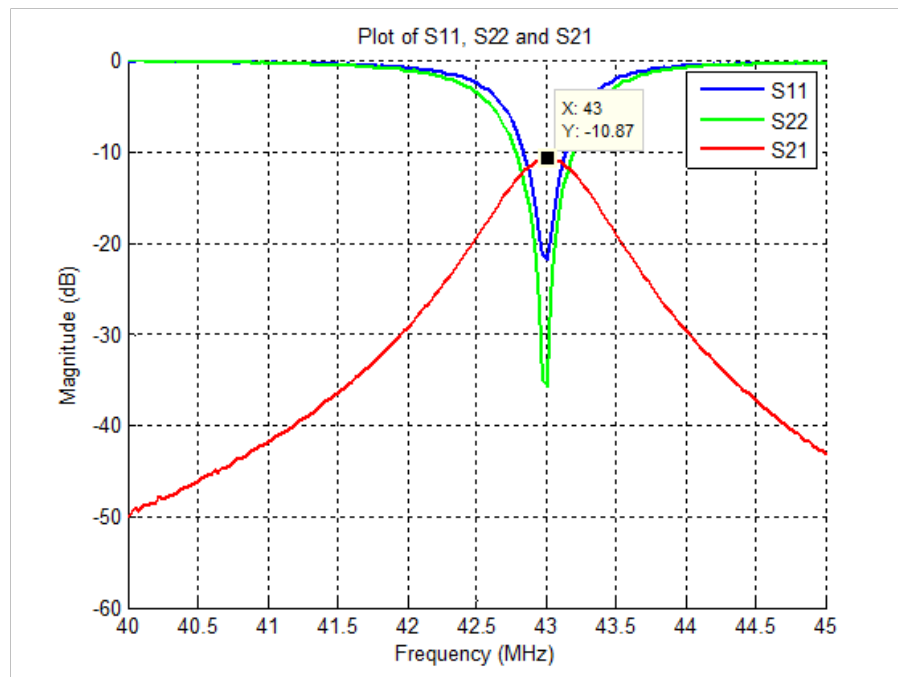
(b) Measured S-parameters

FIGURE 3.7: ECLA protoype and measurement results

(a) |**J**| on structure

(b) |**E**|-field

(c) |**H**|-field
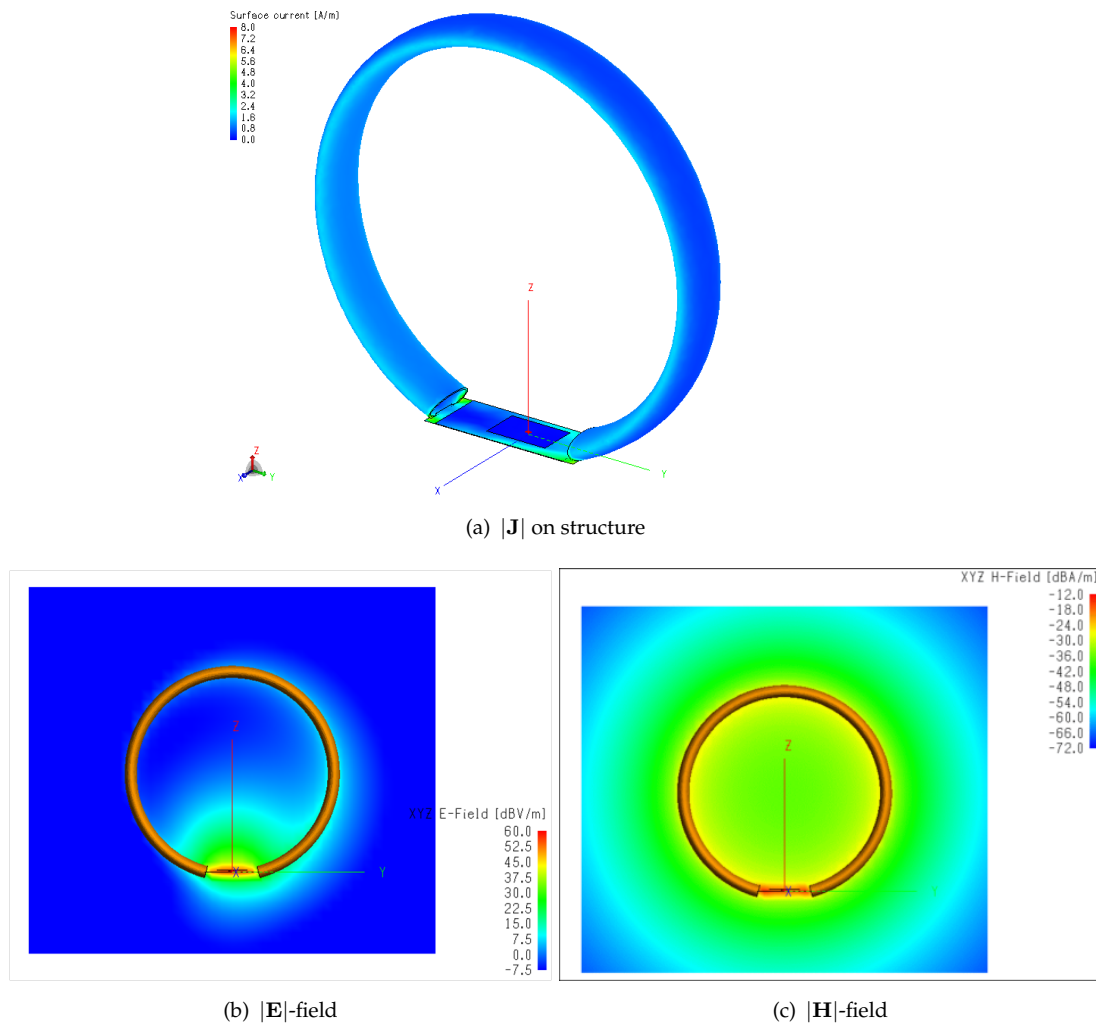
FIGURE 3.8: Ring ECLA simulation in FEKO for near-field

$(2' \times 4')$ is used for avoiding any coupling via the VNA cables. Measurements were taken after obtaining best matching by adjusting the feed head.

To reduce the Ohmic losses incurred as an effect of the thin metal strip and sharp bends in the square ECLA, a ring ECLA was designed in FEKO with a radius of 50 mm (see Fig. 3.8). The resonant frequency was found to be close to 60 MHz and hence a 70 mm radius ring was designed and prototyped to bring the frequency down further. PTFE Tape is used to increase the distributed capacitance as well as for insulation. The experimental setup is shown in Fig. 3.9. A layer of PTFE tape was also used between the capacitive plates to bring down the
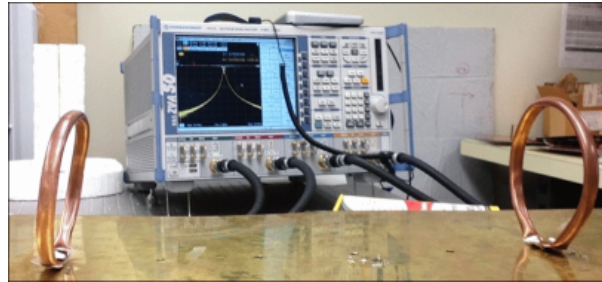
(a) Experimental Setup
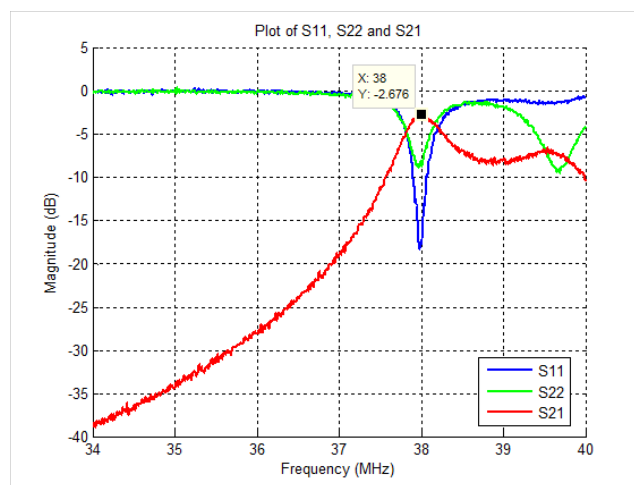
(b) d=20 cm
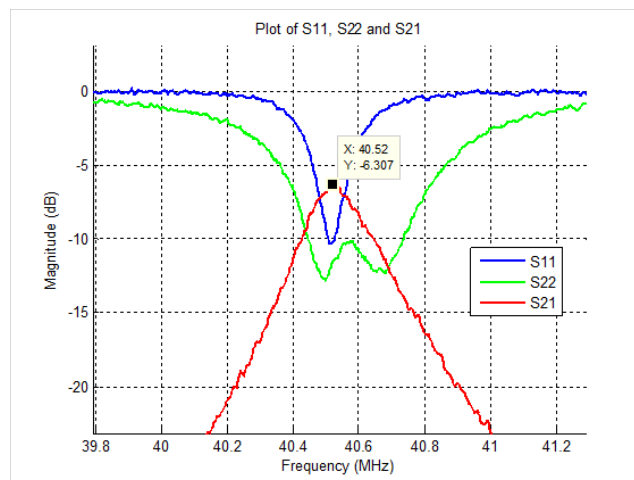
(c) d=50 cm

FIGURE 3.9: Ring ECLA experimental setup

frequency further. The distance between the loops can be varied from 0.1 m to 1 m by moving the loops on pre-drilled holes spaced 10 cm apart on the brass ground plane. S_{21} of -2.7 dB and -6.3 dB (PTE=53.7% and 23.4% respectively) were obtained at 0.2 and 0.5 m separation[4] ($d = 1.4, 3.6L$). At this range, these results can be bettered by fabricating the antennas better and by providing a better load to the receiver (Experiments were performed on a 50 ohm VNA system which may not be the ideal load required to maximize both PTE and/or Power Delivered to Load (PDL) as seen from Section 2.1.2).

Also, to reduce the frequency further while maintaining the same size, higher capacitance at the bottom plates is needed. This can be accomplished by proper manufacturing techniques where the metal surface is coated with epoxy coatings, lacquer finish, Poly-Urethane (PU), etc. (available commercially as sprays, paints) or any other well-characterized thin film coating and mechanically clamped (but electrically insulated)[5]. One of the major achievements of this exercise is to demonstrate the capability of the ECLA in a WPT system while maintaining a small form factor. For example, the WiTricity system demonstrated by Kurs et al. uses large coils (2 feet diameter) to achieve a 45% PTE at 10 MHz. Also, at the least, three coils are needed (two at transmit and one at receive side). By comparison, an ECLA at this frequency would be less than a foot in diameter (possibly lesser if tighter fabrication is performed) and would require only two antennas.

3.4.2 ECLA in Implanted Applications

TABLE 3.2: Coupling efficiency vs. receiver antenna size

Case	Rx ECLA ($L \times h \times W \, \text{mm}^3$)	$|S_{21}|$ (dB)	k
I	$3 \times 3 \times 3$	-27.1	0.0008
II	$5 \times 5 \times 3$	-21.7	0.0019
III	$7 \times 7 \times 3$	-18.7	0.0026

[4]These results were presented at the IEEE AP-S/URSI 2013 Conference in Orlando, FL, USA.
[5]http://en.wikipedia.org/wiki/Conformal_coating

(a) HFSS Setup; $d = 10$ cm

(b) Tuning capacitor values in ADS
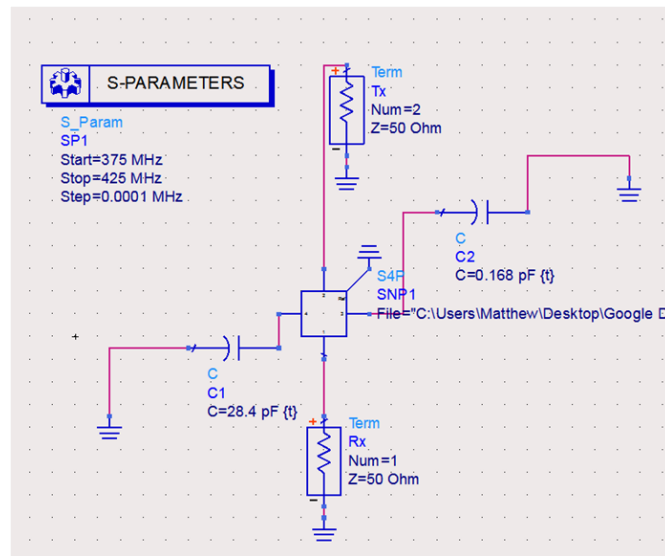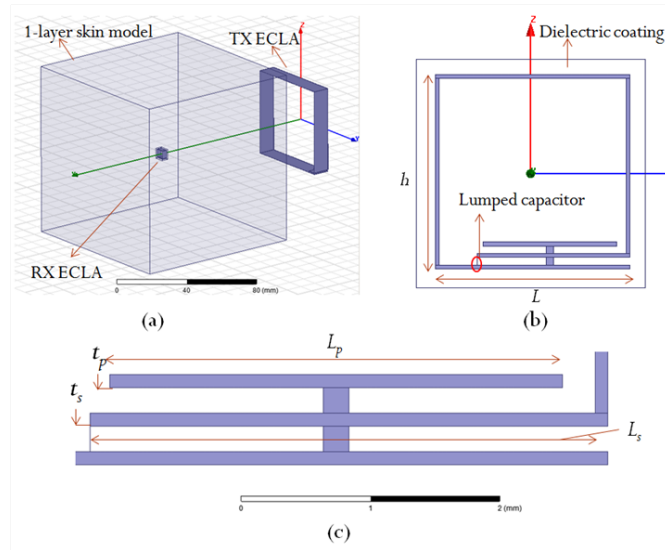
FIGURE 3.10: Initial HFSS and ADS setup for implanted applications
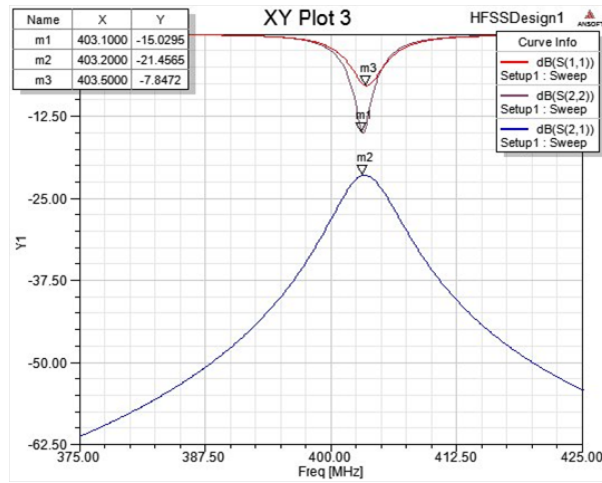
(a) HFSS S-parameters after tuning
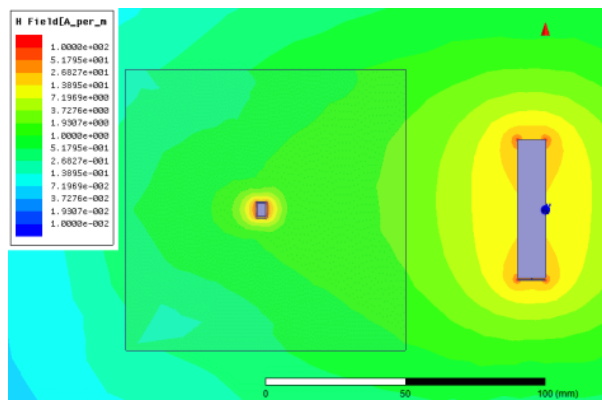
(b) **H**-field in HFSS
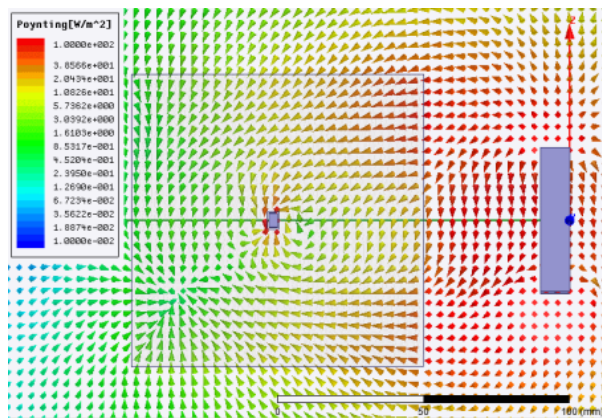
(c) Real part of the Poynting vector($\Re\{\mathbf{E} \times \mathbf{H}\}$)

FIGURE 3.11: HFSS Results

One of the main issues with any implanted device is providing power to it. Those devices which spend a short time in the human body can be easily fed by batteries. However, the long-lived devices always need to be recharged or fed through a reliable energy harvesting mechanism. This can be quite cumbersome especially when the implants are within the body or trans/sub-cutaneous[6]. Existing techniques mostly use inductive loops that require one or more conditioning (or repeater) stages coupled with matching networks at source and load ends which tend to load them and reduce overall system efficiency due to losses incurred in matching networks and parasitic coils [Guoxing et al., 2005, Kumar et al., 2009, Neihart and Harrison, 2005, Ping et al., 2008, RamRakhyani et al., 2011, Si et al., 2007, Xiaoyu et al., 2009]. The ECLA, on the other hand, uses a capacitive feed which can be designed in order to do away with any sort of matching network i.e. it can be directly fed and perfectly matched to a transmission line or directly to a source/load.

The transfer of power to a device inside the human body is a complicated problem and arriving at a reasonable model for such a link is a bit involved [Fotopoulou and Flynn, 2006, Guoxing et al., 2005]. This is mainly due to the non-homogeneous and frequency-dependent dielectric environment that the different parts of the human body offers to RF waves. Another constraint in the case of implanted devices is the small form factor that is required to facilitate their use inside the human body. We will mainly focus on the latter aspect in this section. Therefore, in order to better understand the effect of the variation in size of the receiving antenna on the PTE, we will also study the case where two ECLAs are used as transmitter and receiver. In this section, we modify the ECLA design for implanted applications by miniaturizing it considerably. This can be achieved in two ways:

- In a traditional sense, surrounding the antenna in a dielectric material with a bio-compatible insulation layer to increase the electrical length (d/λ) of the antenna.

- Since the ECLA uses distributed capacitors for feeding as well as for achieving self-resonance (see Table. 3.1), a high-Q lumped capacitor can be added in parallel to the

---

[6]http://www.embedded.com/design/connectivity/4025029/The-challenge-of-designing-in-body-communications

frequency-controlling t_p height to increase the capacitance and lower the frequency of operation to a desirable frequency.

Choice of Full-wave Solver: Note that in typical implanted applications, such as for a pacemaker or a sensor inside the body, the implanted antenna (receiver) is heavily miniaturized but the source or transmit antenna outside the body does not necessarily have to be small. Biomedical applications such as these are inherently a material half-space problem [King et al., 1981, Smith, 1984] and care must be taken in defining the near-zone as power transfer may occur due to hybrid modes at mid to high distances. For studying this half-space problem, HFSS is used over FEKO, due to the latter's difficulty in dealing with dielectric boundaries (MoM engines typically behave irregularly with dielectric interfaces; however, to be fair, FEKO does have an FEM engine and a hybrid solver that the author hasn't tried yet.).

The PTE can be considered to be the value of $|S_{21}|^2$ as it encapsulates the coupling effects between the two antennas and gives an idea of available power [Gonzalez, 1984] transferred from one port to the other[Nambiar and Manteghi, 2014b]. Full-wave EM simulations are carried out in HFSS to obtain PTE followed by a circuit-level analysis using ADS to obtain a value for coupling coefficient, k. Ascertaining k is important as it can facilitate a better design procedure for the antennas and gives a better understanding of the coupling and the overall Q of the system.

The HFSS simulation setup for 403 MHz MICS band WPT for implanted applications is shown in Fig. 3.10. After an initial run, the S-parameter file from HFSS in input to an ADS schematic where the extra capacitor ports are varied in capacitance to achieve operation at the correct frequency. These values are then fed back to the HFSS model and simulated as a final test. An associated problem that arises here is that the initial HFSS simulation contains a solution for a frequency set by the user that very well isn't resonant, at least not at the final desired frequency. However, results were not far from that expected and a small amount of tuning is usually enough to set the antennas to the desired frequency of operation. This hybrid approach of using both HFSS and ADS results in considerable savings in time and computational effort.

The setup consists of two ECLAs, one as a transmitter located in free space and another coated by a polystyrene film (for biocompatibility) of dielectric constant, ϵ_r = 2.07, and embedded within a block of dry skin with equivalent ϵ_r = 49.7 [Gabriel et al., 1996][7]. A lumped capacitor is used to miniaturize the implanted antenna. An equivalent single layer of skin tissue is chosen to keep the simulation simple. The transmitter dimensions are $50 \times 50 \times 10\text{mm}^3$ ($L \times h \times W$) and the dimensions of the implanted antenna are varied as shown in Table. 3.2 separated by $d = 100$ cm. The ADS equivalent circuits discussed in 3.3 were then matched in terms of component values to fit the full-wave simulation results such that a representative value of k may be obtained. From Chapter 2, we know that

$$PTE = k^2 Q_1 Q_2 \tag{3.1}$$

where Q_1, Q_2 are the loaded quality factors of the antennas. Thus, by modeling the link in ADS, we can get a better understanding of the design aspects of the system as well. The results for the final design for Case II of Table. 3.2 are shown in Fig. 3.11 [Nambiar and Manteghi, 2014a]. As expected, a smaller-sized implanted antenna gives a lower value of PTE. However, it is interesting to note that the coupling regime is of a very loosely-coupled system as seen by the magnitude of k (< 0.01). From this we can see that the full wave results and the ADS modeling technique can be compared for a given load impedance and to characterize the power transfer channel purely through the coupling factor, k.

Some prototyped antennas (courtesy of Dr. Manteghi) are shown in Fig. 3.12. These antennas are found to resonate at 449.5 MHz (as some capacitor values needed for MICS band operation were not readily available) and measurement results are seen in Fig. 3.13. As was the case before, a brass sheet acts as a ground plane and the Tx ECLA is modified for 450 MHz operation ($30 \times 30 \times 10\text{mm}^3$). Miniaturization of the antenna was made possible by adding a high-Q lumped capacitor to the distributed capacitor. An $|S_{21}|$ of -35 dB was obtained at a distance of 10 cm in free space which is far below our expectations. However, these results may be

---

[7]http://transition.fcc.gov/oet/rfsafety/dielectric.html
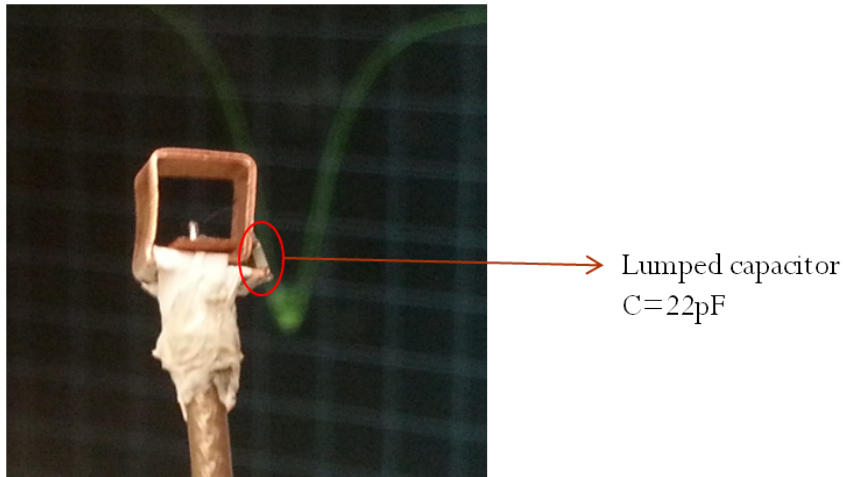
(a) $5 \times 5 \times 3mm^3$ with lumped capacitor

(b)

(c) Other prototype variations

FIGURE 3.12: Miniaturized ECLA prototypes using additional lumped capacitor where necessary

justified by the limited manufacturing capabilities available at the time and poor RL of the small antennas.

Even though the HFSS results were encouraging, they fail to give a complete picture as regards the actual performance of the system when used inside the human body. Remcom's XFDTD 7 (XF7) is a Finite Difference Time Domain (FDTD) solver that has a human body voxel model with mm-level resolution[8]. Fig. 3.14 shows the setup in XF7 and the resulting $|S_{21}|$ at $d = 40, 65$

---

[8]CST also has a human body solver but Remcom graciously allowed the use of their models for free. FEKO also supports human tissue models and SAR calculation but was not used due to lack of a human model.

(a) Experimental Setup
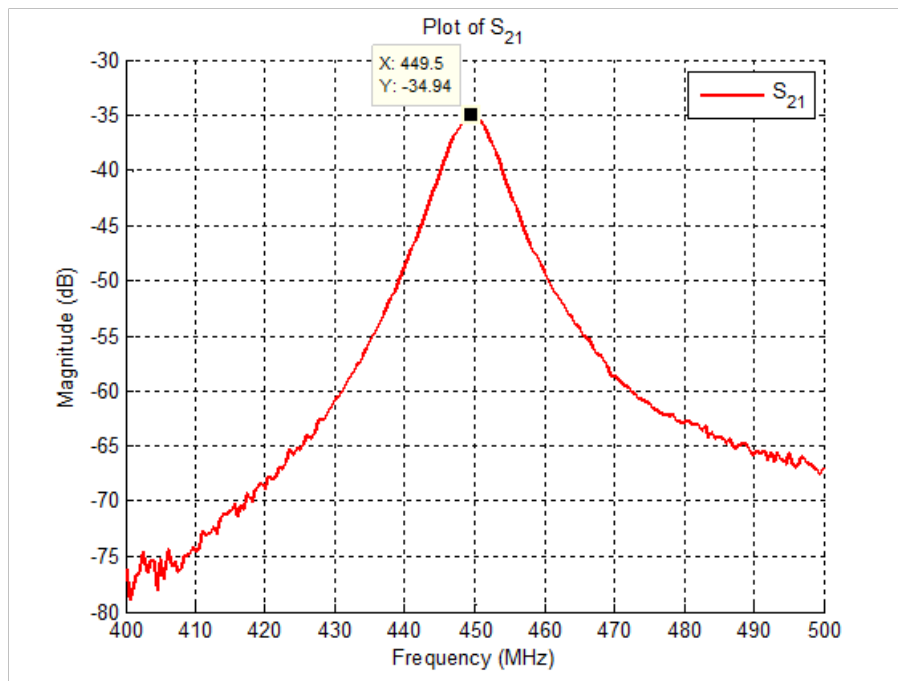
(b) S_{21} curve for free space

FIGURE 3.13: Miniaturized ECLA prototypes experimental setup in free space
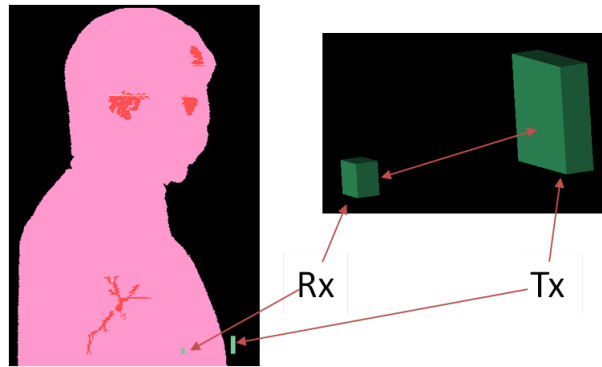
(a) XF7 Setup with human body model
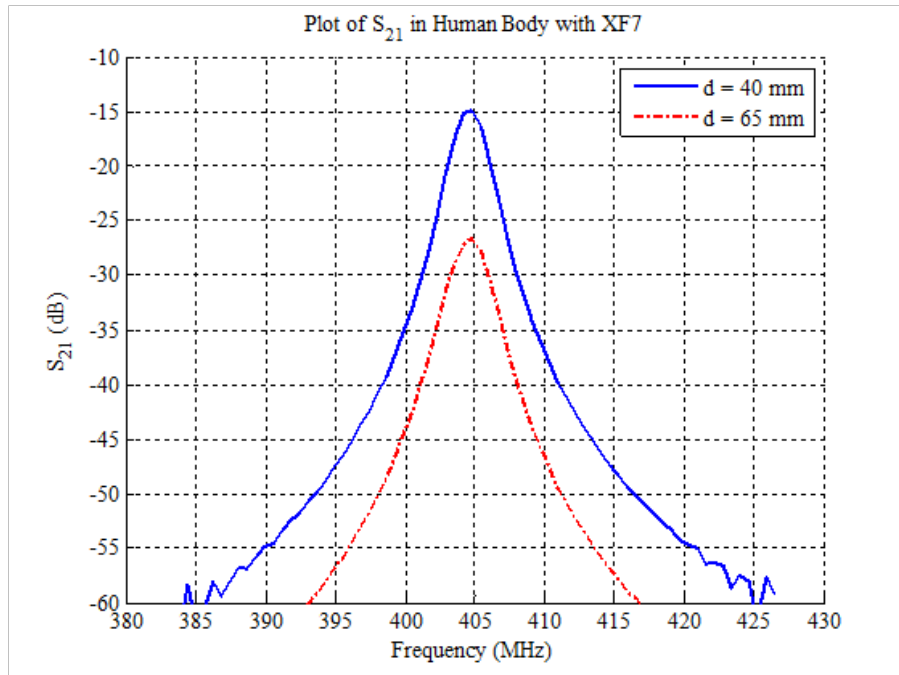
(b) S_{21} curves from XF7

FIGURE 3.14: Miniaturized ECLAs modeled in XF7 with a human body model at MICS band
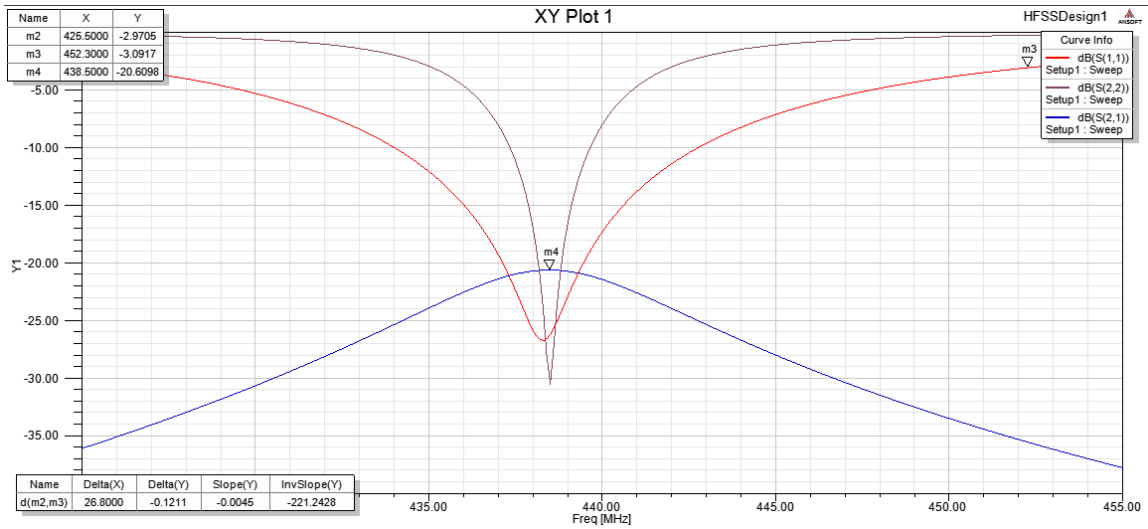
(a) HFSS $d = 40$ mm
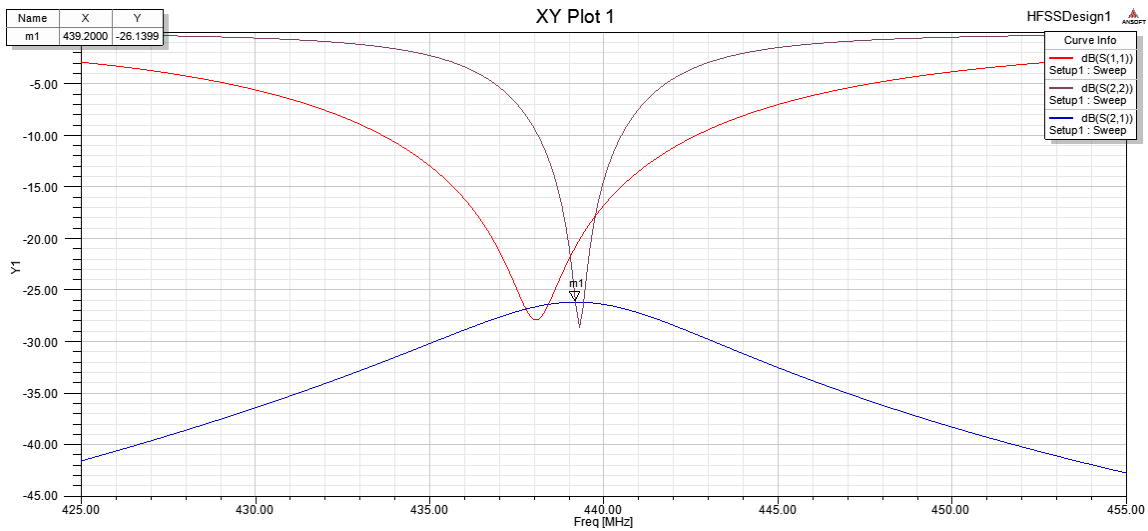
(b) HFSS $d = 65$ mm

FIGURE 3.15: Miniaturized ECLAs modeled in HFSS for a pork-based phantom

mm for an implanted antenna in the chest region. The results are very encouraging mainly due to the fact that the implanted antenna sits in front of the lungs that are primarily air-filled.

In order to actually be able to test the setup in an environment that emulates the human body, a tub of ground pork meat can be used. In order to calculate the electrical properties of the meat, the weighted average of human protein and fat values in the ratio 2:1 (assuming that pork muscle and fat values share the same electrical nature as corresponding human tissues) is taken for finding the required dielectric constant and conductivity. These values are obtained for a frequency of 403 MHz and summarized in Table. 2.1.

$$\bar{\epsilon}_r = \frac{11.6 + 2 \times 58.8}{3} = 43.067$$
$$\bar{\sigma} = \frac{0.08 + 2 \times 0.84}{3} = 0.587 \, \text{S/m}$$
$$\bar{\rho} = \frac{920 + 2 \times 1040}{3} = 1000 \, \text{kg/m}^3$$

With these values, a one-layer equivalent model was created in HFSS with dimensions of $90 \times 90 \times 180 \text{mm}^3$ with the Tx facing the $180 \times 90 \text{mm}^2$ face of the pork model in a setup similar to that shown in Fig. 3.10. The resulting curves are shown in Fig. 3.15.

The experimental setup corresponding to the HFSS experiment and the resulting measured S-parameters are shown in Fig. 3.16 for two distances of 40 mm and 65 mm, respectively. As shown, an $|S_{21}|$ of -25dB was obtained at a distance of 40mm through the pork phantom[9].

Some further modifications to the implanted design may be made as shown in Fig. 3.17 to reduce the SAR. For further reading on the performance of the ECLA in the human body, please refer to Ibraheem and Manteghi [2014a,b].

---

[9]These results were presented at the IEEE AP-S/URSI 2014 Conference in Memphis, TN, USA.

(a) Experimental setup
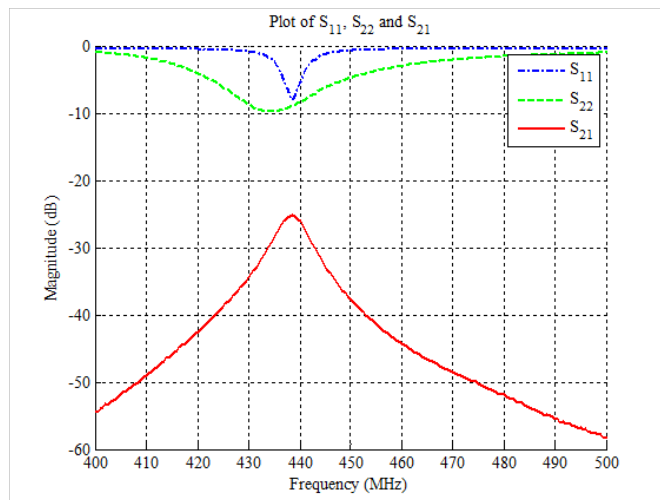
(b) $d = 40$ mm
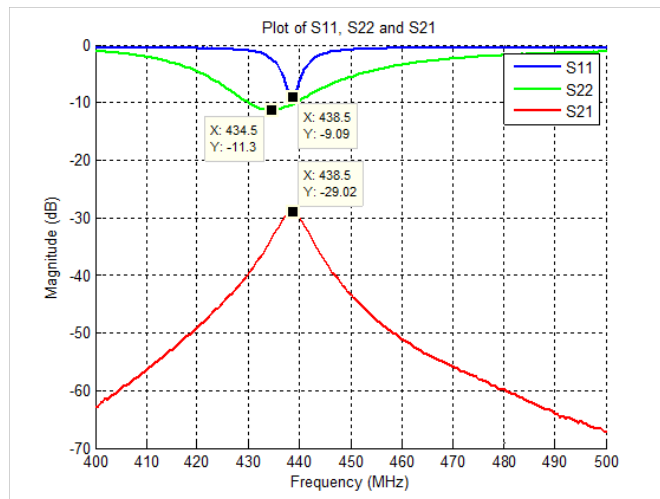
(c) $d = 65$ mm

FIGURE 3.16: Experimental setup for a pork-based phantom

(a) Modified dielectric coating   (b) SAR for an implanted ECLA in the head
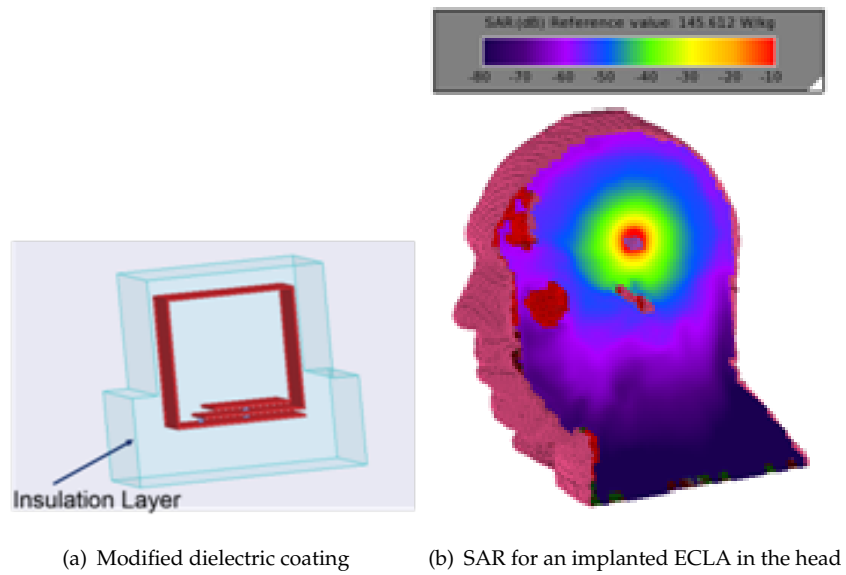
FIGURE 3.17: Medical applications

Chapter 4

System Design

4.1 Overview

In this chapter, we will focus on the design of the oscillator and load to complete the Wireless Power Transfer (WPT) system. Specifically, some design methods for a negative resistance oscillator will be presented and the ways by which a load can be analyzed at the source side are discussed. The objective here is to maximize the Power Delivered to Load (PDL) by choosing the right system goals and obtaining the highest efficiency throughout the system - from source to load. For example, as seen from the last chapter, for most implanted applications that function off of a coin cell (CR2032 Li/MnO type), the maximum power deliverable is of the order of 0.5 W. With an S_{21} of -20 dB, this implies 500 mW of continuous power to an implanted device at a depth of 5 cm would require a 50 W transmitter outside the human body. For most applications, this is a rather high value but the idea is that such a system would have to be able to compensate for the path loss (1-PTE) by delivering suitable power at the transmit antenna port. Typically, 100 mW of power is a sufficient figure [Catrysse et al., 2004, Ghovanloo and Najafi, 2007, Wang et al., 2006] to deliver to an implanted device.

In the literature, considerable effort has gone into designing systems with high Power Transfer Efficiency (PTE) and high PDL (as seen in Chapter 2); however, an effort to study the effect of

the loaded WPT system on a stand-alone source has not been studied to the best of the author's knowledge. Some patent arts establish the use of negative resistance generators but no analysis is presented on how to design these oscillators keeping in mind the figures of merit of a WPT system [Mohammadian, 2009, Toncich et al., 2009]. In this chapter, a negative resistance based oscillator design is proposed for a WPT transmitter. The need for such an oscillator stems from the fact that the antenna is a one-port device and in such cases it is difficult to efficiently incorporate it into the feedback loop of a conventional high-power and high-efficiency oscillator design. Although ultra high efficiency oscillators are not discussed here (such as Class E and above), some design methodologies are discussed from the specific viewpoint of a WPT system and presented in this chapter. Both the free-space and implanted cases discussed in Chapter 3 are considered here and design presented. However, only the free-space case is fabricated.

Although this chapter primarily discusses oscillator design, it is titled *System Design* as we now integrate the previously discussed WPT terms into the oscillator design process, thus completing a closed system where the parameters are interlinked to each other.

4.2 Oscillator Design

As discussed above, the reason that we need a negative resistance oscillator is due to the fact that we are feeding an unbalanced antenna like the Electrically Coupled Loop Antenna (ECLA) . Unlike inductive loops that are common in WPT literature which can be fed by incorporating them into the feedback network of classical oscillator designs like a Colpitts oscillator, a negative resistance oscillator has its own set of design challenges but like any other oscillator also follows the same basic principles. In a feedback oscillator, the feedback path and the associated gain and phase values can be computed quite easily. Doing so may not be inherently apparent but the right analysis shows the similarities in design as well as brings out the load or matching network requirements. There are a few design approaches that can be taken that lead to some very useful insights and in this section we will try to cover a couple of them from a WPT perspective. A thorough and rigorous non-linear analysis can often lead to a very accurate prediction of the final amplitude and frequency level of the oscillation signal. The goal here

is to design an oscillator that operates at the final operational power level of the source ECLA with high efficiency while keeping components at a minimum to keep system complexity low.

4.2.1 Negative Resistance Oscillators

At first glance, a negative resistance may seem non-physical but it can be understood intuitively as an active-device based phenomenon (since passives can only lead to loss/positive resistance). Thus, from an RF perspective, we see that these are the loads that lie outside of the Smith chart. In order to achieve negative resistance, the most important requirement is that of the design of a proper termination network for a given load impedance such that the magnitude of the reflection coefficient, $|\Gamma_{in}|$, is larger than 1 (outside the Smith Chart). Gonzalez [1984], Grebennikov [2007] present some good analytical and empirical techniques for the establishment of oscillations, their stability, phase noise characteristics and other important parameters.

Generally, for high power applications as well as for two-port analysis, a tuned base (inductor to base) is employed as the reflection coefficients are then seen to trace constant susceptance curves with increasing signal level [Rhea, 1995]. These are then negative *conductance* devices as they require a parallel resonator structure. The ECLA can be seen from its equivalent circuit to resemble a parallel resonator. A tuned base transistor can also be thought of as a Clapp oscillator. In order to better understand the working of oscillators, we establish the mathematical formulation in the next section.

4.2.2 Mathematical Description

We begin by considering Fig. 4.1 where a conventional feedback network system is shown [Gonzalez, 1984]. We can define some of the quantities shown as
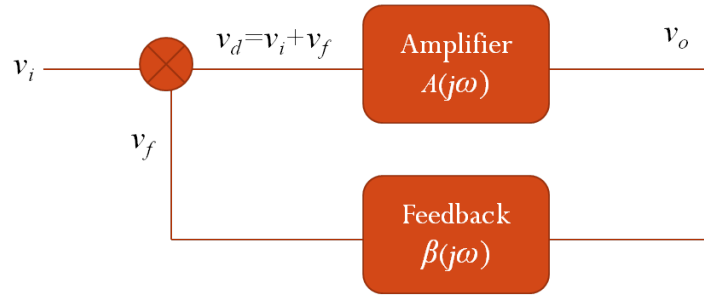
FIGURE 4.1: General Oscillator block analysis
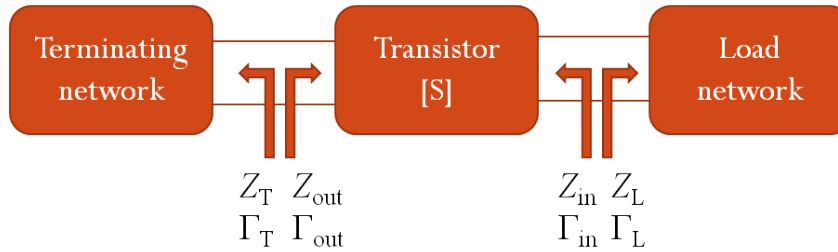
FIGURE 4.2: Two-port oscillator analysis

$$v_o = A(j\omega)v_d \tag{4.1}$$

$$v_f = \beta(j\omega)v_o \tag{4.2}$$

$$v_d = v_i + v_f \tag{4.3}$$

Here, $A(j\omega)$ can be considered to be the open loop amplifier gain and $\beta(j\omega)$ the feedback path's transfer function. Then, the close-loop gain or transfer function is given by

$$A_{cl}(j\omega) = \frac{v_o}{v_i} = \frac{A(j\omega)}{1 - \beta(j\omega)A(j\omega)} \tag{4.4}$$

Then the Barkhausen criteria is achieved for $v_i = 0$ (or by finding the poles of Equation 4.4), i.e.

$$\beta(j\omega)A(j\omega) = 1 \tag{4.5a}$$

$$\text{where} \quad \beta(j\omega) = \beta_r(\omega) + j\beta_i(\omega) \tag{4.5b}$$

$$A(j\omega) = \frac{1}{\beta_r(\omega)} \tag{4.5c}$$

$$\beta_i(\omega) = 0 \tag{4.5d}$$

These equations establish the gain and frequency of the oscillations. It can also be seen that the oscillation condition survives as long as

$$R_{IN}(A_o, \omega_o) + R_L(\omega_o) = 0 \tag{4.6}$$

and

$$X_{IN}(A_o, \omega_o) + X_L(\omega_o) = 0 \tag{4.7}$$

which translates to the point that the oscillations exist as long as the load resistance is less than the magnitude of the negative resistance while maintaining phase conditions. Also, from Kurokawa [1969], we find that the stability of the oscillations can be predicted by

$$\frac{\partial R_{IN}(A)}{\partial A}\Big|_{A=A_o}\frac{dX_L(\omega)}{d\omega}\Big|_{\omega=\omega_o} - \frac{\partial X_{IN}(A)}{\partial A}\Big|_{A=A_o}\frac{dR_L(\omega)}{d\omega}\Big|_{\omega=\omega_o} > 0 \tag{4.8}$$

In most cases, $\frac{dR_L(\omega)}{d\omega} = 0$, but this is only true for a truly static load. In the case of WPT, this would mean a fixed load at a fixed distance having some known coupling factor. In the case where $\frac{dR_L(\omega)}{d\omega} = 0$, we can arrive at the relation

$$R_L = \frac{R_0}{3} \tag{4.9}$$

to maximize the oscillation power, where R_0 is the termination network resistance (if Termination Network impedance is given by $Z_T = R_0 + jX_0$)[Gonzalez, 1984]. This provides a good starting point for the oscillator design problem.

Consider Fig. 4.2 where a two-port system is shown with one port labeled the termination port while the other is the load port where the termination and load networks are connected respectively. Also, after some manipulation, we can arrive at the two-port RF equivalent of the oscillation conditions [Gonzalez, 1984], giving

$$\Gamma_{IN}\Gamma_L = 1 \tag{4.10}$$

$$\Gamma_L = \frac{1}{\Gamma_{IN}} = \frac{1 - S_{22}\Gamma_T}{S_{11} - \Delta\Gamma_T} \tag{4.11}$$

$$\text{or} \quad \Gamma_T = \frac{1 - S_1\Gamma_L}{S_{22} - \Delta\Gamma_L} \tag{4.12}$$

$$\Gamma_{OUT} = \frac{S_{22} - \Delta\Gamma_L}{1 - S_{11}\Gamma_L} \tag{4.13}$$

$$\Gamma_{OUT}\Gamma_T = 1 \tag{4.14}$$

General Design Procedure [Gonzalez, 1984]

1. Use a potentially unstable transistor at the design frequency

2. Design a terminating network to make $|\Gamma_{IN}| > 1$ using series or shunt feedback.

3. Design a load network to resonate Z_{IN} such that

$$X_L(\omega_0) = -X_{IN}(\omega_0) \tag{4.15}$$

and

$$R_L = \frac{R_0}{3} \tag{4.16}$$

It can also be seen that both load and termination networks oscillate at resonance and that the actual frequency of oscillation is controlled by when the positive and negative resistances cancel each other out in the network. Hence, some degree of tuning will be required. Also note that since S-parameters are by their very nature small-signal and linear measurements/characteristics of the device, some variation from the predictions should be expected as oscillators are non-linear systems (by the virtue of their large-signal behavior).

An alternative design approach based on material given in Rhea [1995] will be presented along with the simulation results in following sections.

Transformation

Notice that the equations presented above give the design values in case of a constant load. Since we know that in the case of WPT, our load (as seen from the source) is not constant, some amount of flexibility is required in the termination network which is one of the more important problems associated with this method. However, if a convenient "calibration" curve or variation in load with distance information is at our disposal, then this information can be used to design a smarter source termination network. This is where the techniques presented in the previous chapters such as extraction of k from the equivalent circuit come into play. Thus, this information is embedded into the coupled antenna's reflection coefficient and can be used to incorporate coupling characteristics into the oscillator design. Also, since the oscillation conditions rely heavily upon the load impedance, we can achieve some amount of frequency tracking by virtue of the negative resistance design.

4.3   Simulation Results

In this section, we will aim to design and simulate a few circuits using the approach presented earlier while trying to maximize the efficiency and power delivered by the oscillator. It is, however, beneficial to study the Bode plots of the open loop (or two-port) network as an amplifier

to gain more insight into the problem[1]

Choice of Transistor

Although the circuits given in Rhea [1995] form the basis of the schematics given in the subsequent sections and which use the MRF559 transistor, we will use the MRF555 where possible as this is but a higher power version of the MRF559 ($I_c = 500$ mA vs $I_c = 150$ mA). Both are now mostly obsolete but the abundance of design schematics in the literature for these devices and their trusted RF performance makes them a good candidate for our application. The transistors used in the prototype were ordered from `RFparts.com`.

PBJT vs. S-Parameter models

ADS offers two models for us to work with, namely, a packaged BJT model containing all the known packaged parasitics, and an S-parameter model for a given set of bias conditions. Note that the former is a large-signal model and thus can be used for oscillator analysis while the latter is suitable for amplifier design and to study the response of the transistor in its linear region. A transient or harmonic balance analysis of the oscillator is not possible with the S-parameter model.

Note that to obtain the PBJT and S-parameter models, it is first necessary to unzip the design kits (RF Transistor Library) located in the "oalib" folder of the ADS installation directory. Analog Parts library contains the non-linear SPICE models of transistors for use at frequencies less than 10 MHz. Even though not suited for our purposes, it is compared to the PBJT and S-parameter models as an educational exercise below.

Fig. 4.3 shows the circuit setup to compare the various MRF559 models for a tuned base case with circuit DC conditions matching that of the S-parameter data. Fig. 4.4 shows the $[S]$ matrix values for the models for frequencies from 300 MHz to 1 GHz. Clearly, the S-parameter data is not at all very well-aligned with the PBJT results. This could be due to the difference in bias conditions that existed for the S-parameter data setup (which we have no access to sadly) that might change the feedback mechanisms in play for the S-parameter model vs the PBJT model.

---

[1] An old adage goes: to realize an amplifier, design an oscillator; to realize an oscillator, design an amplifier!
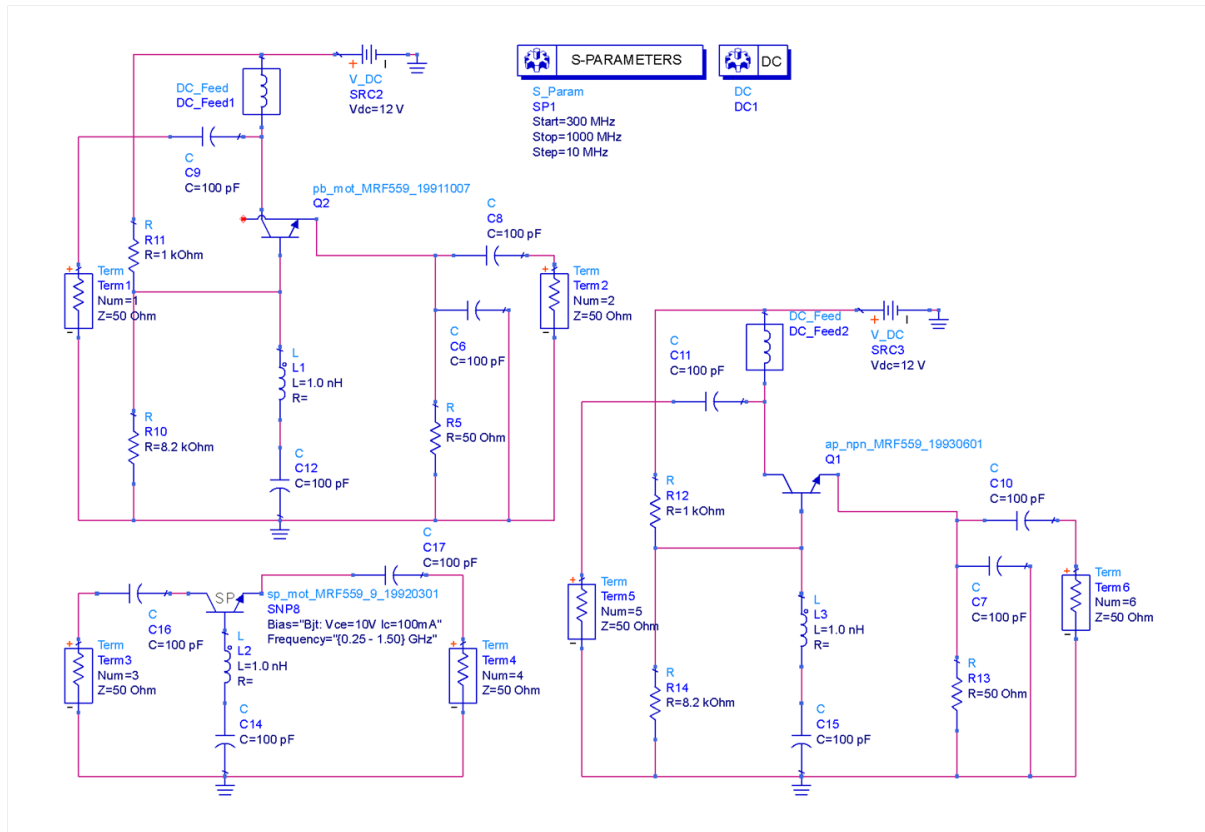
FIGURE 4.3: ADS Circuit test setup for MRF559 for PBJT, AP and S-parameter ADS models ($V_{CE} = 10$ V and $I_C = 100$ mA

The AP part is not so far away from the PBJT but obviously cannot be used in an RF sense. Note that the lowest frequency data available for these models is 250 MHz and hence the free-space case cannot be compared using these models. Also, S-parameter models for MRF555 do not exist in the ADS 2011 library.

From these results, it is clear that the best possible alternative is to go forward with the PBJT model for simulation results and to measure actual S-parameter when possible.

4.3.1 Implanted Applications

We will use the measured S-parameter data of the antenna in conjunction with the large-signal PBJT model of the MRF559 so as to obtain a desired frequency of operation at the resonant
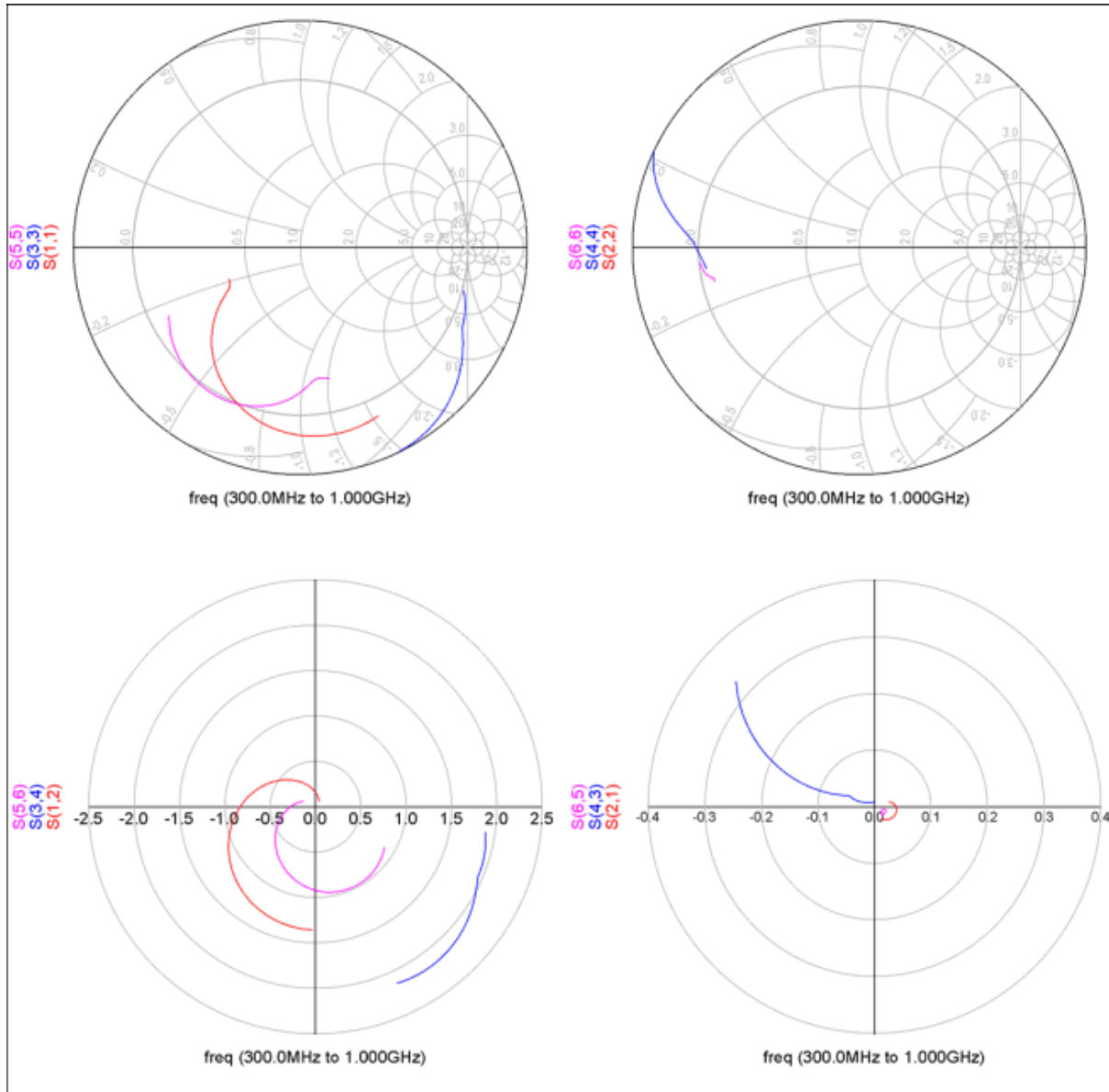
FIGURE 4.4: S-parameter curves for MRF559 for PBJT, AP and S-parameter ADS models ($V_{CE} = 10$ V and $I_C = 100$ mA

frequency of the antenna. At first, it may seem counter-intuitive to design an oscillator based on the measured linear S-parameter data but it is important to realize that the antenna itself is an LTI (Linear Time Invariant) system and the mostly non-linear component is that of the transistor which is modeled effectively by the ADS PBJT model.

Two-port analysis

The results presented here are the result of several iterations of design and simulation and only the final result is shown here in the interest of brevity and conciseness.

From Fig. 4.5, S-parameter data from Coilcraft is used to model the effect of "real" inductors on the circuits. The circuit is tuned so as to achieve maximum values of S_{11}, S_{22} while also achieving a phase reversal in the gain term (S_{12}). Fig. 4.6 shows the stability analysis of the system which shows the network is clearly unstable as $K < 1$ and $|\Delta| > 1$. From Fig. 4.7, a lower frequency is chosen for the two-port analysis and design as it was found (through various iterations) that the oscillator had a tendency to oscillate at roughly a 20-40 MHz higher frequency with tuning.

For the design of a terminating network for the measured antenna load, a MATLAB code is used to calculate the network values (see Appendix B).

Transient analysis

Fig. 4.8 shows the transient analysis setup in ADS. The measured antenna parameters (characterized from 300 - 500 MHz) are connected at the node marked 'Vterm' (Both Termination and Load ports oscillate and therefore can be used interchangeably. Also, there are some efficiency benefits to having a lower resistance value in the passive fixed network). The time response of the circuit is shown in Fig. 4.9 showing the buildup of oscillation in the network at the antenna port. The FFT of the (truncated) time response is given in Fig. 4.10 and shows that the maximum power is a slightly higher frequency of 480 MHz, which can be tuned down by proper tuning techniques (discussed in 4.3.4). Also note the excellent 2nd harmonic suppression (> 20
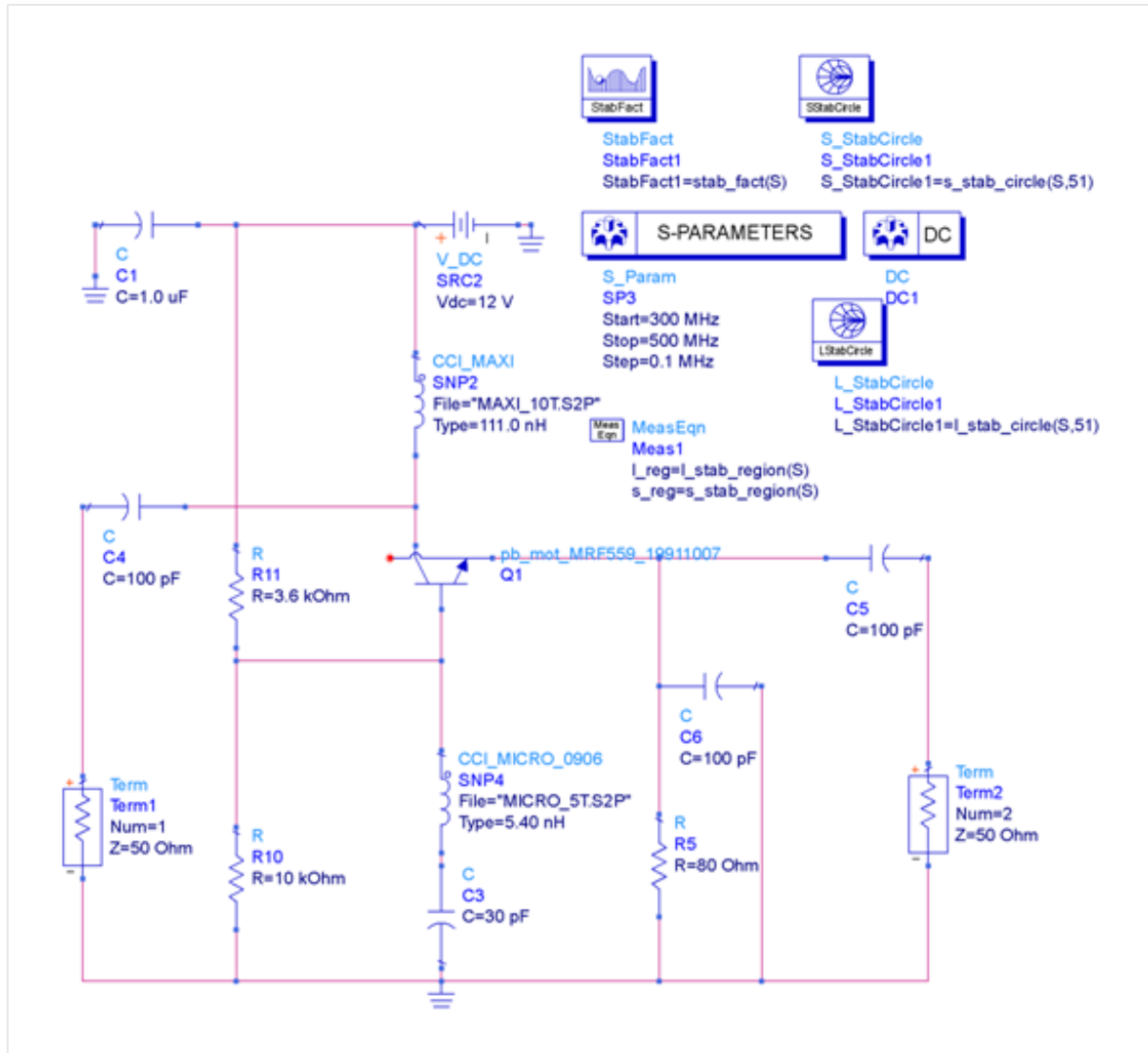
FIGURE 4.5: Two-port analysis ADS setup for 440 MHz

dBc) which is due to the small capacitor terminated in ground at the antenna port. As this is a Class A design, a lot of quiescent power is wasted in the bias networks and thus results in poor efficiency.
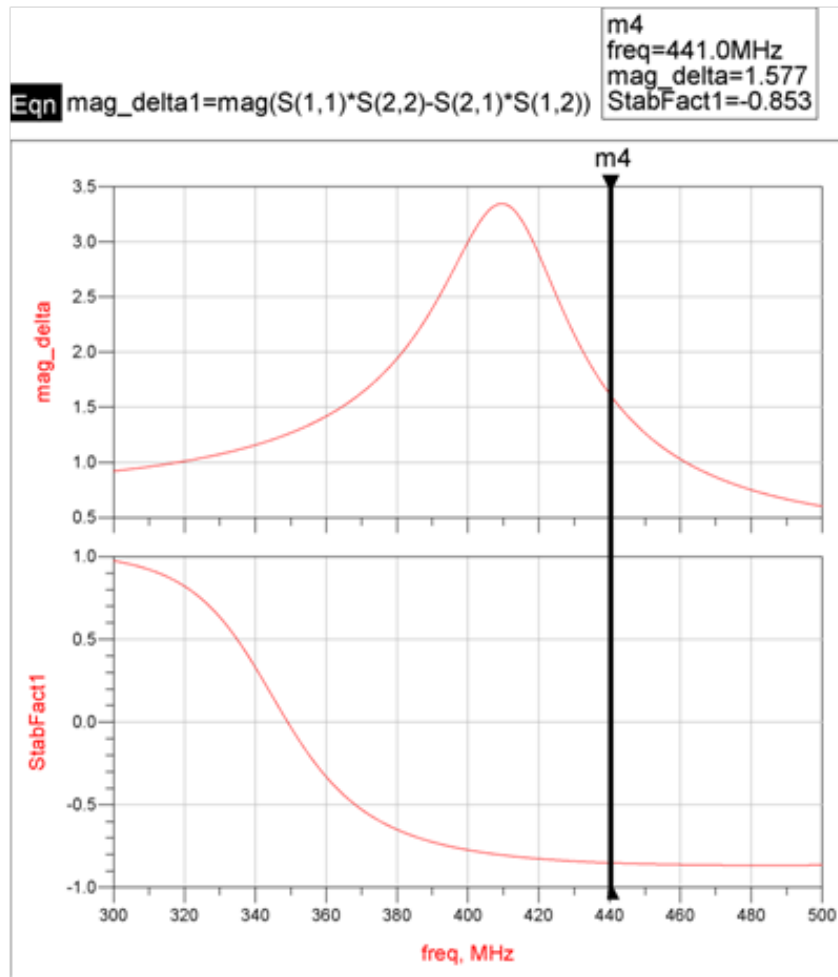
FIGURE 4.6: Two-port stability analysis for 440 MHz

4.3.2 Higher Power/Efficiency Design

An alternative approach to the one discussed in the previous section is to study the two-port system with the resonator in the network to achieve the gain and phase conditions discussed earlier at the target frequency [Rhea, 1995]. In this case, the non-antenna port is grounded via a capacitor for oscillation startup.

Although oscillations were achieved at near the target frequency in the previous design, the poor efficiency leads us to design a more efficient network. This section contains a design from
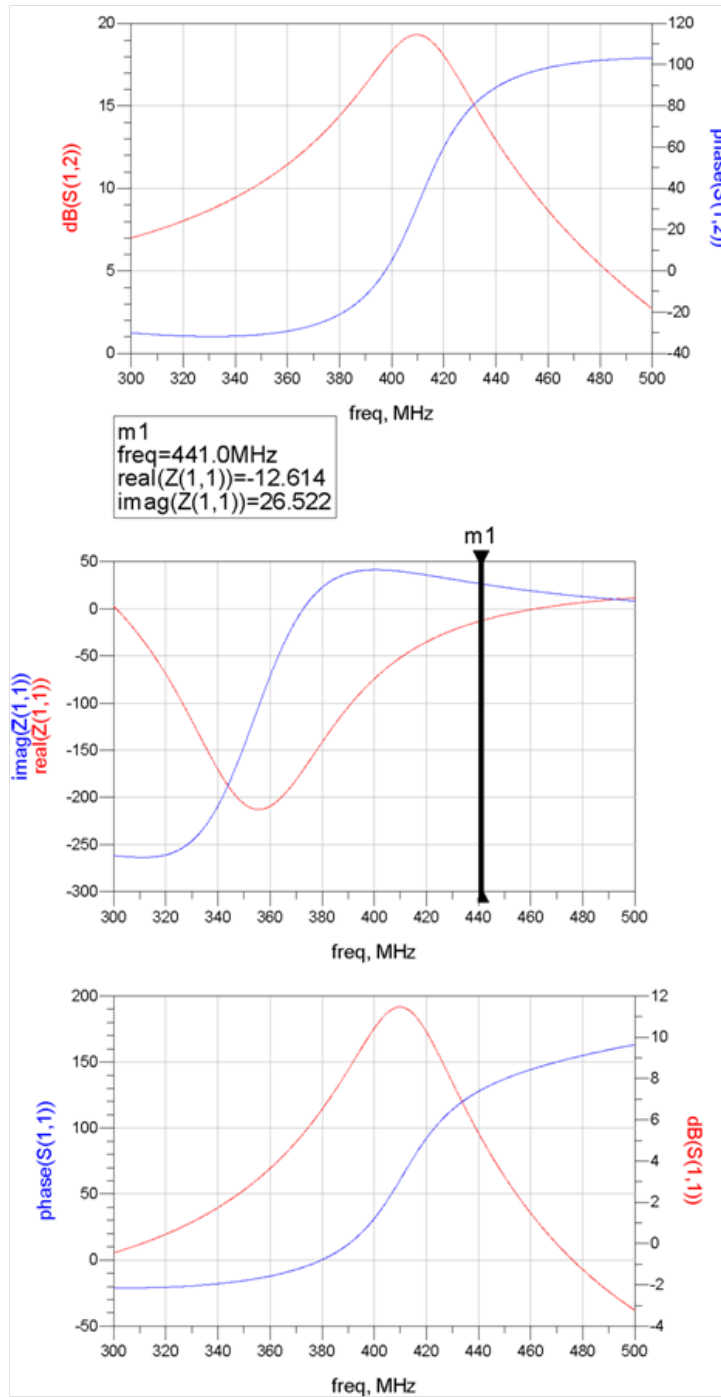
FIGURE 4.7: Two-port analysis S-parameter data for 440 MHz
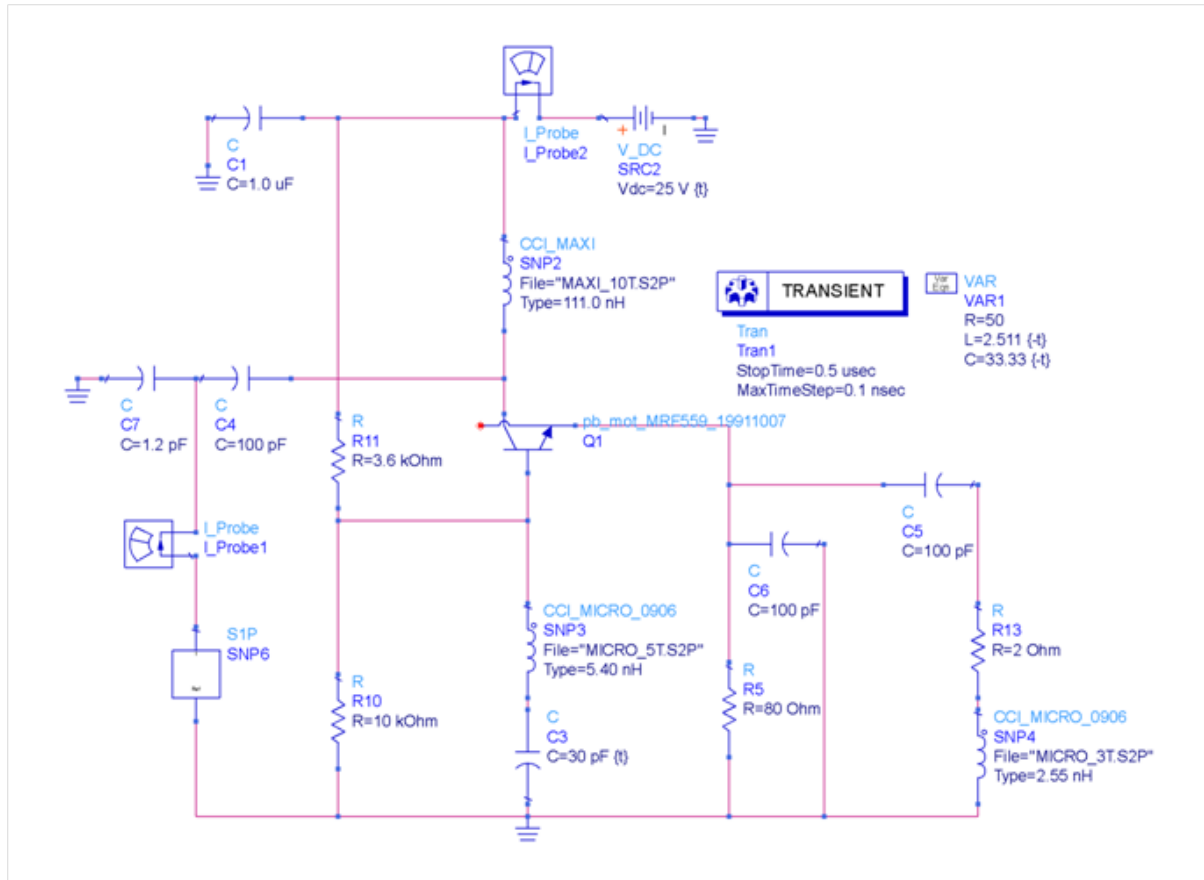
FIGURE 4.8: Transient analysis ADS setup for 440 MHz

Rhea [1995] that proposes a hybrid Class A and C type operation resulting in higher operating efficiency and thus, power.

The proposed design is shown in Fig. 4.11 with the results in Fig. 4.12 and Fig. 4.13. The resulting frequency is higher than expected but we can see that the efficiency is pretty high thus validating the use of this approach. Some tuning may be required post-fabrication to achieve the correct oscillation frequency. Also note that the peak current does not exceed the device rating of 500 mA.
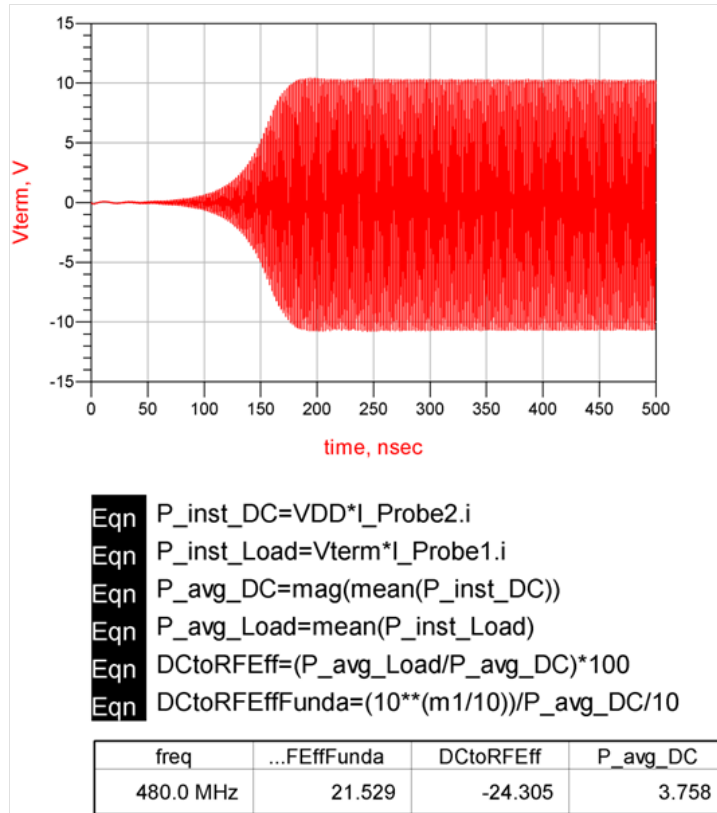
FIGURE 4.9: Time progression data for 440 MHz

4.3.3 Free-space Application

For the free-space case, we use the measurement data from an ECLA resonating at 39.34 MHz and re-design the high-efficiency design mentioned above with an MRF555 as in such use cases, practical PDL is needed to be much higher than the implanted case.

Two-port analysis

The circuit, reflection coefficients, stability and gain, phase information is presented in Fig. 4.14, Fig. 4.15 and Fig. 4.16.
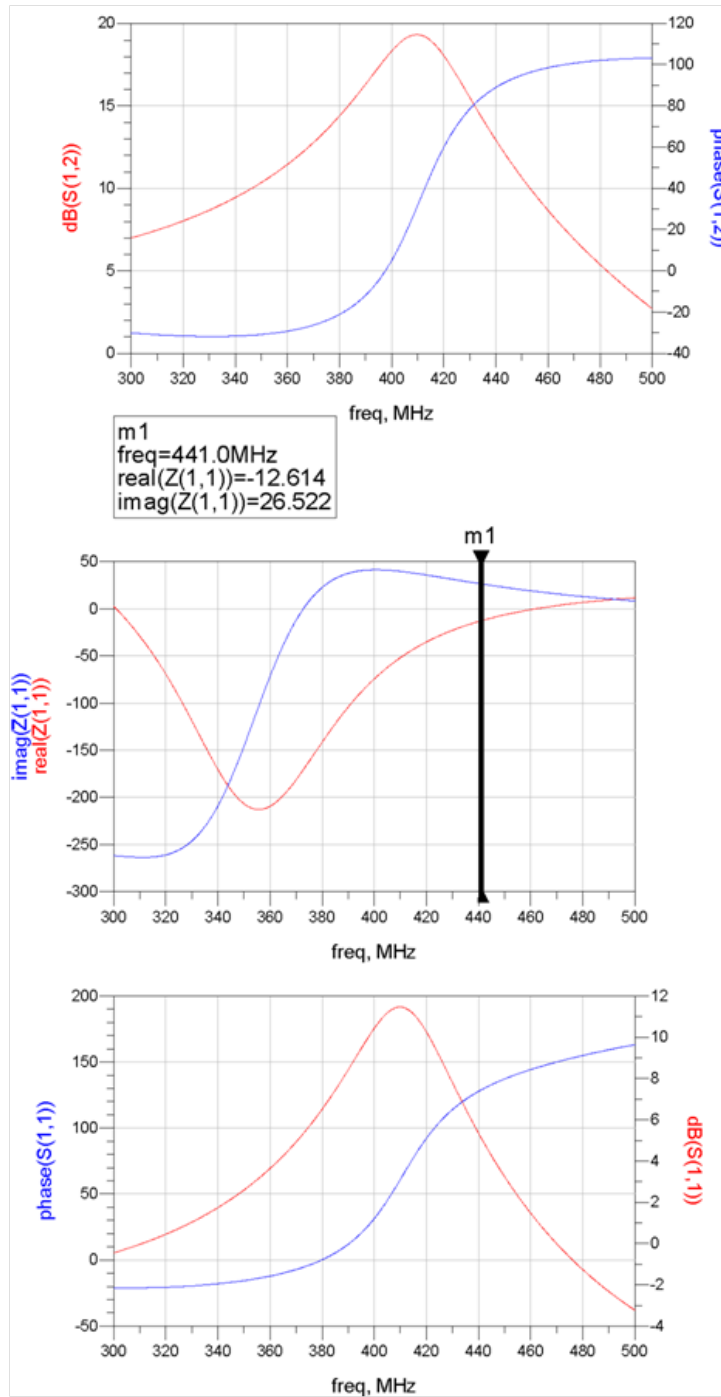
FIGURE 4.10: Frequency analysis of transient data for 440 MHz

FIGURE 4.11: Transient analysis ADS setup for High Power circuit

Transient analysis was found to fail in this case due to a lack of DC convergence at the base of the transistor. Despite numerous attempts at fixing this error, it would not go away. Considering the success of the method of open loop two-port analysis in the implanted application case, a prototype design is fabricated with values obtained from two-port simulation results. Clearly, some work needs to be done to be able to achieve oscillation especially considering that the relationship between actual device and the PBJT has not yet been established.

FIGURE 4.12: Time progression and current data
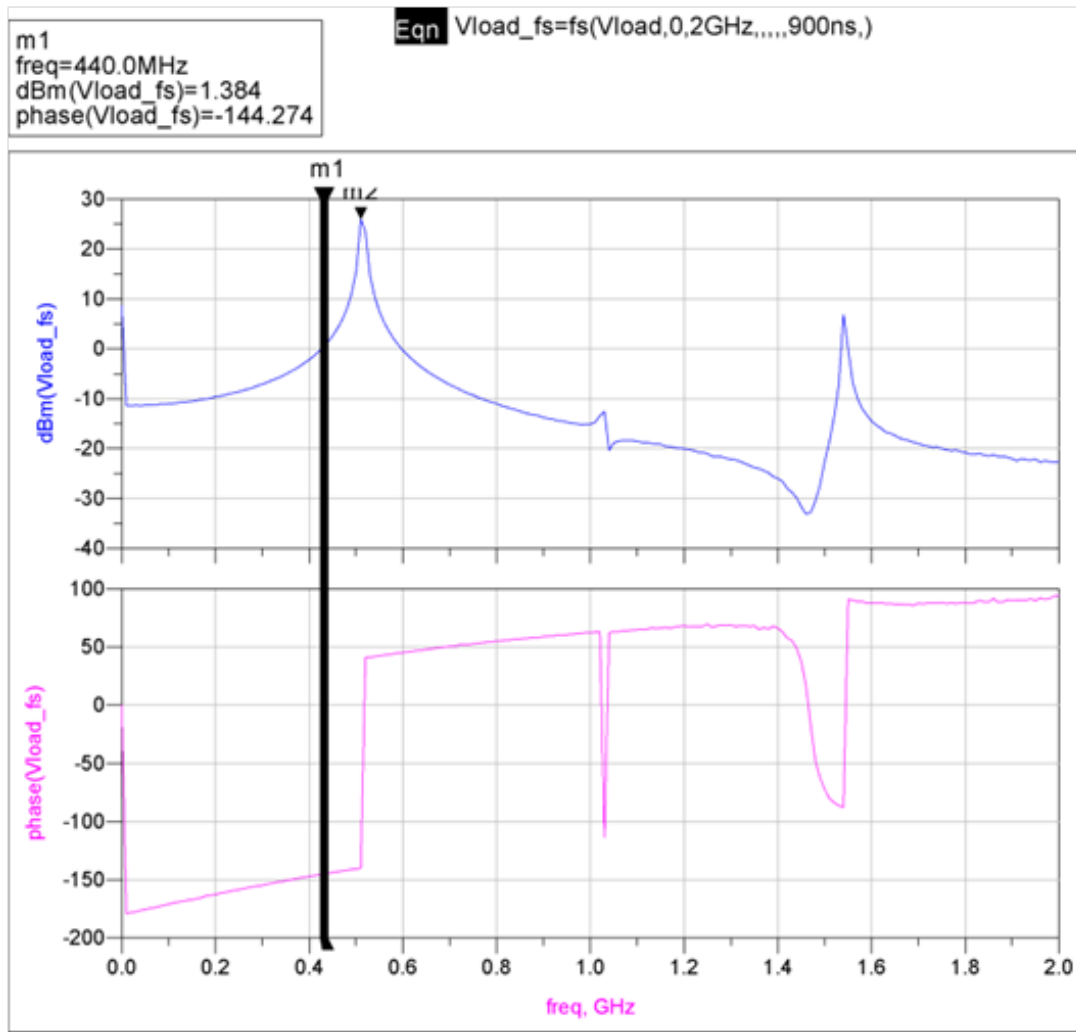
FIGURE 4.13: Frequency analysis of transient data

4.3.4 Tuning the Oscillator

I For adjusting the frequency of oscillation, the oscillator is most sensitive to the tuned base inductor and capacitor combination (in that order).

II For more power when a resistor bias network is used, adjusting the values of the voltage divider to gain more I_B is sufficient. However, note that the device absolute ratings need to be kept in mind. Increasing the source DC voltage also helps in raising the power level
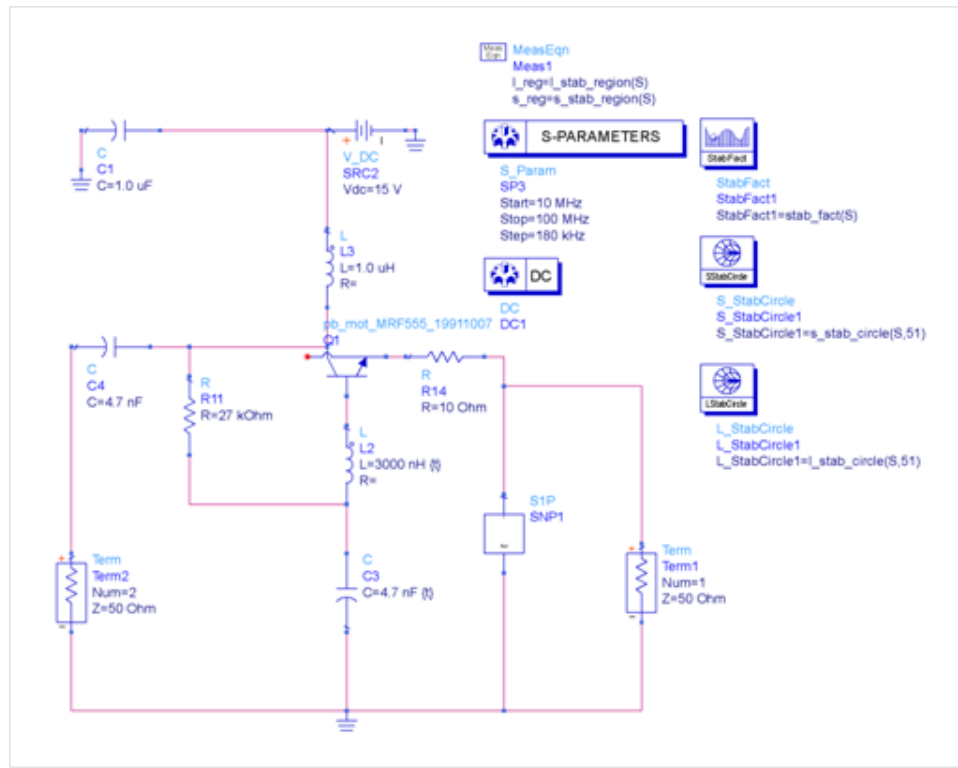
FIGURE 4.14: Two-port S-parameter analysis ADS setup for 39 MHz

to a certain extent but oscillation stability may be sensitive to the base resistor values. Tuning the termination network also results in higher output power.

4.4 Fabrication

Toroidal inductors with a T50-6 (yellow) cores were wound for the required inductances of 1μH (16 turns) and 3μH (27 turns)[2] [3]. These Iron powder cores have an optimum frequency range of 3-50 MHz.

---

[2]http://toroids.info/T50-6.php
[3]http://www.66pacific.com/calculators/toroid_calc.aspx
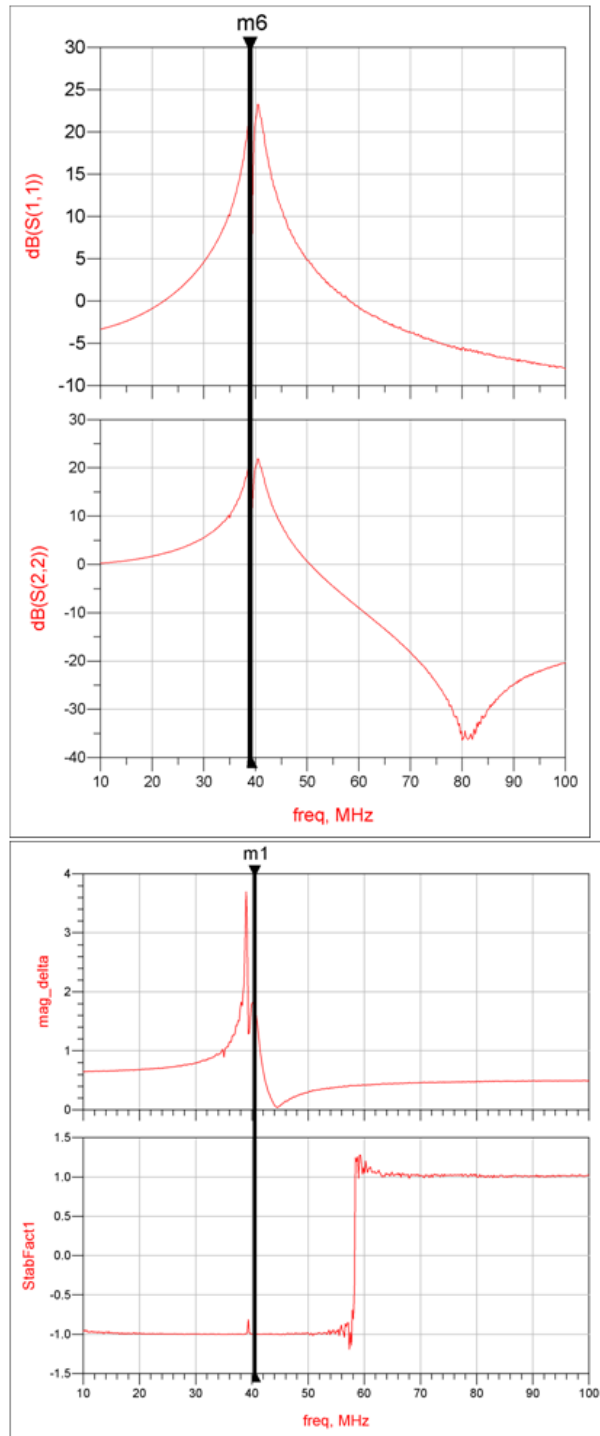
FIGURE 4.15: S_{11}, S_{22}
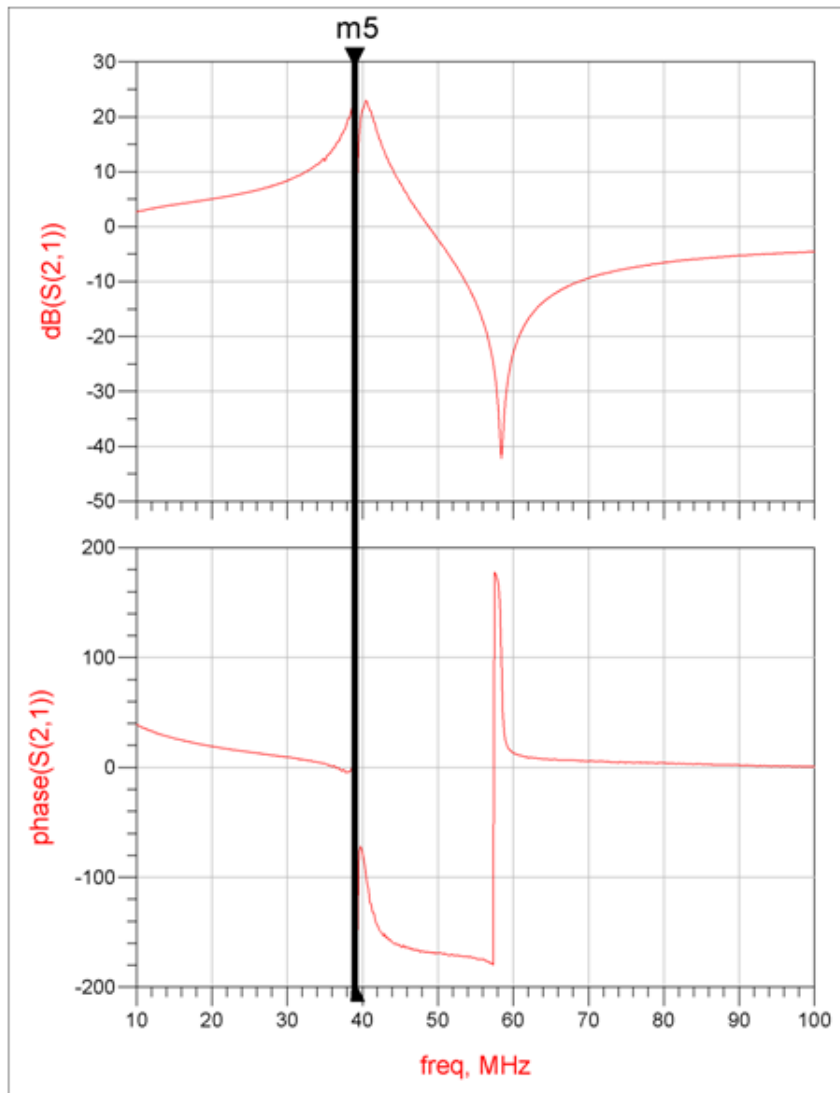
FIGURE 4.16: Gain, phase data of S_{21}

From Fig. 4.17, the non-electrolytic capacitors are 4.7 nF each and the resistor is 27 kΩ. One of the emitter pins is left floating. However, this design didn't seem to work and consequently, other designs need to be evaluated.
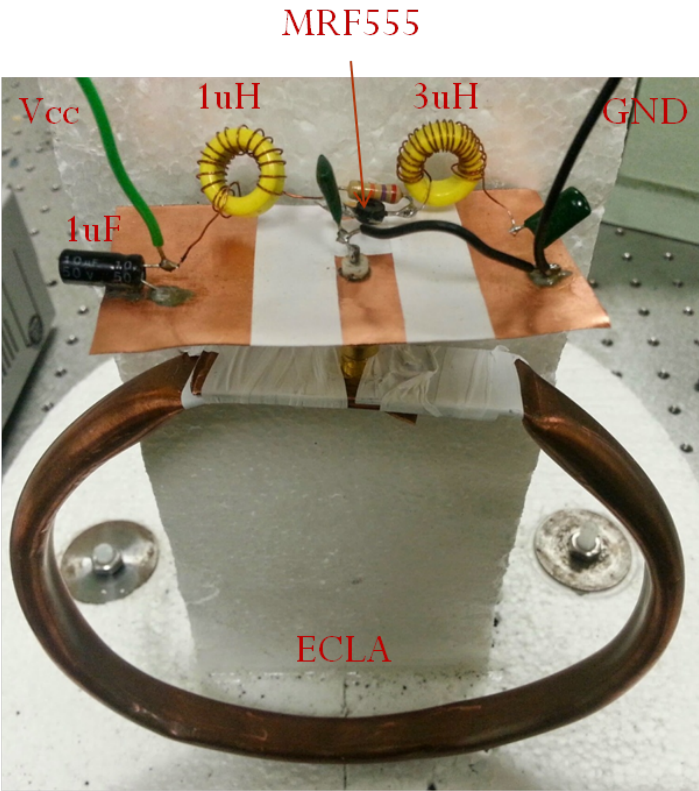
FIGURE 4.17: Prototyped circuit for 39 MHz

Chapter 5

Conclusions and Future Work

5.1 Conclusions

In this thesis, various aspects of a Wireless Power Transfer (WPT) system design have been considered, starting from the analysis of WPT systems using various theoretical techniques for both free-space and implanted applications to the design of high-Q antennas for coupling and finally the oscillator design to power such applications. It was shown that the Power Transfer Efficiency (PTE) and Power Delivered to Load (PDL) of the system, though related to each other, can both be independently maximized without simultaneously maximizing both of them. Thus, for a practical system where PDL is most important, a system design perspective yields the tradeoffs between PTE and PDL even more clearly. The requirements for various WPT couplers were studied and the Electrically Coupled Loop Antenna (ECLA) was proposed as a suitable high-Q resonator for coupling. Miniaturization of the ECLA for implanted applications was studied and some design models proposed for various form factors. Further, experimental results validated the use of ECLAs for implanted applications when manufactured with suitable processes. A negative resistance oscillator was proposed to integrate the coupling parameters into the system design. Various circuit topologies were studied for their gain, efficiency and frequency dependence. Even though a successful prototype did not result

(mainly due to the high-Q nature of the ECLA), the design and prototyping efforts given here should provide a platform from which a working prototype may be fabricated.

5.2 Future Work

This thesis gives but a preliminary analysis of the scope of system design tools to synthesize a complete WPT system. Further work must be done to create a practical system. The author believes that the following points give good direction to future research in this area.

- **Antenna and EM analysis at coupling frequency(/ies) for tight and moderate coupling**: Preliminary results show some interesting results that need to be thoroughly studied. Fig. 5.1 shows a 10 dB drop in far-field gain at the higher frequency that arises due to frequency splitting of tight coupling. This means that most of the energy gets coupled to the load at this frequency and thus, this frequency needs to be preferentially targeted for operation at maximum PDL.

- **Study the variation in Q and damping factor** by having receiver circuitry that synchronizes with the transmitter to give the best overall system performance. For example, a circuit topology or receiver feedback system that involves manipulation of the load conditions (say, a sweep of the resistance over a known value and period of time) that are easily detectable to the oscillator as variation in load pull can be exploited to get a better understanding of the k of the link(s) and modify the matching impedances on the fly and perform optimally at any distance or operating point.

- **Use an array of transmitter and receiver antennas** to direct energy efficiently. Possibility of exploiting supermodes by having side-by-side transmitters.

- Study the **effect of having multiple receivers** on overall coupling [Lee and Cho, 2015].

- **Better, efficient circuitry** is needed. It might be easier to use a Phased Locked Loop (PLL) and a Power Amplifier to achieve better frequency stability, more power and circuit flexibility.
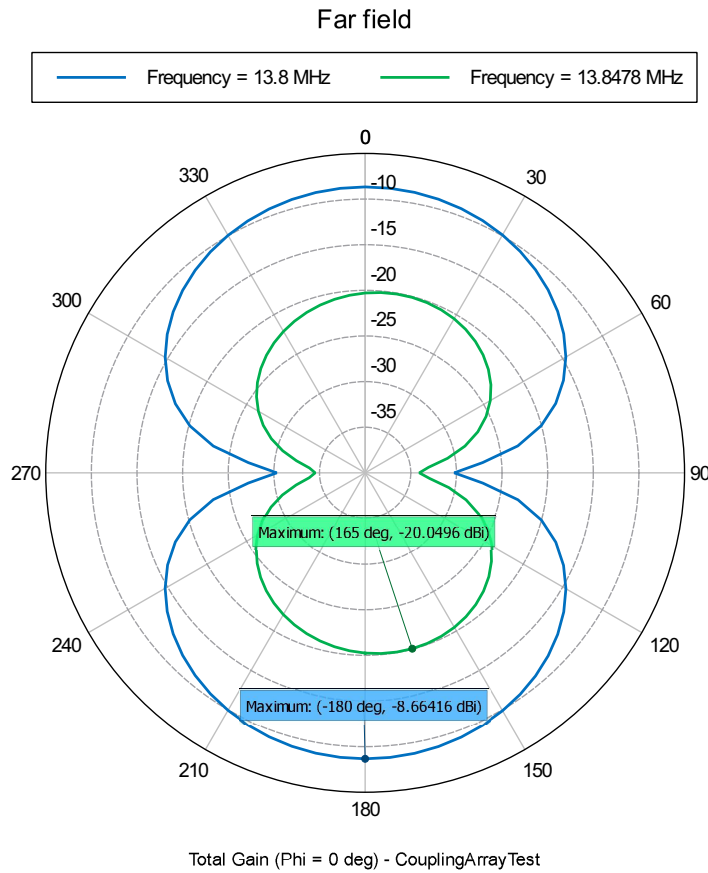
FIGURE 5.1: Radiation Pattern for Coupled ECLA system at the two highest $S_{(}21)$ frequencies

- **Oscillator load pull needs to be studied** to better understand the optimum load conditions and operate the circuit at optimum power. Current design does not take into account optimum power operating point for the oscillator as this is typically a measured characteristic due to the non-linearities involved. An NVNA (non-linear VNA) is typically required for these kind of large-signal measurements.

- Heavily miniaturized implanted antenna design can be investigated. Also, a planar form of the ECLA can be studied for low profile antenna applications.

- Using a signaling mechanism, such as an FSK (Frequency Shift Keying) scheme discussed in Salehi and Manteghi [2014], Salehi et al. [2013] or Ghovanloo and Najafi [2004], Inanlou et al. [2011], communications between the transmit and receive coils can be performed

without the need of another wireless channel (as in the case of Rezence and other commercial offerings), thus minimizing cost.

- Adaptive frequency and impedance control can be explored to maximize efficiency [Ping et al., 2008, Poon et al., 2007, Sample et al., 2013].

Bibliography

Arbabi, A. and Safavi-Naeini, S. (2012). Maximum gain of a lossy antenna. *Antennas and Propagation, IEEE Transactions on*, 60(1):2–7.

Azad, U., Jing, H. C., and Wang, Y. E. (2012). Link budget and capacity performance of inductively coupled resonant loops. *Antennas and Propagation, IEEE Transactions on*, 60(5):2453–2461.

Brown, W. C. (1996). The history of wireless power transmission. *Solar energy*, 56(1):3–21.

Catrysse, M., Hermans, B., and Puers, R. (2004). An inductive power system with integrated bi-directional data-transmission. *Sensors and Actuators A: Physical*, 115(2):221–229.

Chu, L. J. (1948). Physical limitations of omni-directional antennas. *Journal of applied physics*, 19(12):1163–1175.

Collin, R. and Rothschild, S. (1964). Evaluation of antenna q. *Antennas and Propagation, IEEE Transactions on*, 12(1):23–27.

Commission, E. R. (1995). Human exposure to electromagnetic fields, high frequency (10 khz to 300 ghz).

Davis, W., Yang, T., Caswell, E., and Stutzman, W. (2011). Fundamental limits on antenna size: a new limit. *Microwaves, Antennas & Propagation, IET*, 5(11):1297–1302.

Federal Communications Commission, U. (1996). In the matter of guidelines for evaluating the environmental effects of radiofrequency radiation.

Fotopoulou, K. and Flynn, B. W. (2006). Wireless powering of implanted sensors using rf inductive coupling. In *Sensors, 2006. 5th IEEE Conference on*, pages 765–768.

Gabriel, C., Gabriel, S., and Corthout, E. (1996). The dielectric properties of biological tissues: I. literature survey. *Physics in medicine and biology*, 41(11):2231.

Ghovanloo, M. and Najafi, K. (2004). A wideband frequency-shift keying wireless link for inductively powered biomedical implants. *Circuits and Systems I: Regular Papers, IEEE Transactions on*, 51(12):2374–2383.

Ghovanloo, M. and Najafi, K. (2007). A wireless implantable multichannel microstimulating system-on-a-chip with modular architecture. *Neural Systems and Rehabilitation Engineering, IEEE Transactions on*, 15(3):449–457.

Gonzalez, G. (1984). *Microwave transistor amplifiers: analysis and design*, volume 61. Prentice-Hall Englewood Cliffs, NJ.

Grebennikov, A. (2007). *RF and microwave transistor oscillator design*. John Wiley & Sons.

Guoxing, W., Wentai, L., Sivaprakasam, M., and Kendir, G. A. (2005). Design and analysis of an adaptive transcutaneous power telemetry for biomedical implants. *Circuits and Systems I: Regular Papers, IEEE Transactions on*, 52(10):2109–2117.

Hall, P. S. and Hao, Y. (2006). Antennas and propagation for body centric communications. In *Antennas and Propagation, 2006. EuCAP 2006. First European Conference on*, pages 1–7. IEEE.

Harrington, R. F. (1960). Effect of antenna size on gain, bandwidth, and efficiency. *J. Res. Nat. Bur. Stand*, 64(1):1–12.

Haus, H. A. et al. (1984). *Waves and fields in optoelectronics*, volume 464. Prentice-Hall Englewood Cliffs, NJ.

Heebl, J. D., Thomas, E. M., Penno, R. P., and Grbic, A. (2014). Comprehensive analysis and measurement of frequency-tuned and impedance-tuned wireless non-radiative power-transfer systems. *Antennas and Propagation Magazine, IEEE*, 56(4):44–60.

Hong, J.-S. G. and Lancaster, M. J. (2004). *Microstrip filters for RF/microwave applications*, volume 167. John Wiley & Sons.

Hui, S., Zhong, W., and Lee, C. (2013). A critical review of recent progress in mid-range wireless power transfer.

Ibraheem, A. and Manteghi, M. (2014a). Path loss inside human body using electrically coupled loop antenna at different frequency bands. In *Antennas and Propagation Society International Symposium (APSURSI), 2014 IEEE*, pages 977–978.

Ibraheem, A. A. Y. and Manteghi, M. (2014b). Performance of an implanted electrically coupled loop antenna inside human body. *Progress In Electromagnetics Research*, 145:195–202.

IEEE (2010). Ieee standard for safety levels with respect to human exposure to radio frequency electromagnetic fields, 3 khz to 300 ghz - amendment 1: Specifies ceiling limits for induced and contact current, clarifies distinctions between localized exposure and spatial peak power density. *IEEE Std C95.1a-2010 (Amendment to IEEE Std C95.1-2005)*, pages C1–9.

Inanlou, F., Kiani, M., and Ghovanloo, M. (2011). A 10.2 mbps pulse harmonic modulation based transceiver for implantable medical devices. *Solid-State Circuits, IEEE Journal of*, 46(6):1296–1306.

Jin, J.-M. (2011). *Theory and computation of electromagnetic fields*. John Wiley & Sons.

Jungsuek, O. and Sarabandi, K. (2012). Low profile, miniaturized, inductively coupled capacitively loaded monopole antenna. *Antennas and Propagation, IEEE Transactions on*, 60(3):1206–1213.

Karalis, A., Joannopoulos, J. D., and Soljačić, M. (2008). Efficient wireless non-radiative mid-range energy transfer. *Annals of Physics*, 323(1):34–48.

Karalis, A., Kurs, A., Moffatt, R., Joannopoulos, J., Fisher, P., and Soljacic, M. (2010). Wireless power range increase using parasitic resonators. US Patent App. 12/787,765.

Karlsson, A. (2004). Physical limitations of antennas in a lossy medium. *Antennas and Propagation, IEEE Transactions on*, 52(8):2027–2033.

Kiani, M. and Ghovanloo, M. (2012). The circuit theory behind coupled-mode magnetic resonance-based wireless power transmission. *Circuits and Systems I: Regular Papers, IEEE Transactions on*, 59(9):2065–2074.

Kiani, M. and Ghovanloo, M. (2013). A figure-of-merit for designing high-performance inductive power transmission links. *Industrial Electronics, IEEE Transactions on*, 60(11):5292–5305.

Kiani, M., Jow, U.-M., and Ghovanloo, M. (2011). Design and optimization of a 3-coil inductive link for efficient wireless power transmission. *Biomedical Circuits and Systems, IEEE Transactions on*, 5(6):579–591.

Kim, H.-S., Won, D.-H., and Jang, B.-J. (2010). Simple design method of wireless power transfer system using 13.56 mhz loop antennas. In *Industrial Electronics (ISIE), 2010 IEEE International Symposium on*, pages 1058–1063. IEEE.

Kim, J. and Rahmat-Samii, Y. (2004). Implanted antennas inside a human body: Simulations, designs, and characterizations. *Microwave Theory and Techniques, IEEE Transactions on*, 52(8):1934–1943.

Kim, K. (2012). *Wireless Power Transfer: Principles and Engineering Explorations*. Intech.

King, R. W. P., Smith, G. S., Owens, M., and Wu, T. T. (1981). Antennas in matter: Fundamentals, theory, and applications. *NASA STI/Recon Technical Report A*, 81:29690.

Kumar, A., Mirabbasi, S., and Mu, C. (2009). Resonance-based wireless power delivery for implantable devices. In *Biomedical Circuits and Systems Conference, 2009. BioCAS 2009. IEEE*, pages 25–28.

Kurokawa, K. (1969). Some basic characteristics of broadband negative resistance oscillator circuits. *Bell System Technical Journal*, 48(6):1937–1955.

Kurs, A., Karalis, A., Moffatt, R., Joannopoulos, J. D., Fisher, P., and Soljačić, M. (2007). Wireless power transfer via strongly coupled magnetic resonances. *science*, 317(5834):83–86.

Large, D., Ball, L., and Farstad, A. (1973). Radio transmission to and from underground coal mines–theory and measurement. *Communications, IEEE Transactions on*, 21(3):194–202.

Lee, K. and Cho, D. (2015). Analysis of wireless power transfer for adjustable power distribution among multiple receivers.

Lee, K. and Cho, D.-H. (2013). Diversity analysis of multiple transmitters in wireless power transfer system. *Magnetics, IEEE Transactions on*, 49(6):2946–2952.

Manteghi, M. (2013a). Electrically coupled loop antenna as a dual for the planar inverted-f antenna. *Microwave and Optical Technology Letters*, 55(6):1409–1412.

Manteghi, M. (2013b). A new resonator for high efficiency wireless power transfer. In *Antennas and Propagation Society International Symposium (APSURSI), 2013 IEEE*, pages 838–839. IEEE.

Manteghi, M. and Ibraheem, A. (2014). On the study of the near-fields of electric and magnetic small antennas in lossy media.

McLean, J. S. (1996). A re-examination of the fundamental limits on the radiation q of electrically small antennas. *Antennas and Propagation, IEEE Transactions on*, 44(5):672.

Mohammadian, A. (2009). Method and apparatus with negative resistance in wireless power transfers. US Patent App. 12/266,525.

Nambiar, S. C. and Manteghi, M. (2014a). A simple wireless power transfer scheme for implanted devices. In *Radio Science Meeting (USNC-URSI NRSM), 2014 United States National Committee of URSI National*, pages 1–1. IEEE.

Nambiar, S. C. and Manteghi, M. (2014b). Study of coupling efficiency of wireless power transfer systems in implanted applications. In *Antennas and Propagation Society International Symposium (APSURSI), 2014 IEEE*, pages 842–843. IEEE.

Neihart, N. M. and Harrison, R. R. (2005). Micropower circuits for bidirectional wireless telemetry in neural recording applications. *Biomedical Engineering, IEEE Transactions on*, 52(11):1950–1959.

Ping, S., Hu, A. P., Malpas, S., and Budgett, D. (2008). A frequency control method for regulating wireless power to implantable devices. *Biomedical Circuits and Systems, IEEE Transactions on*, 2(1):22–29.

Pollock, C. R. (1995). *Fundamentals of optoelectronics*. Irwin Chicago.

Poon, A. S., O'Driscoll, S., and Meng, T. H. (2007). Optimal operating frequency in wireless power transmission for implantable devices. In *Engineering in Medicine and Biology Society, 2007. EMBS 2007. 29th Annual International Conference of the IEEE*, pages 5673–5678. IEEE.

RamRakhyani, A. K. and Lazzi, G. (2013). On the design of efficient multi-coil telemetry system for biomedical implants. *Biomedical Circuits and Systems, IEEE Transactions on*, 7(1):11–23.

RamRakhyani, A. K., Mirabbasi, S., and Mu, C. (2011). Design and optimization of resonance-based efficient wireless power delivery systems for biomedical implants. *Biomedical Circuits and Systems, IEEE Transactions on*, 5(1):48–63.

Rhea, R. W. (1995). *Oscillator design and computer simulation*. Noble Publishing.

Salehi, M. and Manteghi, M. (2014). Self-contained compact transmitter for high-rate data transmission. *Electronics Letters*, 50(4):316–318.

Salehi, M., Manteghi, M., Suh, S.-Y., Sajuyigbe, S., and Skinner, H. G. (2013). A wideband frequency-shift keying modulation technique using transient state of a small antenna. *Progress In Electromagnetics Research*, 143:421–445.

Sample, A. P., Waters, B. H., Wisdom, S. T., and Smith, J. R. (2013). Enabling seamless wireless power delivery in dynamic environments. *Proceedings of the IEEE*, 101(6):1343–1358.

Si, P., Hu, A. P., Hsu, J. W., Chiang, M., Wang, Y., Malpas, S., and Budgett, D. (2007). Wireless power supply for implantable biomedical device based on primary input voltage regulation. In *Industrial Electronics and Applications, 2007. ICIEA 2007. 2nd IEEE Conference on*, pages 235–239.

Smith, G. S. (1984). Directive properties of antennas for transmission into a material half-space. *Antennas and Propagation, IEEE Transactions on*, 32(3):232–246.

Taga, T. and Tsunekawa, K. (1987). Performance analysis of a built-in planar inverted antenna for 800 mhz band portable radio units. *Selected Areas in Communications, IEEE Journal on*, 5(5):921–929.

Tesla, N. (1900). Apparatus for transmission of electrical energy. US Patent 649,621.

Tesla, N. (1914). Apparatus for transmitting electrical energy. US Patent 1,119,732.

Toncich, S., Ozaki, E., and Mohammadian, A. (2009). Method and apparatus for adaptive tuning of wireless power transfer. US Patent App. 12/266,522.

Villamil, C. and Manteghi, M. (2013). A circuit model for the pifa. In *Antennas and Propagation Society International Symposium (APSURSI), 2013 IEEE*, pages 702–703.

Wait, J. R. (1952). The magnetic dipole antenna immersed in a conducting medium. *Proceedings of the IRE*, 40(10):1244–1245.

Wang, G., Liu, W., Sivaprakasam, M., Zhou, M., Weiland, J. D., and Humayun, M. S. (2006). A dual band wireless power and data telemetry for retinal prosthesis. In *Engineering in Medicine and Biology Society, 2006. EMBS'06. 28th Annual International Conference of the IEEE*, pages 4392–4395. IEEE.

Wei, X., Wang, Z., and Dai, H. (2014). A critical review of wireless power transfer via strongly coupled magnetic resonances. *Energies*, 7(7):4316–4341.

Wheeler, H. (1958). Fundamental limitaions of a small vlf antenna for submarines. *Antennas and Propagation, IRE Transactions on*, 6(1):123–125.

Wheeler, H. A. (1947). Fundamental limitations of small antennas. *Proceedings of the IRE*, 35(12):1479–1484.

Wheeler, H. A. (1959). The radiansphere around a small antenna. *Proceedings of the IRE*, 47(8):1325–1331.

Wheeler, H. A. (1975). Small antennas. *Antennas and Propagation, IEEE Transactions on*, 23(4):462–469.

Xiaoyu, L., Fei, Z., Hackworth, S. A., Sclabassi, R. J., and Mingui, S. (2009). Wireless power transfer system design for implanted and worn devices. In *Bioengineering Conference, 2009 IEEE 35th Annual Northeast*, pages 1–2.

Zierhofer, C. M. and Hochmair, E. S. (1996). Geometric approach for coupling enhancement of magnetically coupled coils. *Biomedical Engineering, IEEE Transactions on*, 43(7):708–714.

Zimmerman, T. G. (1996). Personal area networks: near-field intrabody communication. *IBM systems Journal*, 35(3.4):609–617.

Appendix A

ADS Techniques

A.1 Introduction

Keysight (Agilent) ADS has been an indispensable tool for studying the various aspects of this thesis. A Test Bench Creation tool for optimization of the equivalent circuits is shown in the first section followed by some tutorial links for studying non-linear techniques that the author found helpful.

A.2 Test Bench Creation for Equivalent Circuit Optimization

To facilitate a semi-automated approach to computing the equivalent circuit parameters for an ECLA (or any antenna in general), the author created the following setup for fast iteration. The following technique allows one to create a model for a device and optimize parameters to fit measurement data.

The hierarchy is as: Device model – Test Bench (TB) – Test Lab (TL) to compare model with measurement. Note that the model can contain only pins and no ports. TB can contain ports that are referenced in TL. A Sequencer can be used to test multiple TBs one after the other. An Optimization routine takes care of minimizing the difference in the two TBs. Use

(diff=mag($S_{model} - S_{measured}$) = 0) as the optimization goal. Note that some initial seeding is required to maintain meaningfulness of this technique. For example, an approximate value for the sheet inductance[1] and capacitor values (parallel plate model, no fringing) of the ECLA can be calculated with well-known formulas. The ADS setup/flowchart is shown in Fig. A.1.
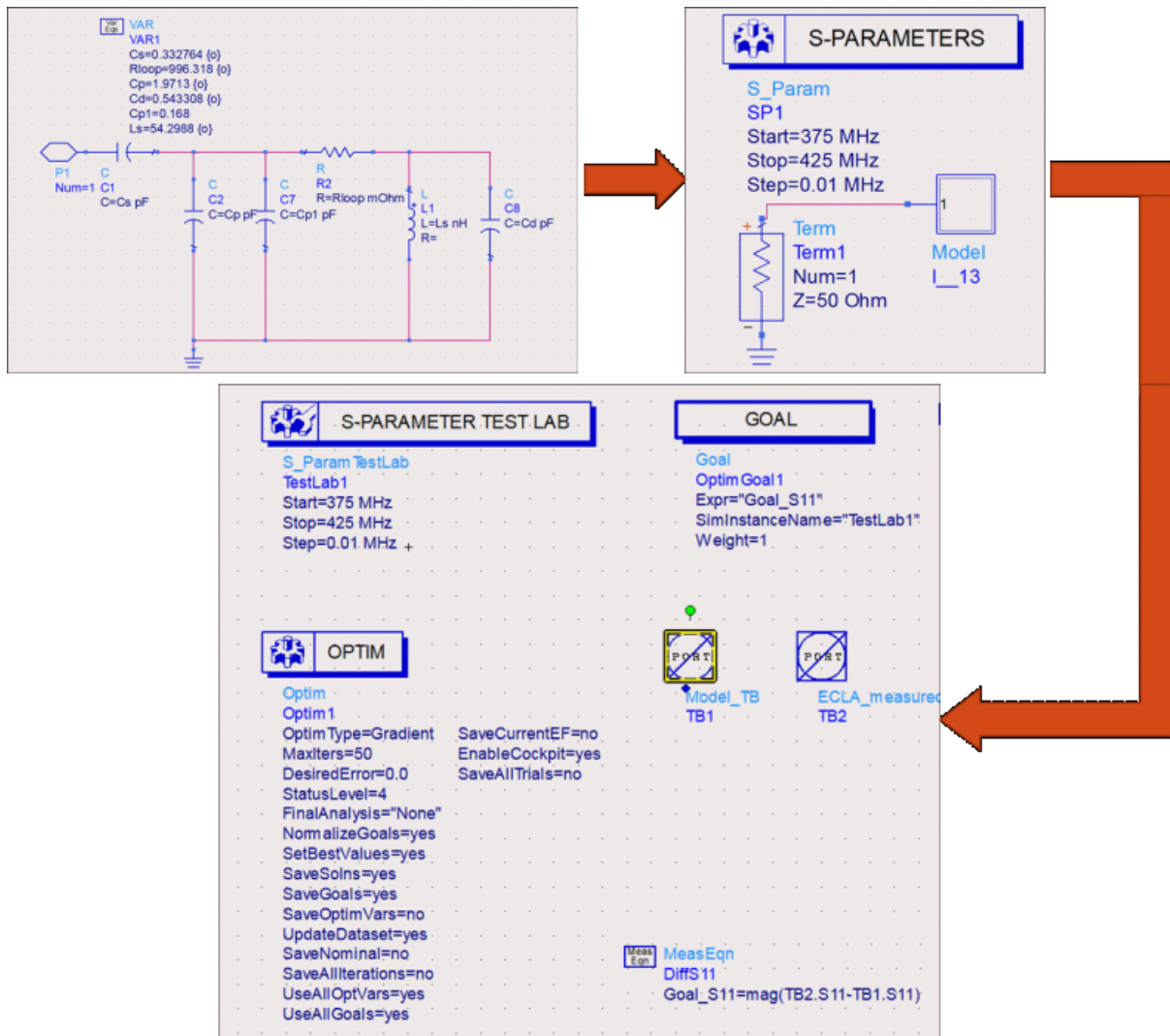
FIGURE A.1: Test Bench and Test Lab setup for creation of equivalent circuit in ADS

---

[1] http://chemandy.com/calculators/flat-wire-inductor-calculator.htm

A.3 ADS Non-Linear and General Techniques References

Given below are some useful repositories and/or direct links to ADS techniques that can be found freely on the internet.

- Prof. Long's notes: <http://www.ece.ucsb.edu/~long/ece145a/>

- Prof. Rodwell's notes on oscillator design: <http://www.ece.ucsb.edu/Faculty/rodwell/Classes/ece218b/notes/OscSim.pdf>

- Prof. Henderson's notes: <https://www.utdallas.edu/~rmh072000/Site/Software_and_Links_files/>

Appendix B

MATLAB Codes

B.1   Introduction

Along Chapters 2 and 4, some of the computational work has been done through the use of MATLAB code. They may be found below.

B.2   FEKO Field Extraction and Plotting

B.2.1   NormalizedPowerPlotter.m

```matlab
%% Dipole data plotting tool: Plots Normalized power ratios for E/M
    Dipoles
% Author: Shyam C. Nambiar
% Date: 04/09/2014
% (c) 2015 All rights reserved with author.
%% Initialize and setup
clear all;
close all;
clc;
delete *.dat;
disp('All previous data files have been deleted!');
% Theoretical Data Stored here
normPowerTh_dB=[22.6983 19.0519 16.4535 14.4399 12.8045 11.4367
    10.2701
    9.2612 8.3800 7.6047 6.9187 6.3091 5.7654 5.2792 4.84 4.4516
    4.0990
    3.7810 3.4937 3.2338 2.9982 2.7843 2.5898 2.4128 2.2513 2.1038
    1.9688];
%% Number of samples in various coordinates for E, H field data
% Ideally, both E and H fields should have same number of sample
    points.
% However, at minimum, number of radial samples and start, end limits
% should be equal to ensure comparable results.
% % Ideal dipole number of samples
% n1e=100;n1h=100;
% n2e=10;n2h=10;
% n3e=10;n3h=10;
% Physical antenna number of samples
```

```matlab
n1e=199;n1h=199;
n2e=10;n2h=10;
n3e=10;n3h=19;
% Size limits of sphere containing antenna, 'a' vector
a_min=1;
a_max=14;
a_inc=0.5;
a=a_min:a_inc:a_max;
l_a=length(a);
% % Ideal dipole file names
% E_file='dipole_sphericalNF_3';
% M_file='loop_sphericalNF_3';
% Physical antenna file names
E_file='dipole_sphericalNF_4';
M_file='loop_sphericalNF_4';
EP_n=zeros(l_a,n1e);
MP_n=zeros(l_a,n1h);
%% Load all data
[EP_r(1,:) Er(1,:)]=fn_PowerDistance3(E_file,E_file,n1e,n2e,n3e);
[MP_r(1,:) Mr(1,:)]=fn_PowerDistance3(M_file,M_file,n1h,n2h,n3h);
if ~isequal(Er,Mr)
    msg='Position vector information on E and H fields do not match!'
;
    error(msg);
end
disp('Files loaded');
% Replicating data on all other rows
EP_r=repmat(EP_r(1,:),l_a,1);
MP_r=repmat(MP_r(1,:),l_a,1);
% Normalize and store
for ii=1:l_a
    % Padding ones on non-essential indices with small values
    % to ensure consistent length. Zero-padding causes trouble in dB
    scale.
    EP_n(ii,1:ii)=ones(1,length(1:ii));
    MP_n(ii,1:ii)=ones(1,length(1:ii));
    % Normalize each row to power level found at r=a
    EP_n(ii,ii:n1e)=EP_r(ii,ii:n1e)./EP_r(ii,ii);
    MP_n(ii,ii:n1h)=MP_r(ii,ii:n1h)./MP_r(ii,ii);
end
% Convert P_n to dB
EP_n_dB=10.*log10(EP_n);
MP_n_dB=10.*log10(MP_n);
%% Plot figures
close all;
power_limits=[-50 0];
% For plotting only up to a = xx mm
disp_max_index=23;
a_limits=[a(1) a(disp_max_index)];
a_ticks=0:5:a(disp_max_index);
a1=a(1:disp_max_index);
EP_n_dB1=EP_n_dB(1:disp_max_index,1:10:n1e);
MP_n_dB1=MP_n_dB(1:disp_max_index,1:10:n1h);
c_ticks=-50:10:0;
figure(1);
surf(Er(1,1:10:n1e).*1E3,a1,EP_n_dB1);
xlabel('Radiation distance, r (mm)');
ylabel('Radius, a (mm)');
zlabel('Normalized Radiated Power {\itP}_{\itE}^{\itN} ({\itr},{\ita
    }) (dB)');
zlim(power_limits);
ylim(a_limits);
set(gca,'YTick',a_ticks)
caxis(power_limits);
view(39,12);
hcb=colorbar;
set(hcb,'YTick',c_ticks);
figure(2);
surf(Mr(1,1:10:n1e).*1E3,a1,MP_n_dB1);
xlabel('Radiation distance, r (mm)');
```

```matlab
ylabel('Radius, a (mm)');
zlabel('Normalized Radiated Power {\itP}_{\itM}^{\itN} ({\itr},{\ita
    }) (dB)');
zlim(power_limits);
ylim(a_limits);
set(gca,'YTick',a_ticks)
caxis(power_limits);
view(39,12);
hcb=colorbar;
set(hcb,'YTick',c_ticks);
figure(3);
surf(a1,Mr(1,1:10:n1e).*1E3,(MP_n_dB1-EP_n_dB1)');
ylabel('Radiation distance, r (mm)');
set(gca,'XTick',a_ticks)
xlabel('Radius, a (mm)');
zlabel('Magnetic to Electric Normalized Power Ratio (dB)');
view(39,12);
colorbar;
% load normPower_muscle_403_dB.mat;
figure(4);
plot(a,normPowerTh_dB,'-*b');
grid on;
hold on;
plot(a,MP_n_dB(:,end)-EP_n_dB(:,end),'-or');
xlabel('Radius, a (mm)');
ylabel('Magnetic to Electric Normalized Power Ratio (dB)');
legend('Theory','Simulation');
hold off;
disp('Figures plotted');
%% All limits
% figure(1);
% surf(Er(1,1:10:n1e).*1E3,a,EP_n_dB(:,1:10:n1e));
% xlabel('Radiation distance, r (mm)');
% ylabel('Radius, a (mm)');
% zlabel('Normalized Radiated Power {\itP}_{\itE}^{\itN} ({\itr},{\
    ita}) (dB)');
% zlim(power_limits);
% caxis(power_limits);
% view(39,12);
% colorbar;
%
% figure(2);
% surf(Mr(1,1:10:n1e).*1E3,a,MP_n_dB(:,1:10:n1e));
% xlabel('Radiation distance, r (mm)');
% ylabel('Radius, a (mm)');
% zlabel('Normalized Radiated Power {\itP}_{\itM}^{\itN} ({\itr},{\
    ita}) (dB)');
% zlim(power_limits);
% caxis(power_limits);
% view(39,12);
% colorbar;
%
% figure(3);
% surf(a,Mr(1,1:10:n1e).*1E3,(MP_n_dB(:,1:10:n1e)-EP_n_dB(:,1:10:n1e)
    )');
% ylabel('Radiation distance, r (mm)');
% xlabel('Radius, a (mm)');
% zlabel('Magnetic to Electric Normalized Power Ratio (dB)');
% view(39,12);
% colorbar;
%
% % load normPower_muscle_403_dB.mat;
% figure(4);
% plot(a,normPowerTh_dB,'-*b');
% grid on;
% hold on;
% plot(a,MP_n_dB(:,end)-EP_n_dB(:,end),'-or');
% xlabel('Radius, a (mm)');
% ylabel('Magnetic to Electric Normalized Power Ratio (dB)');
% legend('Theory','Simulation');
```

B.2.2 Functions

```matlab
function [ P_abs, r ] = fn_PowerDistance3( file1, file2, n1, n2, n3 )
%FN_POWERDISTANCE3 Given the filenames of E and H field data files,
    number
% of samples of each coordinate axis; returns Power wrt distance
% (Resultant Power), Distance vector.
%   Resultant power, P_abs, is resultant of components of P_r.
[~,E]=fn_FEKO_FieldExtractor(file1,'.efe');
[r_vec,H]=fn_FEKO_FieldExtractor(file2,'.hfe');
S=fn_Power2(E,H);
r=r_vec((1:n1).*n2.*n3,1);
theta=r_vec((1:n2).*n3,2);
phi=r_vec(1:n3,3);
% If symmetrical solution used, multiply by factor to compute total
    power
factor1=1;
factor2=1;
if 180-theta(end)>5
    factor1=180/theta(end);
end
if 360-phi(end)>10
    factor2=360/phi(end);
end
factor=factor1*factor2;
P_r=zeros(n1,1);
for rr=1:n1
    term=0;
    a=r(rr);
    for tt=2:n2
        dt=theta(tt)-theta(tt-1);
        for pp=2:n3
            dp=phi(pp)-phi(pp-1);
            ind=(rr-1)*n2*n3+(tt-1)*n3;
            term=term+S(ind).*(a^2).*sin(theta(tt)).*dt.*dp;
        end
    end
    P_r(rr)=term;
end
P_r=factor.*P_r;
P_abs=P_r;
% P_abs=sqrt(sum(P_r.^2,2));
end
```

```matlab
function [ r_vec, X ] = fn_FEKO_FieldExtractor( filename, ext )
%FN_FEKO_FIELDEXTRACTOR Extracts the position vector and field
    information
%from a FEKO gnerated file
%   Input: filename and extension (.efe or .hfe) as strings
%   Output: Position vector and complex field components
source=fopen([filename ext]);
if exist([filename '.dat'],'file')
    filename=[filename '(1)'];
end
target=fopen([filename '.dat'],'w');
% Define number of header lines, 15 default
numHdrLines=15;
for ii=1:numHdrLines
    [~]=fgets(source);
end
ptr=ftell(source);
% File pointer is at ptr for FEKO Field files after numHdrLines
fseek(source,ptr,-1);
% Read from source file and write to another data file
while ~feof(source)
    data=fgets(source);
    fwrite(target,data);
end
fclose('all');
dataFmt=load([filename '.dat']);
dataFmt=sortrows(dataFmt);
```

```matlab
% Store position vector columns
r_vec=dataFmt(:,1:3);
% Store Complex field values
X(:,1)=dataFmt(:,4)+1j.*dataFmt(:,5);
X(:,2)=dataFmt(:,6)+1j.*dataFmt(:,7);
X(:,3)=dataFmt(:,8)+1j.*dataFmt(:,9);
end
```

B.3 Stability Analysis, Negative Resistance Termination Network for Oscillator Design

B.3.1 NegRes.m

```matlab
%% Negative Resistance Termination Network Calculator
% Author: Shyam C. Nambiar, VTAG, Virginia Tech
% Date: 01/02/2015
% (c) 2015 All rights reserved with author.
%% Init
clear all;
clc;
%Transistor S-params at required frequency (Must fill out)
f=420.9E6;
s=[0.99641        127.32;0.15043         -95.963;2.2414
    86.852;1.1716        -161.03];
s=fn_sPar_MA_AB(s);
delta=fn_delta(s)
K=fn_RollettStab(s,delta)
% Few sample points to start
gam_T=[1j,-1,-1j,0];
gam_InP=fn_gamma_out(s,gam_T);
abs(gam_InP)
rad2deg(angle(gam_InP))
%% Plot Stability Circles
% Compute required values
disp('Magnitude of delta');
disp(abs(delta));
CL=( conj( s(2,2))-delta*(conj(s(1,1))) ) / ...
    ( (abs(s(2,2)))^2 - (abs(delta))^2 ) );
RL=abs( ( s(1,2)*s(2,1) ) / ( (abs(s(2,2)))^2 - (abs(delta))^2 ) );
CS=( conj( s(1,1))-delta*(conj(s(2,2))) ) / ...
    ( (abs(s(1,1)))^2 - (abs(delta))^2 ) );
RS=abs( ( s(1,2)*s(2,1) ) / ( (abs(s(1,1)))^2 - (abs(delta))^2 ) );
% Plot stability circles
figure(1);
hold on;
unitO=fn_circle(0,1,'b');
inpStabO=fn_circle(CL,RL,'r');
outStabO=fn_circle(CS,RS,'g');
legend('Unit Circle','Input/Load (\Gamma_{out}^\prime) Stability
    Circle','Output/Terminating (\Gamma_{in}^\prime) Stability Circle
    ');
axis equal;
grid on;
hold off;
% disp('Magnitude of Gamma_in with CL');
% disp(abs(fn_gamma_in(s,CL)));
%
% disp('Magnitude of Gamma_out with CS');
% disp(abs(fn_gamma_out(s,CS)));
%% Find optimum Gamma_InPrime or Gamma_Out
Nr=50;
x=linspace(-1,1,Nr);
y=linspace(-1,1,Nr);
```

```matlab
[X Y]=meshgrid(x,y);
xcs=real(CS);ycs=imag(CS);
idx1=find(sqrt((X-xcs).^2+(Y-ycs).^2)>RS);
Gam_T_test=X+1j.*Y;
Gam_InP_test=fn_gamma_out(s,Gam_T_test);
Z=log10(abs(Gam_InP_test));
%% Plot the values of Gamma_InPrime for various Gamma_T_test
figure(2);
hold on
pcolor(X,Y,Z);
colormap(hot);
colorbar;
unitO=fn_circle(0,1,'w');
outStabO=fn_circle(CS,RS,'g');
axis equal;
grid on;
hold off;
%% Given a specified load, design termination or vice versa
Zt=29.18-1j*4.16; % Input impedance of antenna
% Zt=50; % Input impedance of antenna
Gam_T=fn_refFromImp(50,Zt)
Gam_InP=fn_gamma_out(s,Gam_T);
ZinP=fn_impFromRef(50,Gam_InP);
Zl=-1*real(ZinP)/3 - 1j* imag(ZinP)
% Value of reactive component
iZl=imag(Zl);
if(iZl>0)
    L=iZl/(2*pi*f)
else
    C=1/(iZl*2*pi*f)
end
```

B.3.2 Functions

```matlab
function [ s_ab ] = fn_sPar_MA_AB( s_ma )
%FN_SPAR_MA_AB converts s matrix in magnitude phase form to a+jb form
ang_rad=degtorad(s_ma(:,2));
for i=1:4
    [x,y]=pol2cart(ang_rad(i),s_ma(i,1));
    temp(1,i)=x+1j*y;
end
s_ab(1,:)=temp(1,1:2);
s_ab(2,:)=temp(1,3:4);
end
% function [ s_ab ] = fn_sPar_MA_AB( s_ma )
% %FN_SPAR_MA_AB converts s matrix in magnitude phase form to a+jb
%   form
% ang_rad=degtorad(s_ma(:,2));
% for i=1:4
%     [x,y]=pol2cart(ang_rad(i),s_ma(i,1));
%     temp=x+1j*y;
%     s_ab(floor(i/2) +1,mod(i+1,2) +1)=temp;
% end
% end
```

```matlab
function delta=fn_delta(s)
%FN_DELTA computes the delta value for given s paramter matrix
%   delta=s11*s22-s12*s21
delta=s(1,1)*s(2,2)-s(1,2)*s(2,1);
end
```

```matlab
function K = fn_RollettStab(s,delta)
%FN_ROLLETTSTAB computes the Rollett Stability Factor K for gien s-
%   matrix
```

```matlab
%and delta
%    K= ( 1 + (abs(delta))^2 - (abs(s11))^2 - (abs(s22))^2)/(2*abs(s12
    *s21))
K= ( 1 + (abs(delta))^2 - (abs(s(1,1)))^2 - (abs(s(2,2)))^2)/...
    (2*abs(s(1,2)*s(2,1)));
end
```

```matlab
function gam_in = fn_gamma_in(s,gamma_l)
%FN_GAMMA_IN computes the complex value of gamma_in for given s-
    matrix and
% load reflection coefficient 'gamma_l'
%    gam_in= s11 + (s12*s21*gamma_l)/(1-s22*gamma_l)
gam_in = s(1,1) + ( s(1,2).*s(2,1).*gamma_l)./(1-s(2,2).*gamma_l);
end
```

```matlab
function gam_out = fn_gamma_out(s,gamma_s)
%FN_GAMMA_OUT computes the complex value of gamma_out for given s-
    matrix and
% source reflection coefficient 'gamma_s'
%    gam_out= s22 + (s12*s21*gamma_s)/(1-s11*gamma_s)
gam_out = s(2,2) + ( s(1,2).*s(2,1).*gamma_s)./(1-s(1,1).*gamma_s);
end
```

```matlab
function Z = fn_impFromRef(Z_0,gamma)
%FN_IMPFROMREF computes the relevant source/load reflection
%    Z= Z_0 * (1+gamma)/(1-gamma)
Z= Z_0 * (1+gamma)/(1-gamma);
end
```

```matlab
function h = fn_circle(c,r,col)
%FN_CIRCLE plots a circle with centre 'c' and radius 'r' in the
    complex
%plane
th = 0:pi/50:2*pi;
x = r * cos(th) + real(c);
y = r * sin(th) + imag(c);
h=plot(x,y,col);
end
```